Biomedicine Radioengineering **Международный научно-прикладной журнал**

БИОМЕДИЦИНСКАЯ РАДИОЭЛЕКТРОНИКА

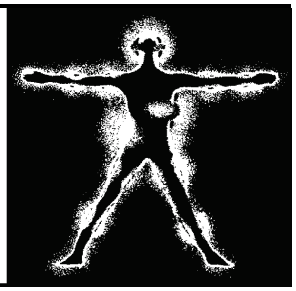

ISSN 1560-4136

5′ 2018

Выходит с 1998 г.

Включен в перечень ВАК

Proceedings of the 13th Russian German Conference on Biomedical Engineering
23.05.2018–25.05.2018, Aachen, Germany

Conference Chairs

Chair: Prof. Dr.-Ing. Dr. med. Steffen Leonhardt, Philips Chair for Medical Information Technology (MedIT), RWTH Aachen University, Germany

Co-Chair: Prof. Jaakko Malmivuo, PhD, Chair of Electronics and Medical Signal Processing (EMSP), Technische Universität Berlin, Germany

Scientific Committee

Prof. Hubertus Feußner, Technical University of Munich, Germany; Prof. Birgit Glasmacher, Leibniz Universität Hannover, Germany; Prof. Thomas Gries, RWTH Aachen University, Germany; Prof. Tobias Ortmaier, Leibniz Universität Hannover, Germany; Prof. Sergey Selishchev, National Research University of Electronic Technology, Moscow, Russia; Prof. Sergey I. Shchukin, Baumann Moscow State Technical University, Russia; Prof. Ludmila T. Sushkova, Vladimir State University, Russia; Prof. Zafar Yuldashev, Saint-Petersburg State Electrotechnical University LETI, Russia

The Russian Bavarian Conference on Biomedical Engineering (RBC) was founded 2005 in Munich. Thereafter, the conference established itself as a fruitful information exchange platform for researchers from Russia and Germany. The conference location alternated equally between cities in Russia and the southern part of Germany. After the successful 8th RBC conference in Moscow the steering committee decided to broaden the focus and establish a new conference: the Russian German Conference (RGC) on Biomedical Engineering. The goal is to serve as meeting point for information exchange and as venue for initiating bilateral Russian German research projects within the conference's scope. The first RGC on Biomedical Engineering took place in 2013 Hanover, Germany.

Previous conferences:

2016: 12th Russian-German Conference on Biomedical Engineering, 04–07.07.2016, Vladimir State University, Suzdal, Russia – Link to Proceedings
2015: 11th German-Russian Conference on Biomedical Engineering, 17–19.06.2015, RWTH Aachen University, Germany
2014: 10th German-Russian Conference on Biomedical Engineering, 25–27.06.2014, Saint Petersburg State Electrotechnical University «LETI», St. Petersburg, Russia
2013: 9th Russian-German Conference, 23–26.10.2013, Hanover, Germany
2010: 6th Russian-Bavarian Conference on Biomedical Engineering, 8–12.11.2010, Bauman Moscow State Technical University, Russia
2009: 5th Russian-Bavarian Conference on Biomedical Engineering, 01–04.07.2009, Munich, Germany
2008: 4th Russian Bavarian Conference on Biomedical Engineering, Moscow Institute of Electronic Technology, 07–11.07.2008 – Link to Proceedings
2007: 3rd Russian-Bavarian Conference on Biomedical Engineering, 02–03.07.2007, Friedrich-Alexander-University Erlangen-Nuremberg, Germany
2006: 2nd Russian-Bavarian Conference on Bio-Medical Engineering, 14–15.06.2006, Bauman Moscow State Technical University, Russia
2005: 1st Russian-Bavarian Conference on Bio-Medical Engineering, 13–14.10.2005, Munich, Germany

13-я Российско-Германская конференция по биомедицинской инженерии
23.05.2018-25.05.2018, Аахен, Германия

Организационный комитет

Руководство конференции:

Руководитель: проф. д.т.н, д.м.н., Steffen Leonhardth (С.К. Леонхард), зав. кафедрой информационных технологий в медицине, Рейнско-Вестфальский технический университет Ахена, Германия.

Заместитель: проф., к.т.н., Jaakko Malmivuo (Гакко Малмиво), Берлинский технический университет, кафедра электроники и обработки медицинских сигналов, Германия.

Научный комитет:

Проф. Hubertus FeuBner, Мюнхенский технический университет, Германия
Проф. Brigit Glasmacher (Бригит Гласмахер), Ганноверский университет имени Лейбница, Германия
Проф., Thomas Gries (Томас Гриз), Рейнско-Вестфальский технический университет Ахена, Германия
Проф. Tobias Ortmaier(Тобиас Артмаер), Ганноверский университет имени Лейбница, Германия
Проф. Селищев С.В., Национальный исследовательский университет Московский институт электронной техники, Россия
Проф. Щукин С.И., Московский государственный технический университет им. Баумана, Россия
Проф. Сушкова Л.Т., Владимирский государственный университет, России
Проф. Юлдащев З.М., Санкт-Петербургский государственный электротехнический университет ЛЭТИ, Россия

Российско-Баварская конференция по биомедицинской инженерии (РБК) была впервые проведена в 2005 г. в г. Мюнхене. С этого момента, конференция представляет собой продуктивную платформу для обмена информации учеными из России и Германии. Место проведения конференции чередовалось между городами России и южной части Германии. После успешной 8-й конференции РБК в Москве, руководящий комитет решил расширить информационное поле и организовать новую конференцию – Российско-Германскую конференцию. Основой задачей является организация встречи для обмена информацией, а также для инициирования российско-германских исследовательских проектов в рамках проводимой конференции. Первая Российско-Германская конференция впервые была проведена в 2013 г. в Германии в г. Ганновере.

Предыдущие конференции:

2016: 12-я Российско-Германская конференция по биомедицинской инженерии, 04.07. – 07.2016, Владимирский государственный университет, Суздаль, Россия
2015: 11-я Российско-Германская конференция по биомедицинской инженерии, 17.06 – 19.06.2015, Рейнско-Вестфальский технический университет Ахена, Германия
2014: 10-я Российско-Германская конференция по биомедицинской инженерии, Санкт-Петербургский государственный электротехнический университет ЛЭТИ, Санкт-Петербург, Россия
2013: 9-я Российско-Германская конференция, 23.10 – 26.10.2013, Ганновер, Германия
2010: 6-я Российско-Баварская конференция по биомедицинской инженерии, 08.11 – 12.11.2010, Московский государственный технический университет им. Н.Э. Баумана, Москва, Россия
2009: 5-я Российско-Баварская конференция по биомедицинской инженерии, 01.04 – 04.07.2009, Мюнхен, Германия
2008: 4-я Российско- Баварская конференция по биомедицинской инженерии, 07.07 – 11.07.2008. Московский институт электронной техники, Россия
2007: 3-я Российско- Баварская конференция по биомедицинской инженерии, 02.07 – 03.07.2007, Нюренбенрг, Германия
2006: 2-я Российско- Баварская конференция по биомедицинской инженерии, 14.06 – 15.06.2006, Московский государственный технический университет им. Н. Э. Баумана, Москва, Россия
2005: 1-я Российско- Баварская конференция по биомедицинской инженерии, 13.10 – 14.10.2005, Мюнхен, Германия

Contents
Содержание

1

Клинические признаки различных типов пигментных новообразований кожи в ранней диагностике с целью выявления предраковых изменений кожи

Римская Е.Н.[1], Аполлонова И.А.[1], Николаев А.П.[1], Кудрин К.Г. [2], Черномырдин Н.В.[1], Решетов И.В.[2], Зайцев К.И.[3]

[1] МГТУ имени Н.Э. Баумана, Москва, Россия

[2] НОКЦ пластической хирургии ГБОУ ВПО Первый московский государственный медицинский университет им. И.М. Сеченова

[3] ИОФ РАН им. А.М. Прохорова

Среди всех новообразований кожи особое внимание уделяется меланоме из-за ее крайней агрессивности. Поскольку эффективность лечения меланомы сильно зависит от ее ранней диагностики, разработка новых высокоэффективных методов раннего выявления диспластических невусов и меланомы кожи *in situ* остается крайне актуальной проблемой современной медицины, прикладной физики и инженерных наук. Перспективным путем повышения эффективности ранней неинвазивной диагностики меланомы является использование автоматизированных комплексов, что позволяет определять клинические признаки пигментных новообразований кожи, основываясь на анализе данных клинической диагностики.

Ключевые слова: пигментные новообразований кожи, клинические признаки, меланома, диспластический невус.

Влияние температуры на электрическую проводимость эритроцитов человека

Судсири Ч.Дж., Ритчи З.Дж.

Университет Принца Сонгкла, Тайланд

Проведено исследование цитоплазматической электрической проводимости эритроцитов человека при разной температуре. Дана экспериментальная оценка объема клетки и содержания клеточной воды в зависимости от температуры, по которым был выполнен расчет цитоплазматической электрической проводимости. Показано, что цитоплазматическая электрическая проводимость эритроцитов может быть оценена независимо от исследования диэлектрических свойств клеток.

Ключевые слова: цитоплазматическая электропроводность, температурная зависимость, эритроциты, объем клетки.

Разработка алгоритма автоматического обнаружения ранней стадии воспаления мягких тканей пародонта на инфракрасных изображениях

Акуленко Л.О., Колпаков А.В.

МГТУ имени Н.Э. Баумана, Москва, Россия

Представлены результаты исследования эффективности методов сегментации очагов воспаления, а также результаты оценки качества алгоритма автоматического обнаружения очагов воспаления мягких тканей пародонта на инфракрасных изображениях.

Ключевые слова: воспаление пародонта, ранняя стадия, инфракрасные изображения, автоматическое обнаружение.

Алгоритм определения и ориентации одноосного приемника системы магнитного позиционирования

Геркен Е.А., Гречихин В.В.

Южно-Российский государственный политехнический университет (НПИ) имени М.И. Платова

Системы магнитного позиционирования включают подвижный приемник, осуществляющий измерение ортогональных компонент магнитного поля в исследуемой области. В работе реализован алгоритм определения положения и ориентации одноосного приемника в трехмерном пространстве в реальном времени. Показано, что габаритные размеры приемника могут быть минимизированы без потери точности измерения.

Ключевые слова: системы магнитного позиционирования, одноосный приемник, магнитный поток.

Математическое моделирование потоков электроаэрозолей при лечении ожогов

Карпухин В.А., Мустафина К.С., Климиашвили Г.С.

МГТУ имени Н.Э. Баумана, Москва, Россия

Обоснована актуальность разработки аппарата местной электроаэрозольной терапии ожогов, обеспечивающего направленный поток электроаэрозоля на ожог и позволяющего регулировать его скорость. Исследовано влияние параметров рабочей камеры на поток с целью повышения эффективности терапии. Разработаны геометрическая и математическая модели рабочей камеры. В результате вычислительного эксперимента определены параметры рабочей камеры, при которых достигается максимальный поток.

Ключевые слова: аэрозоль, электроаэрозоль, ожоги, моделирование.

2

[2] ФГБОУ ВО «Юго-Западный государственный университет», Курск, Россия
[3] ФГБУ «3 Центральный Военный Клинический Госпиталь им. А.А. Вишневского», Москва, Россия
Получены математические модели для прогноза динамики развития критической ишемии нижних конечностей. Разработан алгоритм выбора оптимальных превентивных мер. Показана возможность уменьшения количества ампутаций нижних конечностей у пациентов, коррекции гемореологии и уменьшения тяжести состояния.
Ключевые слова: гибридные нечеткие модели, модель принятия решения, критическая ишемия нижних конечностей.

Arrhythmia Analysis in a Non-contact cECG Chair using Convolutional Neural Network

Исследование аритмии на ЭКГ, зарегистрированной бесконтактными емкостными электродами, с использованием сверточных нейронных сетей
Помпрапа А., Ахмед В., Штолленверк А., Ковалевски С., Леонард С.
Рейнско-Вестфальский технический университет Аахена
Для классификации аритмических состояний на четыре основные категории применена шестислойная сверточная нейронная сеть глубинного обучения. Продемонстрирована возможность отслеживания и классификации аритмического состояния емкостными бесконтактными электродами в реальном масштабе времени с использованием архитектуры последовательного анализа, основанной на банке биортогональных вейвлетов.
Ключевые слова: анализ электрокардиограммы, бесконтактная электрокардиография, емкостные электроды, сверточная нейронная сеть, сердечная аритмия.

Apnea Detection in a Contactless Multisensor System using Deep Learning Algorithm

Обнаружение апноэ бесконтактной мультисенсорной системой с использованием алгоритмов глубинного обучения
Помпрапа А.[1], Саянти М.С.[1], Анвар Т.[2], Штолленверк А.[3], Ковалевски С.[3], Леонард С.[1]
[1] Рейнско-Вестфальский технический университет Аахена, Германия
[2] Технологический университет Петронас, Перак, Малайзия
[3] Рейнско-Вестфальский технический университет Аахена, Германия
Для обнаружения апноэ на данных, полученных у пяти здоровых добровольцев, применена гибридная модель глубинного обучения, основанная на сверточной и рекуррентной нейронных сетях. Продемонстрирована возможность обнаружения апноэ предложенной бесконтактной мультисенсорной системой с потоковой и пакетной обработкой данных в реальном масштабе времени с использованием лямбда-архитектуры. Система может быть использована для обнаружения экстренных состояний или для долгосрочной диагностики.
Ключевые слова: сверточная нейронная сеть, рекуррентная нейронная сеть, лямбда-архитектура, синдром обструктивного апноэ во сне, индекс апноэ-гипопноэ, индекс дыхательной недостаточности.

A Noninvasive Glucose Estimation based on Near Infrared Spectroscopy and Pulse-Echo Ultrasound

Неинвазивная оценка уровня глюкозы, основанная на спектроскопии в ближней инфракрасной области и эхо-импульсном ультразвуке
Нанди С., Жан И., Зиа Дж., Синг Т., Мастрандреа Л.
Университет Баффало, Баффало, США
Предложен метод неинвазивной оценки уровня глюкозы, основанный на двух способах измерения для увеличения точности. В ходе экспериментальных исследованиях *in-vitro* показано, что предложенный метод потенциально обладает наилучшими характеристиками среди аналогов. Для оценки уровня глюкозы использованы модели линейной регрессии и гауссова процесса, с последующим объединением результатов. Работа является основой для дальнейшего проведения экспериментов *in-vivo*.
Ключевые слова: оценка уровня глюкозы, спектроскопия в ближней инфракрасной области, эхо-импульсный ультразвук, линейная регрессия, гауссов процесс.

3

«Biomedicine Radioengineering», 2018, № 7
(«Биомедицинская радиоэлектроника», 2018 г., №7)

Tissue layers three-dimensional structure formation by nanosecond laser pulses

Формирование трёхмерной структуры слоёв ткани с помощью наносекундных лазерных импульсов
Василевский П.Н.[1], Герасименко А.Ю.[1,2], Савельев М.С.[1,2], Терещенко С.А.[1]
[1] Национальный исследовательский университет «Московский институт электронной техники» (НИУ «МИЭТ»), Зеленоград, Россия,
[2] Первый Московский государственный медицинский университет имени И. М. Сеченова.
Получены трехмерные тканеинженерныхе конструкции на основе белков альбумина и коллагена с внутренним

каркасом из углеродных нанотрубок. Определены нелинейные свойства белковых водных дисперсий с углеродными нанотрубками. Увеличение значений нелинейного коэффициента поглощения с добавлением углеродных нанотрубок позволяет предположить, что нанотрубки поглощают большую часть лазерного излучения по мере увеличения его светового потока.
Ключевые слова: нелинейная оптика, углеродные нанотрубки, применение лазера, мощность лазера, поглощение.

Биотехническая система автоматической оценки степени повреждения лицевого нерва

Лаврова Е.А.[1], Самородов А.В.[1], Мордовский А.В.[2], Кудрин К.Г.[2], Поляков П.А.[2]
[1] МГТУ имени Н.Э. Баумана, Москва, Россия
[2] МНИОИ им. П.А. Герцена

Представлены результаты исследования метода автоматической оценки степени повреждения лицевого нерва, основанного на компьютерном анализе видеоизображения лица. Разработан метод регистрации видеоизображения лица. Приведены индексы асимметрии лица, полученные в результате обработки видеоизображения лица, результаты сравнения индексов асимметрии пациентов и представителей контрольной группы. Определены наиболее информативные индексы асимметрии лица.
Ключевые слова: автоматический анализ изображения лица, контрольные точки лица, повреждение лицевого нерва, асимметрия лица.

Вариация локальной скорости пульсовой волны, определяемой в течение сердечного цикла: валидация *in-vivo* с использованием двухэлементного магнитного плетизмографического артериального зонда

Набель П.М., Джайарай Дж., Моханасанкар С.
Индийский технологический институт Мадраса

Представлен метод и система прямого измерения локальных изменений скорости пульсовой волны, определяемой в течение сердечного цикла. Разработан новый двухэлементный магнитный плетизмографический артериальный зонд. Исследования на 15 здоровых добровольцах показали возможность оценки локальной скорости пульсовой волны. Предлагаемый зонд не требует калибровки и обеспечивает возможность безманжетной оценки параметров артериального давления от поверхностных артерий в каждом кардиоцикле.
Ключевые слова: магнитный плетизмографический зонд, неинвазивные измерения, вариация локальной скорости пульсовой волны,безманжетная оценка параметров артериального давления.

Гемодинамические пробы для индуцирования изменений артериального давления в лабораторных условиях

Набель П.М., Сурия В., Джайарай Дж., Моханасанкар С.
Индийский технологический институт Мадраса

Рассмотрены пять упражнений, влияющих на гемодинамику и приводящих к безопасному контролируемому изменению артериального давления. Получены данные изменения артериального давления во время каждого упражнения и после его окончания. Результаты могут быть использованы для сбора данных для развития моделей предсказания артериального давления в системах безманжетного мониторинга.
Ключевые слова: гемодинамические пробы, контролируемое изменение артериального давления, время восстановления.

Неинвазивная оценка вариаций инкрементного модуля упругости артерии, определяемого в течение сердечного цикла

Рай К., Набель П.М., Джайарай Дж., Моханасанкар С.
Индийский технологический институт Мадраса

Предложен зонд для неинвазивного измерения инкрементного модуля упругости артерии, содержащий один ультразвуковой преобразователь и тонометр для одновременного определения толщины стенки артерии, ее диаметра и пульсовых волн. Экспериментальные исследования на 10 добровольцах показали достоверность выполняемых измерений.
Ключевые слова: инкрементный модуль упругости артерии, ультразвуковой преобразователь, тонометрия, зонд для неинвазивных измерений.

Структурирование биоконструкций с углеродным нанокаркасом в белковой матрице

Герасименко А.Ю.[1,2], Глухова О.Е.[3], Слепченков М.М.[3], Журбина Н.Н.[1], Савельев М.С.[1,2], Ичкитидзе Л.П.[1,2], Подгаецкий В.М.[1], Селищев С.В.[1], Кицюк Е.П.[4], Павлов А.А.[5]

[1] Национальный исследовательский университет «Московский институт электронной техники» (НИУ «МИЭТ»), Зеленоград, Россия

[2] Первый Московский государственный медицинский университет имени И.М. Сеченова

[3] Саратовский государственный университет

[4] Научно-производственный комплекс «Технологический центр»

[5] Институт нанотехнологий микроэлектроники РАН

Приведены результаты экспериментов по структурированию биоконструкций с углероднымнанокаркасом в белковой матрице. Выявлен механизм связывания одностенныхуглеродных нанотрубок под действием лазерного излучения. Представлены синтезированные образцы каркасного наноматериала на основе разветвленной структуры углеродных нанотрубок. Экспериментально исследовано и продемонстрировано лазерное формирование древовидной структуры нанокаркаса изуглеродных нанотрубок в белковой матрице.

Ключевые слова: структурирование, биоструктуры, биоматериалы, углеродные нанотрубки, белковая матрица, импульсное лазерное излучение.

Mixed Reality applications for the collaborative operating room – a prototypical study

Приложения смешанной реальности для коллаборативного операционного блока – прототипное исследование

Мараренс Н., Остлер Д., Вейнцирл Дж., Кон Н., Фогель Т., Вильгельм Д., Коллер С., Фесснер Х.

Мюнхенский технический университет

Приведено исследование потенциала применения приложений смешанной реальности для эффективного взаимодействия в коллаборативном операционном блоке. Представлено описание примера использования устройства, помогающего операционной сестре в корректном выборе хирургического инструмента, пользовательская оценка алгоритма взаимодействия с устройством смешанной реальности.

Ключевые слова: смешанная реальность, дополненная реальность, коллаборативный операционный блок, хирургические вспомогательные технологии, распознавание объектов.

Longterm high resolution manometry (HRM) challenges and pitfalls of an automated motility analysis

Длительная манометрия высокого разрешения: сложности и недостатки автоматизированного анализа моторики пищевода

Елл А.[1], Хюссер Н.[1], Хе С.[1], Остлер Д.[1], Телышев Д.[2], Селишев С.[2], Фесснер Х.[1]

[1] Мюнхенский технический университет, Германия

[2] Национальный исследовательский университет «Московский институт электронной техники» (НИУ «МИЭТ»), Зеленоград, Россия

Обоснована актуальность пролонгации эзофагиальной манометрии высокого разрешения (ЭМВР) для учета изменения циркадных ритмов в работе пищевода. Проведены клинические исследования моторики пищевода с помощью длительной ЭМВР. Разработана программа автоматического анализа, основанная на чикагской классификации. В результате были установлены значения нормы и патологии для выявления нарушений работы пищевода при проведении длительной ЭМВР.

Ключевые слова: эзофагоманометрия, манометрия высокого разрешения, пищевод.

Investigation of the spectral properties of media based on chitosan and carbon nanotubes

Исследование спектральных свойств сред на основе хитозана и карбоновых нанототрубок

Федорова Ю.О.[1], Полохин А.А.[1], Мурашко Д.Т.[1], Савельев М.С.[1], Герасименко А.Ю.[1,2]

[1] Национальный исследовательский университет «Московский институт электронной техники» (НИУ «МИЭТ»), Зеленоград, Россия

[2] ПМГМУ им. И.М. Сеченова

Представлены результаты исследований спектральных характеристик материалов на основе хитозана с включениями карбоновых нанотрубок, применяемых в кардиоваскулярной хирургии для создания имплантируемых тканей.

Ключевые слова: хитозан, нанототрубки, спектральные характеристики, кардиохирургия, тканевая инженерия.

Piezoelectric properties of PVDF and PVDF-TrFE electrospun materials for nerve regeneration

Пьезоэлектрические свойства материалов PVDF и PVDF-TrFE, изготавливаемых электропрядением, для восстановления нервов

Халаби Ф. Аль[1], Гришков О.[1], Кун А.И.[1], Капралова В.М.[2], Гласмахер Б.[1]

[1] Ганноверский университет имени Лейбница, Германия

[2] Санкт-Петербургский политехнический университет Петра Великого, Российская Федерация

Поливинилидинфторид и трифторэтилен являются перспективными материалами для разработки активных имплантатов для регенерации нервов. Разработан метод измерения параметров материалов для описания их электромеханической связи. Метод заключается в создании механического напряжения волокнистых образцов с последующим измерением индуцированных электрическихзарядов.

Ключевые слова: пьезоэффект, восстановление нервов, электромеханическая связь.

Evaluation of the P300 parameters with photic stimulation

Оценка параметров P300 при фотостимуляции

Дмитриев А.Н., Щукин С.И.

МГТУ имени Н.Э. Баумана, Москва, Россия

Показано влияние фотостимуляции с частотами 1, 3 и 5 Гц и пространственным интервалом между светодиодами 0.8°, 1.6 и 2.4 на детекцию P300. Продемонстрировано изменение амплитуды и латентности P300 для разных режимов стимуляции. Оценено влияние зрительных вызванных потенциалов на детекцию P300.

Ключевые слова: P300, ИМК, фотостимуляция, ЗВП, пространственный интервал.

Telephone call management in the cognitive operating room

Управление телефонными звонками в когнитивной операционной комнате

Кон Н., Остлер Д., Коллер С., Мараренс Н., Замм Н., Кранцфелдер М., Фогель Т., Вильгельм Д., Фесснер Х.

Мюнхенский Технический Университет

Мобильные телефоны повышают доступность хирургов и регулярно берутся в операционную. Но это увеличивает рабочую нагрузку и может привести к негативному влиянию на результат операции. Предложена система ситуационной осведомленности, основанная на классификации звонков по важности, приведены варианты сценариев реагирования. Результат опроса явно показывает преимущество системы управления звонками.

Ключевые слова: когнитивная операционная комната, управление звонками, классификация важности звонков.

Translation Dynamics in Holistic Analysis of Functional Human-body System

Трансляционная динамика в комплексном анализе работы организма человека

May И.[1,2]

[1] Дюссельдорфский Университет им. Г.Гейне, Дюссельдорф, Германия

[2] Частный институт вычислительных методов, Крефельд, Германия

Предложена математическая модель аксиоматической конфигурации динамики, основанная на системном подходе, которая может объяснить динамику работы человеческого организма совместно на различных уровнях. Данный метод позволяет упростить вычислительный процесс, в его основе лежит принцип получения математических выражений высоких уровней из математических выражений более низких уровней.

Ключевые слова: математическое моделирование, системный подход, динамика.

Ready for the Future: 5G Data Transfer in Visceral Surgery

Возможности «Хирургии 4.0»: передача данных 5G при минимально-инвазивной хирургии

Фогель Т.[1,2], Мараренс Н.[1], Коллер С.[1], Йелл А.[1,2], Остлер Д.[1], Вайгель В.[3], Айшингер Дж.[3], Фесснер Х.[1,2], Кранцфелдер М.[1,2]

[1] Ганноверский университет имени Лейбница, Германия

[2] Санкт-Петербургский политехнический университет Петра Великого, Санкт-Петербург, Российская Федерация

[3] Научный центр Мюнхена Huawei, Германия

Технологии передачи данных в операционной ограничены с точки зрения скорости передачи, латентности и стабильности сигнала. Проведено исследование по методу «Дельфи», в котором дана оценка ожидания и принятия технологии 5G в хирургическом поле в целом. Предварительные результаты исследования по методу «Дельфи» показывают положительную перспективу реализации технологии 5G в клинической среде.

Ключевые слова: минимально-инвазивная хирургия, передача данных, 5G.

IVAP 2025 – Towards the collaborative operating room

IVAP 2025 – По направлению к коллаборативной операционной комнате

Остлер Д., Мараренс Н., Кон Н., Коллер С., Кранцфелдер М., Фесснер Х., Вильгельм Д.

Мюнхенский Технический Университет

Представлены первые результаты построения коллаборативной операционной комнаты, которая активно поддерживает контекстно-зависимое интра- и послеоперационное лечение. Функционирование когнитивной хирургической среды демонстрируется на типичном примере лапароскопической резекции желчного пузыря. Приведено описание концепции коллаборативной операционной комнаты и ее основные компоненты; их реализация показала эффективность предложенного подхода.
Ключевые слова: коллаборативная комната, анализ данных, резекция, желчный пузырь.

Представлен метод получения нанокомпозитных биоконструкций из водно-белковой дисперсии углеродных нанотрубок. Приведены результаты исследований структурных и биологических свойств нанокомпозитных биологических структур для тканевой инженерии, созданных методом лазерного трехмерного прототипирования. Показано, что разработанный метод может быть применен для восстановления остеохондральных дефектов в суставах.
Ключевые слова: нанокомпозиты, трехмерное лазерное прототипирование, тканевая инженерия.

Повышенный уровень стресса и рабочие нагрузки хирургов во время операций являются серьезной угрозой безопасности пациентов. Показано, что параметры сердечного и дыхательного ритма являются маркерами физического и умственного стресса, который, в свою очередь, будет пропорционален уровню образования и опыту хирурга. Результаты такого анализа могут быть интегрированы в систему распознавания рабочих процессов, в том числе для роботизированных операций.
Ключевые слова: робот-ассистивные технологии, показатели уровня стресса, лапароскопическая хирургия, сердечный и дыхательный ритм, машинное обучение.

Представлены последние результаты работы автора в области разработки эффективных алгоритмов оценивания параметров вариабельности сердечного ритма. Показано, что в рамках методологии многомасштабного корреляционного анализа, на основе вычисления по масштабно-временным представлениям ряда геометрических характеристик, можно достаточно надежно оценивать параметры сердечного ритма и осуществлять последующий анализ их динамики. На примере длительных (Холтеровского типа) ЭКГ записей обсуждаются скоростные, робастные и др. характеристики предложенного метода.
Ключевые слова: анализ биомедицинских сигналов, обработка длительных записей ЭКГ, многомасштабный корреляционный анализ, вариабельность сердечного ритма, корреляционная ритмография, геометрические методы анализа ВСР, оценивание параметров медленных волн ВСР.

Рассмотрены аспекты решения проблемы восполнения обратной связи в биоэлектрических протезах предплечья. Описана связь между кинематической и математической моделями протеза предплечья для расчета параметров для реализации обратной связи. Для получения входных данных модели, произведена серия экспериментов по раздавливанию хрупких объектов протезом.
Ключевые слова: обратная связь, биоэлектрический протез предплечья, тактильная информация.

Использование минимально инвазивных технологий при кохлеарной имплантации сдерживается повышением требований к точности сверления улитки внутреннего уха. Одним из способов достижения требуемой точности является использование индивидуального слепка улитки пациента внутреннего уха в качестве проводника для сверла. Показана возможность применения для этого гранулированных термопластов низкого давления.
Ключевые слова: гранулированные термопласты низкого давления, минимально инвазивная хирургия, кохлеарная имплантация.

"Biomeditsinskaya radioelektronika" (Biomedicine Radioengineering) is a scientific and technical journal devoted to biomedicine technologies and electromagnetic oscillations influence on biological objects. Established in 1998.
Полный список опубликованных в журналах статей, а также аннотации к ним Вы найдете на нашем сайте http://www.radiotec.ru

РАДИОТЕХНИКА

Учредитель ООО «Издательство «Радиотехника». Свидетельство о регистрации № 016200 от 10 июня 1997 г.
Сдано в набор 16.04.2017. Подписано в печать 10.05.2018. Печ. л. 9. Тираж 500. Изд. № 75.

107031, Москва, К-31, Кузнецкий мост, д. 20/6. Тел./факс +7(495)621-4837
info@radiotec.ru

Дизайн и допечатная подготовка ООО «САЙНС-ПРЕСС».
Отпечатано с предоставленных готовых файлов в полиграфическом центре ФГУП «Издательство «Известия». 127254, ул. Добролюбова, д. 6. Контактный телефон: (495)650-38-80. Заказ №

ISSN 1560-4136

DEVELOPMENT OF SOFTWARE SYSTEM FOR RESTORATION OF MIMIC ACTIVITY OF PATIENTS WITH APHASIA

A.A. Polishchuk[1], I.A. Apollonova[1]

[1]Bauman MSTU, Russia

Contact: gotikgit@mail.ru

Introduction

According to the Federal Statistical Agency of the Russian Federation for the 2015 year, the most common diseases are: diseases of the nervous system (2 257 cases per 113 927) and traumatism (13 235 cases per 113 927 people) [1]. In the USA, each year more than 700 000 people come through a stroke and 85 % of them suffer from aphasia. The number of diseased people will be doubled by 2020 year [2]. Thus, it is arguable that aphasia is a common disease. Aphasia is a systemic speech disorder that covers the different levels of speech organization [3]. The causations of disease are stroke, encephalitis, neurosurgical intervention, a chronic dysfunction of the central nervous system, etc. The principal symptoms: chaotic re-arrangement of syllables and sounds; violation of memorizing the names of objects, etc.

The development of the software system (SS) for restoration of mimic activity of patients with aphasia will significantly reduce the doctor's workload, will increase the patient capacity in hospitals, will allow the patient to perform independently certain exercises.

Scope and requirements

The objectives of SS for restoration of mimic activity: correction of the aphasia and replacement the existing electroneuromyography method. As a result, after working with the SS, the speech apparatus of the patient should be restored and the pronunciation of sounds should be clearer. The SS is made as a training program on PC, which stores in its database the articulation of several healthy people. The patient's task is to repeat the pronunciation of the phoneme, which he has first seen on the screen. Next, the process of pronouncing the phoneme by the patient will be recorded by a web camera. After that, there will be a placement of the control points and their comparison with the existing database. As a result, the program will be able to evaluate the correctness or incorrectness of the pronounced phoneme.

For the correct recognition of the face, the patient should sit strictly opposite the web camera, at a distance of 50-70 cm. In this way, the oral region is clearly displayed on the screen. The resolution of the web camera must be at least 1 280 x 720 for clear detection of the lips line on the image. The duration of continuous work on the computer for one patient should not exceed two hours.

For correct recognition of lips line, the relative error of the software should not exceed 5 %. The relative error of the automatic placement of control points 1, 4, 7, 9, 11, 13, 15, 17 should not exceed 2 %.

Control points

On the lips, it is possible to place the control points, the position of which, individually or in sum, uniquely determines the change of the position of the muscles of the mouth during speaking. The program «ASM Photo» automatically places the control points on lips line and allows a user to conduct different research. The program is based on the active shape model. The task of finding the lips line is realized by solving the problem of minimizing the energy function, which is calculated for each control point of the contour and its surroundings [4]. The placement of the control points is represented in figure 1.

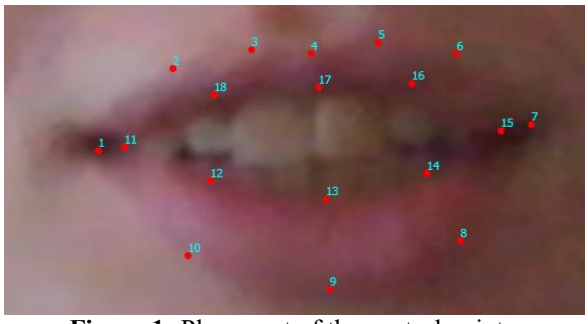

Figure 1: Placement of the control points.

Points 1-2-3-4-5-6-7-8-9-10 characterize the circular muscle of the mouth; 1-2-3-4 and 4-5-6-7 – small and large zygomatic muscle; 2-3-4 – the muscle that lifts the upper lip; 8-9-10 characterizes the muscle, lowering the lower lip and chin muscle; 6-7-8 and 2-1-10 – buccal muscle [5].

For the further work were chosen the control points, which clearly characterize the pronounced phonemes: 1, 4, 7, 9, 11, 13, 15 and 17. At the same time, it became possible to reduce the amount of data for handling. The control points 1 and 11 characterize the right corner of the mouth (outer and inner contours); 7 and 15 – the left corner of the mouth; 4 and 15 – the middle of the upper lip; 9 and 13 – the middle of the lower lip.

Experiment

To verify the workability of the model of the SS were selected five healthy people and five actors, which was simulating articulation disorders. Each actor pronounced to web camera six vowel phonemes: «А», «О», «У», «Э», «И», and «Ы». All the videos were converted to .avi format with the help of the program «Format Factory». After that, for each video was received storyboards made by the «VirtualDub» program. For the placement of the control points, were used two programs: ASM Photo and WpfApplication1. The first program creates a file in the format .xml with the position of the control points in the system X-Y, and the second program puts these points directly on the footage. The automatic placement of the control points is represented in figure 2.

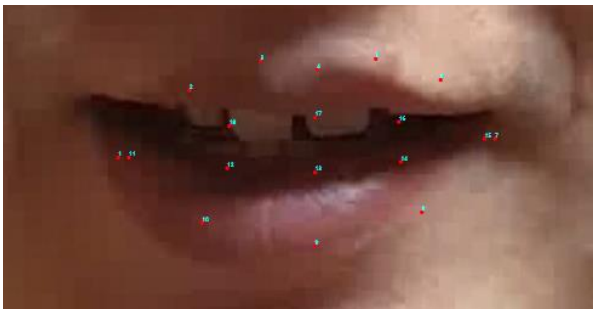

Figure 2: The automatic placement of control points made by ASM Photo and WpfApplication1.

The placement of some control points is out of true, so it may lead to errors in the data processing and, consequently, to errors in the SS.

To prevent errors in the further data processing, it is necessary to correct the placement of the control points manually (Figure 3).

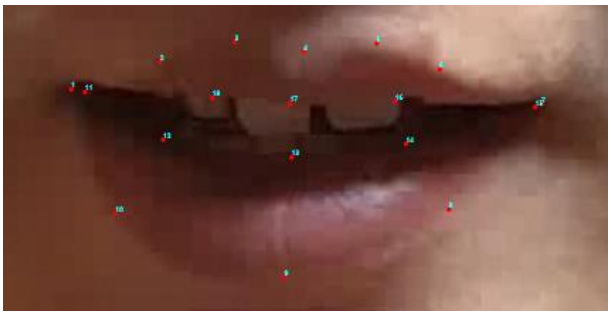

Figure 3: Manually adjust control points.

Results

The Coordinates of the control points 1, 4, 7, 9, 11, 13, 15, 17 after the automatic and manual placement are listed in table 1.

Table 1: The result of comparison the coordinates (Coord.) of the control points (CP) after automatic and manual placement.

		Phoneme					
CP	**Coord.**	**«И»**	**«А»**	**«О»**	**«Э»**	**«У»**	**«Ы»**
1	x	1,72	1,63	0,38	0,84	1,98	1,02
	y	0,81	1,86	0,31	0,86	1,13	1,08
4	x	0,90	0,08	0,15	0,31	0,30	0,74
	y	0,31	0,74	0,66	0,99	1,06	0,74
7	x	0,85	1,09	1,33	0,66	1,44	1,39
	y	0,36	1,92	1,10	0,73	1,29	0,81
9	x	0,96	0,00	0,24	0,47	0,47	0,00
	y	0,75	1,00	2,13	2,33	2,15	0,00
11	x	2,15	1,24	2,59	1,79	2,14	1,64
	y	0,69	1,97	0,71	0,96	0,63	1,13
13	x	0,70	0,15	0,30	0,47	0,42	0,33
	y	0,90	1,87	1,10	2,86	1,38	0,42
15	x	0,91	1,33	3,74	1,13	2,42	1,94
	y	0,31	1,65	1,59	0,40	1,83	1,07
17	x	0,40	0,21	0,39	0,77	0,77	0,57
	y	0,50	1,47	1,33	0,39	1,73	0,93

As can be seen from the Table 1, all the deviations of the control points are corresponding to the declared requirements for detection of the lips line (< 5 %). However, for the points 9, 11, 13 and 15, the relative error is higher than 2 %. Therefore, the automatic placement of the control points is not completely reliable. In the future research, it is proposed to use an additional filter, which transfers the image to a different color range [6]. It is assumed that the method above or alternative methods will increase the accuracy of the automatic placement of the control points to 30 %.

According to the set of additional experiments, it was established that each phoneme have a "limits of correctness" — the limits of variation the phoneme in six parameters. After the patient pronounce the phoneme, the program automatically compares the control points on the patient's lips with the "limits of correctness". According to the results of such comparison, an evaluation of the correctness of the pronunciation is displayed on the screen. The algorithmic diagram for the phoneme «О» is shown in figure 4.

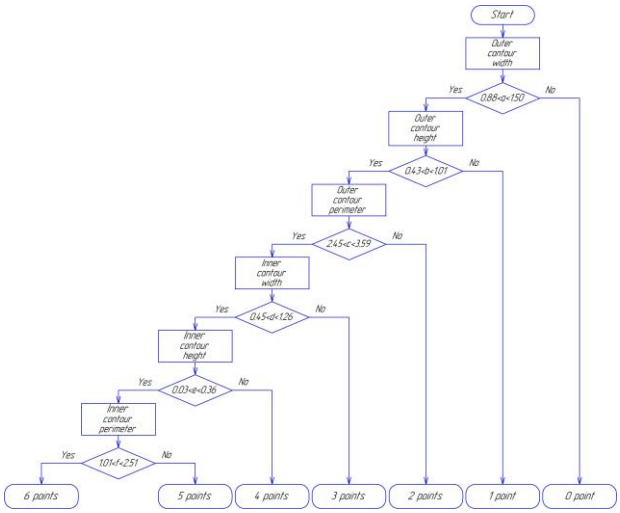

Figure 4: Evaluation of the correctness for the phoneme "O".

During the research, it was found out that the unique determining parameters for the phoneme «А» are the inner contour height and the outer contour height; for the phoneme «И» — the inner contour height and the inner contour perimeter; for the phoneme «У» — the outer contour height. The unique determining parameters — the parameters by which the phoneme is the most grossly changes. Only these parameters determine the evaluation of the quality of the pronunciation. For the phonemes «Э», «ЫІ» and «О» the unique determining parameters were not revealed, therefore, the evaluation is based on the algorithm presented in Figure 4.

Conclusion

Conducted research on the model of the SS for restoration of mimic activity of patients with aphasia proved the workability of the method. It was shown that it is possible to recognize, evaluate and determine qualitative and quantitative differences in the articulation between a healthy person and a patient with aphasia.

The requirements for the relative error in the recognition of the lips line and in the placement of the control points are given. The results of the experiment confirmed that the program «ASM Photo» can recognize the lips line with a given relative error (< 5 %), but it cannot place the control points with the relative error (< 2 %).

In addition, an algorithm for evaluation the correctness of the pronunciation of the phoneme has been developed. The results of the additional research are contradictory, and therefore are given in the abbreviated form. An additional study is required to confirm or refute the results.

References

[1] E.M. Shubochkina. Federal Service of State Statistics, 2015.
[2] Aphasia Statistics [Electronic resource]// www.pinterest.com: [website]. URL:https://ru.pinterest.com/AphasiaAware/aphasia-statistics/ (reference date: 13.April.2017).
[3] V.M. Shklovsky, T.G. Wiesel. Recovery of language functions in patients with different forms of aphasia. Association of pathologists, 2000.
[4] T.A. Zavistovskaya. Automation of the process of forming text messages based on processing the sequence of digital images of the operator's face in the presence of strong noises [Text] / Zavistovskaya TA, Kovshov E.E. – M: MSTU "STANKIN." – P. 7-8.
[5] The muscles of the face. The human body inside the outside. Deagostini, 2008.
[6] S. Soldatov. Lip Reading: Preparing Feature Vectors. Moscow: Department of Computational Mathematics and Cybernetics.

Development of algorithm for HR determination for athletes

I.A. Kusyakina[1]

[1]Bauman Moscow State Technical University (BMSTU), The second Bauman str., 5, Moscow, Russia

Contact: kusyakina123@mail.ru

Introduction

In sports practice the most often as the criterion for assessing the intensity of physical load use heart rate (HR), i.e. there is a linear relationship between heart rate and training intensity. To endurance training was the most useful, it should be done with the intensity at which activated all the oxygen-transport system. At this intensity there is no accumulation of lactic acid (lactate).

A qualitative assessment of the functional preparedness of a hockey player allows you to clearly assess the balance of its power supply systems. This knowledge may contribute to the improvement of his physical activity due to the competent use of a number of special training techniques, rather than "sports pharmacology", which very often borders on doping.

There are a huge number of methods in which you can measure the values of heart rate. This article gives an example of measurement data values by electrical impedance method. For this, it is necessary to locate the device on the head, as it is less prone artifacts of motion.

The implementation of the algorithm

According to the National American Standard ANSI / AAMI EC13: 2002 [1], it is necessary to measure the heart rate of athletes at a load range up to 200 beats per minute with an accuracy of ± 5 beats per minute.

Figure 1 shows an example of the synchronous recording of changes in electrical impedance from the head and the cardiogram in the first lead of Einthoven.

R peaks occur on the rising edge of the rheogram. As the rheogram and ECG are periodic, the distance between the R prongs, and hence the heart rate, will be calculated as the distance between the maxima on the rheogram. The front after the R wave on the rheogram drastically changes the value of the impedance, that is, during a systole a sharp decreasing front is observed. The use of a back front in the algorithm is due to the simplicity of finding peaks. The values of the maxima of the rheogram can be found using the first derivative. It is necessary that the previous count of the graph was positive, and the next one was negative, between these samples there will be an intersection with the zero of the derivative. In this count, where the derivative changes its sign, the rheogram has a maximum (peak).

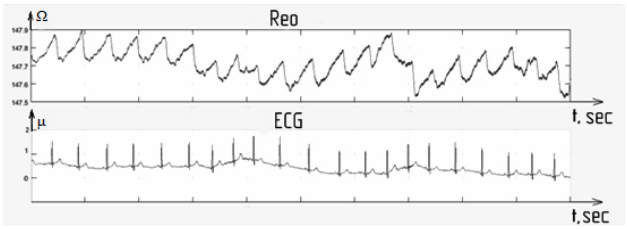

Figure 1: An example of graphs of electrical impedance from the head and ECG

Ω

In the designed algorithm it is necessary to determine the heart rate by the signal of the rheogram. To find results you must get rid of the noises superimposed on the useful signal. It is necessary to apply a low pass filter which removes high frequency. Will be used the method of exponential averaging, which suppresses noise by multiplying the input count by a constant and addition of this work with the previous average multiplied by the addition of constants to one. The advantages of this method is that it requires only one memory cell for storing the value of the reference medium to obtain the next input frame [2]. If you change the weighting factor, changes the degree of noise suppression, which is a characteristic feature of the method. The smaller the value of weighting factor, the more suppressed the noise. The obtained graph of the rheogram after applying the filter shown in figure 2.

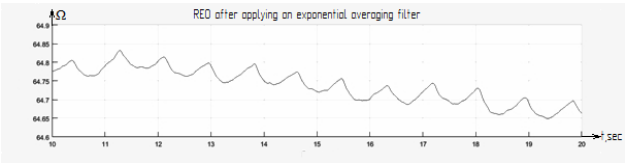

Figure 2: The rheogram after applying an exponential averaging filter

To take a derivative of the signal is used as the transition filter. At low frequencies it possesses differentiating properties and attenuates high frequencies, which is evident from the frequency response of the filter shown in figure 3.

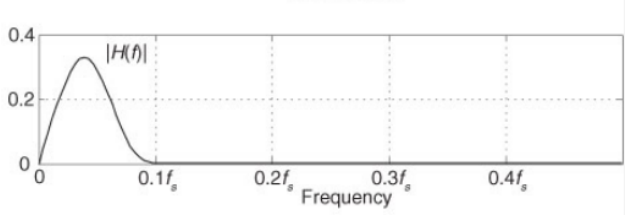

Figure 3: The frequency response of the transition filter

When the signal is significantly noisy, reliable detection of transitions of the signal provides the standard filtering with a time delay line developed by C. Turner, whose coefficients are considered according to the following formula 1:

$$C_k = -\frac{12 * (k-1) - 6 * (N-1)}{N^3 - N} \quad (1)$$

where 1 ≤ k ≤ N-1, N is usually set empirically in the range from L/4 to L, where L is the time of systole, L = 201 samples or 0.201 sec.

For any integer N the coefficients C_k of the filter contain a linear decreasing slope front, which makes this sequence very useful for identifying linear transitions in the input signal.

After using this filter graph the first derivative of the signal shown in figure 4.

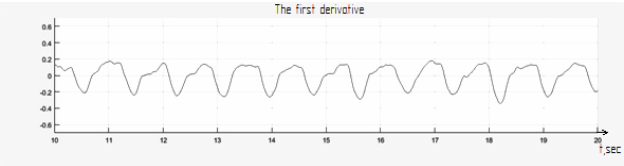

Figure 4: The first derivative of the signal after applying the transition filter

After writing the algorithm, we get:

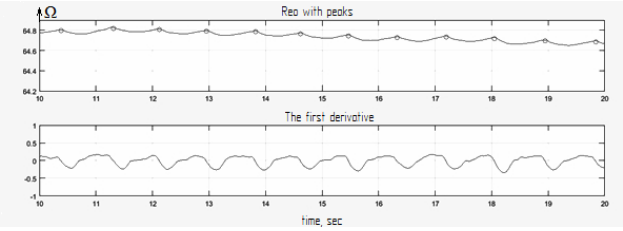

Figure 5: Rheogram with peaks and first derivative after applying a transition filter that has a delay (N-1)/2

Results

After checking the algorithm on real signals, the results are shown in Table 1.

Table 1: Results of testing the algorithm for determining HR

	Processed (PCs)	**Max error (bpm)**	**The number of false peaks (PCs).**
With exponential averaging	70	4.83	5
Without exponential averaging	70	4.966	39

Conclusions

In this paper has shown the algorithm for HR determination for athletes. Thus, using an exponential filter to averaging the rheogram reduces the number of false peaks; a maximum error of 0.136 between the true values of the heart rate calculated from the ECG, and the values calculated using the algorithm using the rheogram peaks. The designed algorithm is effective, since it has been tested on a real signal and satisfies the accuracy requirement.

References

[1] ANSI/AAMI EC13:2002. Cardiac monitors, heart rate meters, and alarms http://www.pauljbennett.com/pbennett/work/ec13/ec13.pdf

[2] R.G. Lyons Understanding Digital Signal Processing. Pearson Education, Inc., pages 430–435, 2011.

[3] N.N. Uryupin, V.V. Savostyanov, and A.V. Alehnovich. General and special readiness of hockey players (methodical guide for national team coaches) under general editorship by V.A. Tretyak. Moscow, pages 1–34, 2014.

Acknowledgements

The author would like to thank Alexander Kobelev Senior Lecturer of faculty BMT2 of Bauman Moscow State Technical University (BMSTU) who helped the author providing guidelines to perform the work.

Clinical signs of different types of pigmented skin lesions for early di-agnostics for the purpose of early detection of precancerous skin changes

E.N. Rimskaya[1], I.A. Apollonova[1], A.P. Nikolaev[1], K.G. Kudrin[2], N.V. Chernomyrdin[1], I.V. Reshetov[2], and K.I. Zaytsev[1,3]

[1]Bauman Moscow State Technical University, Moscow 105005, Russia
[2]Sechenov First Moscow State Medical University, Moscow 119991, Russia
[3]Prokhorov General Physics Institute of RAS, Moscow 119991, Russia

Contact: romehelen@gmail.com

Introduction

Among other lesions of the skin, a special attention is paid to the melanoma because of its extreme aggressiveness. Melanoma remains the leading cause of death in patients with oncodermatology [1]. A steady increase of morbidity and mortality form melanoma is observed all over the world. Since efficiency of the melanoma treatment strongly depends on its early diagnosis, the development of novel highly-efficient methods for the early detection of dysplastic skin nevi and melanomas in situ remains a challenging problem of modern medicine, applied physics and engineering sciences.

Visual examination of the skin and dermatoscopy remain the most widely applied methods for non-invasive diagnosis of dysplastic skin nevi and melanomas in situ [2]. Other techniques, such as fluorescence imaging [3,4], ultrasound diagnosis [5,6], confocal laser microscopy [7-9], thermometry [10-12], provide additional information and seem to be prospective instruments for clarifying diagnosis. An accuracy of visual dermatoscopy strongly depends on the experience of the doctor and a number of other factors that influence the process of assessing the severity of the disease. Numerous errors could occur during the visual diagnosis, among which there are errors of a subjective nature, as well as errors associated with the use of the particular diagnostic technique. A promising way to improve the effectiveness of early noninvasive diagnosis of melanoma is to use the correctly-selected early diagnosis method for various types of skin pigmented lesions.

Types of pigmented skin lesions

Methods of early diagnosis are based on the analysis of different types of pigmented skin lesions, as at the first stage it is the specialist who should classify the pigmented lesion for the correct further diagnosis [13].

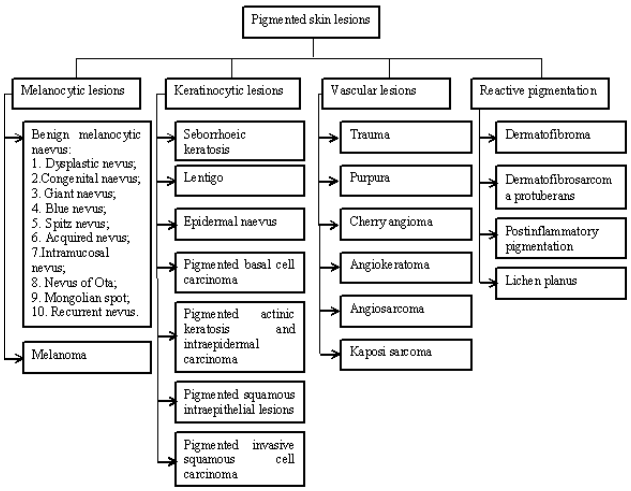

Figure 1: Types of pigmented skin lesions

Each type of nevi has its own typical clinical signs therefore it's necessary to study all the signs for benign and malignant lesions as thorough as possible. When the normal cells and tissues grow into tumor cells, the following clinical signs of pigmented skin lesions change.

Table 1 – Clinical signs of pigmented skin lesions [14]

Clinical signs	
Color	Border sharpness
Pigmentation uniformity	Form
Pigmentation intensity	Temperature of lesions
Size: diameter, area	Structure: pigmented network, globules, dots and streaks, heterogeneity
The Border of lesions	Echogenicity

Having identified several parameters from table 1, the specialist has higher chance of making the correct diagnosis. With only one of these parameters detected, the accu-

racy of the diagnosis is considerably lower for the first signs of malignancy are often difficult to distinguish from usual inflammatory changes.

The initial pattern of the disease in typical cases proceeds as follows: the pigmented lesions at some point begins to increase after a previous injury, a burn or without apparent causes, change its color, shape, structure, temperature, etc., and turns into a tumor that sometimes occurs on one of the sites of pigmented growth.

Therefore, it is necessary to isolate the clinical parameters for simple and dysplastic nevi in order to detect early precancerous skin changes and methods for their diagnosis., On the human body there are one average 80% of simple nevi, 15% of dysplastic nevi and 5% of other nevi. Comparative characteristics of clinical parameters of simple, dysplastic nevi, melanoma and methods for their diagnosis are presented in Table 2.

Table 2 – Comparative table of clinical signs of simple, dysplastic nevi, melanoma and methods for their diagnosis [3-15]

№	Signs	Simple nevus	Dysplastic nevus	Melanoma	Diagnostic methods
1	Color	1)Homogeneous colors 2)Light brown, brown	1)Heterogeneity of color 2)Light brown, brown, dark brown, yellow-brown	1)Heterogeneity of color and color asymmetry 2)Dark brown, black, gray, bluish, rose-purple	1)Dermatoscopy 2)Visual examination
2	Pigmentation uniformity	Uniform color	Uneven color change	Uneven color change	Dermatoscopy, visual examination
3	Pigmentation intensity	Very light, light	Dark, very dark	Very dark	Visual examination
4	Size: 1) diameter 2) area	1) less than 5 mm 2)less than 20 mm^2	1) from 1 mm to 1 cm 2) less than 78.5 mm^2	1) from 1 mm to 3 cm 2) less than 7.065 cm^2	1)Visual examination 2)Visual examination
5	The Border of lesions	1)Clear smooth boundaries 2) Clear boundaries 3)The Border of lesions	1)Fuzzy boundaries 2) Clear boundaries 3)The Border of lesions	1)Fuzzy boundaries 2)Fuzzy boundaries 3)Tumor boundaries	1)Visual examination, dermatoscopy 2)Ultrasound diagnosis 3)Fluorescent diagnostics
6	Border sharpness	Sharp	Unsharp	Unsharp	Visual examination
7	Form	1) Round, oval 2) Spindle shape	1) Arbitrary 2) Spindle shape	1) Arbitrary 2) Spindle shape	1)Visual examination, confocal laser scanning microscopy 2)Ultrasound diagnosis
8	Structure: 1)pigmented network 2)globules 3)dots and streaks 4)heterogeneity	1)Uniform pigment network without breakage 2)Black points located in the filaments of the pigmented network, brown or black globules in the center of education 3) - 4)Homogeneous structure	1)Irregular pigment network with breakages, heterogeneous holes in the pigment network, uneven pigment network boundary 2)Granules are usually atypical 3)Possible detection of bands 4)Homogeneous structure	1)Uneven pigment network, uneven boundary of the pigment network with a sharp break in the periphery 2)Non-structural zones, atypical granules and points 3)Atypical bands (pseudopodia and radiance), blots, spots that mimic scattered pepper, and a veil, or a blue and white veil 4)Inhomogeneous structure	1) Dermatoscopy, confocal laser scanning microscopy 2) Dermatoscopy, confocal laser scanning microscopy 3) Dermatoscopy, confocal laser scanning microscopy 4)Ultrasound diagnosis
9	Temperature of lesions	1,0 °C	1,0 °C	2,5°C	Thermometry
10	Echogenicity	Isohogenic and moderately reduced echogenicity	Hypoehogenicity or isoechoogenicity with hypoechoic zones	Moderately reduced echogenicity	Ultrasound diagnosis

Conclusions

The results of a comparative analysis of different types of pigmented lesions and their clinical signs allowed to establish the necessary type of the diagnostics for the purpose of early detection of precancerous skin changes, which will substantially increase the survival rates at the early stage of melanoma detection.

References

[1] Eisemann N., Waldmann A., Geller A., Weinstock M. et al. Non-Melanoma Skin Cancer Incidence and Impact of Skin Cancer Screening on Incidence. Journal of Investigative Dermatology 134 (1), 43-50 (2014).

[2] Tsao H., Olazagasti J., Codoro K., Brewer J. et al.. Early detection of melanoma: Reviewing the ABCDEs. Journal of the American Academy of Dermatology 72 (4), 717-723 (2015).

[3] North J.P., Garrido M.C., Kolaitis N.A., LeBoit P.E. et al. Fluorescence In Situ Hybridization as an Ancillary Tool in the Diagnosis of Ambiguous Melanocytic Neoplasms: A Review of 804 Cases. American Journal of Surgical Pathology; 38(6), 824-831 (2014).

[4] Borisova E.G., Angelova L.P., Pavlova E.P. Endogenous and Exogenous Fluorescence Skin Cancer Diagnostics for Clinical Applications. IEEE Journal of Selected Topics in Quantum Electronics; 20(2): 211-222 (2014).

[5] Rohrbach D.J., Muffoletto D., Huihui J., Saager R. et al. Preoperative Mapping of Nonmelanoma Skin Cancer Using Spatial Frequency Domain and Ultrasound Imaging. Academic Radiology; 21(2), 263-270 (2014).

[6] Taruttis A., Ntziachristos V. Advances in real-time multispectral optoacoustic imaging and its applications. Nature Photonics; 9, 219-227 (2015).

[7] Gonzalez S. Confocal reflectance microscopy in dermatology: promise and reality of non-invasive diagnosis and monitoring. Actas Dermo-sifiliograficas; 100 (2), 59—69 (2009).

[8] Longo C., Zalaudek I., Argenziano G., Pellacani G. New directions in dermatopatology: in vivo confocal microscopy in clinical practice. Dermatologic Clinics; 30 (4), 799—81 (2012).

[9] Pellacani G., De Pace B., Reggiani C., Cesinaro A.M., Argenziano G., Zalaudek I., Soyer H. P., Longo C. Distinct melanoma types based on reflectance confocal microscopy. Experimental Dermatology; 23(6), 414-418 (2014).

[10] Müller J., Hartmann J. and Bert C. Infrared camera based thermometry for quality assurance of superficial hyperthermia applicators. Physics in Medicine & Biology; 61(7), (2016).

[11] Petersen B., Philipsena P.A. and Wulf H.C. Skin temperature during sunbathing – relevance for skin cancer. Photochemical & Photobiological Sciences. 13, 1123-1125 (2014).

[12] Faust O., Acharya U.R., Ng E.Y.K., Hong T.J., Yu W. Application of infrared thermography in computer aided diagnosis. Infrared Physics & Technology; 66, 160-175 (2014).

[13] Rosendahl C., Tschandl F., Cameron A.,Kittler H. Diagnostic accuracy of dermatoscopy for melanocytic and nonmelanocytic pigmented lesions. Journal of the American Academy of Dermatology 64 (6), 1068-1073 (2011).

[14] Nachbar F., Stolz W., Merkle T., Cognetta B.A., Vogt T., Landthaler M., Bilek P., Braun-Falco O., Plewig G. The ABCD rule of dermatoscopy: High prospective value in the diagnosis of doubtful melanocytic skin lesions. Journal of the American Academy of Dermatology 30 (4), 551-559 (1994).

[15] Stevenson A., Mickan S.,2 Mallett S., Ayya M. Systematic review of diagnostic accuracy of reflectance confocal microscopy for melanoma diagnosis in patients with clinically equivocal skin lesions. USA, National Center for Biotechnology Information. Dermatol Pract Concept. Oct; 3(4), 19–27 (2013).

Effect of temperature on electrical cell conductivity of human erythrocytes

Chadapust J. Sudsiri [1], Raymond J. Ritchie [2]
[1] Department of Industrial Management, Faculty of Sciences and Industrial Technology
Prince of Songkla University – Suratthani, 84000 Thailand.

[2] Biotechnology of Electromechanics Research Unit,
Faculty of Technology and Environment,
Prince of Songkla University – Phuket, 83120 Thailand.

Contact: chadapust.s@psu.ac.th

Introduction

The electrical conductivity (σ in units of S m^{-1}) of an electrolyte is determined by the concentration and mobility of its ions. Therefore, the electrical conductivity of the cell interior should provide information about the state of the ions within the cell, i.e., whether or not they are free moving or bound by ion exchanger mechanisms to components of the cytoplasm such as proteins. It is a key measurement for dielectric studies on cells. One of the most thoroughly investigated cells is the red blood cell of mammals. This cell exhibits a simple architecture, and its composition of proteins and lipids is well known. Pauly and Schwan, (1966) measured the internal conductivity of erythrocytes and found a value of 0.518 S m^{-1} at 25 °C (σ_{25} = 0.518 S m^{-1}). They concluded that the internal conductivity is largely due to the inorganic ionic content composed primarily of K^+, Na^+, Mg^{++}, Cl^-, and HCO_3^- whose concentrations are relatively easy to measure experimentally. The concentration of ions of haemoglobin due to their net charge was reported to be +45 mmol charge/l (cell H_2O) from a total concentration of haemoglobin of 7 mM (cell H_2O) and so the mean effective +ve charge per haemoglobin molecule was +6.4 (Pauly and Schwan, 1966). The calculation of cytoplasmic conductivity from the ionic concentration of ions present in the cytoplasm multiplied by their limiting ionic conductance according to Kohlrausch's law gave a value of σ = 1.45 S m^{-1} which is 2.7 times higher than that obtained from experimental measurements by Pauly and Schwan, (1966) (σ_{25} = 0.518 S m^{-1}). They concluded that the discrepancy between ideal specific conductivity and the measured value was due to the ionic mobility being hindered by cytoplasmic viscosity (Pauly and Schwan, 1966). However, since most mammalian cells regulate their volumes, after the initial passive swelling (stomatocytogenic) or shrinking (echinocytogenic) as a result of changes in the bathing electrolyte and/or temperature, cells usually return to a near-normal volume (Glaser, 1979). Red blood cells quickly change their cell volumes because water moves quickly into them through water channel proteins called aquaporins which do not allow charged ions to pass through them (Murata et al., 2000). Several mechanisms are involved in the slower process of adjusting their cell volume back to normal, in most cases involving the loss and gain of K^+ and Cl^- and to a lesser extent Na^+(Glaser, 1979; Bernhardt, 1991; Parker, 1993; O'Neill, 1999). A perturbation of cell volume will certainly disturb the concentration of ions present in the cytoplasm as described by Glaser and Donath, (1984) and consequently cause the cytoplasmic conductivity to shift from the normal physiological state.

In this investigation, the cytoplasmic conductivity of human red blood cells (HRBCs) at different temperatures was observed. The cell volumes and cell water contents in the cells were measured experimentally. The cytoplasmic conductivity (σ_c) was calculated according to the Debye - Hückel – Onsager equation combined with Walden's rule (Laidler and Meiser, 1995) and its temperature coefficient was then estimated.

Materials and Methods

Red blood cells

HRBCs were obtained from the blood bank (Suratthani Hospital, Thailand) and used within 3 days. The cells were first separated from the blood plasma by centrifugation at 2000 g for 8 min. The supernatant plasma and buffy coat was removed. The sedimented cells were used for the experiments.

Preparation of the cell suspension

A 157 mM NaCl solution (300 mOsmol kg^{-1}) containing 1 mM Sodium Phosphate buffer (pH 6.8) was used to resuspend the cells and the conductivity of the suspending medium was adjusted to a conductivity of 1.48 S m^{-1}. The standard conductivity of the bathing electrolyte suspensions at 20°C (σ_{20}) was measured in the temperature compensation mode ($\sigma_{20} = \sigma_T(1-0.0214(T-20))$, where σ_T is the measured conductance at temperature T (°C) in a constant temperature bath using a conductivity meter (Mettler-Toledo, Switzerland).

Volume experiments

The haematocrit volume (*Hct*) of the red-cell sediment was determined in haematocrit-capillaries by centrifugation at 10000 g for 8 min (Cence, China). From the *Hct*, the amount of measuring solution was calculated that was needed for the dilution of 50 µl of the sedimented cells to a final cell concentration of 10% (v/v). The cells were incubated in the measuring solution for 5 min and the *Hct* of the suspensions were determined by haematocrit-centrifugation at 10000 g for 8 min. In parallel, the cell number was microscopically determined using a standard haemocytometer (Improved Neubauer). From the cell count and the *Hct* after 5 min in suspended solutions, the mean cell

volume (MCV) was determined following standard clinical methods (Gedde andHuestis, 1979; Harris, 1984; Sudrisi, 2009; Glaser, 2000). A trapped water volume correction constant of 3% was assumed in all *Hct* calculations (Gedde and Huestis, 1979).

Determination of cell water

Red blood cells in a standard 1.5 ml Eppendorf tube were spun down (10 000g) after 5 min of suspension in the experimental medium. 300 µl of the packed cell volume was then pipetted into a pre-weighed test tube (Gedde and Huestis, 1979; Harris, 1984; Sudrisi, 2009). In parallel, the *Hct* was determined experimentally. The tube was weighed before and after drying at 80 °C for 24 hours. The cell waterdetermination (*Wc*)was calculated from the wetted cells weight (*Wt*) and dried cells weightas (*Wd*) as follows (Harris, 1984)

$$\%\, W_c = \frac{W_t - W_d}{W_t} * 100 - (100 - Hct) * \frac{100}{Hct} \qquad (1)$$

Results

Cell volume

The data set of volume changes as well as water content of HRBCs after suspension for 5 min in the measuring solutions. The changes in cell water were found to be proportional to volume changes: the HRBC volume increases with rising of temperature. To further characterize the nature of the volume changes depending on temperature, the data on cell volume change were plotted over a range of experimental temperatures (Figure 1) and fitted to the Arrhenius-relation as a suitable model (Glaser, 2000).

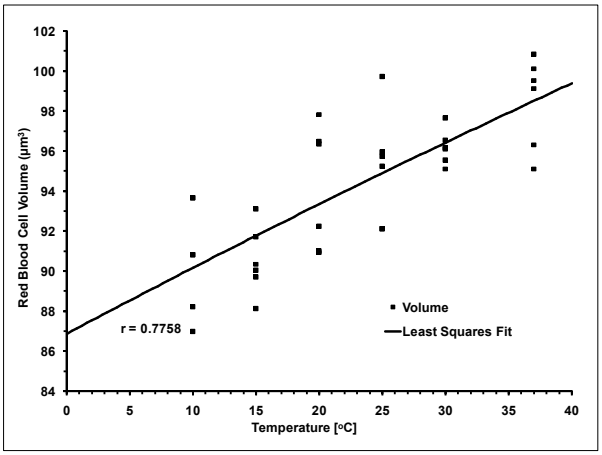

Figure 1: Volume changes over temperature in six different external conductivities. The Arrhenius relation

($V_T = Ae^{-\frac{E_A}{RT}}$) was used to fit the experimental points and fitted using non-linear least squares fitting and the asymptotic errors were calculated by matrix inversion. At the standard experimental temperature of 25 °C the cell volume was found to be 96.18 (± 0.356) × 10^{-18} m^3 (± SE, n = 6) and the cell water content was 67.55 (± 0.824) × 10^{-18} m^3 (± SE, n = 6) and at the normal human body temperature of 37 °C, cell volume = 98.52 (± 0.926) × 10^{-18} m^3 (± SE, n = 6) and cell water 69.95 (± 0.658) × 10^{-18} m^3 (± SE, n = 6).

Cytoplasmic conductivity

A Plot of calculated cytoplasmic conductivities over a range of temperatures is shown in Figure 2.The data were fitted to an exponential relation using non-linear least squares methods and the asymptotic errors of the fitted parameters calculated by matrix inversion. A temperature coefficient value of k = 0.06239 ± 0.00202 (± SE, n = 24) was obtained (Figure 2). The intracellular conductivities increased by a factor of 1.866 ± 0.0377 (± SE) for every increase in temperature of 10°C and hence the Q_{10} of cytoplasmic conductivity vs. temperature is a typical value of ≈ 2 found in many biological systems (Glaser, 2000; Nobel, 2009).

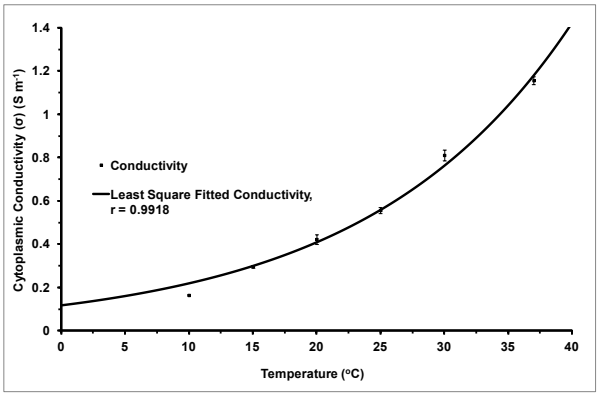

Figure 2: Cytoplasmic conductivity of HRBCs suspended in external conductivities of 1.48 S m^{-1} at six different temperatures. Data points are means ± SE (n = 4) so total n = 24. The line was fitted by non-linear least squares methods and the errors of the fitted parameters calculated by matrix inversion.

Discussion

Cell volume

The activation energy obtained from the fit in Figure 1 indicates the electrical energy required to provide a driving force for net movements of ions across the membrane plotted over the ionic concentrations of the suspending solution. Highly negative activation energy means there is a high ionic concentration difference across the cell membrane. The fits using the direct non-linear and log-transform methods both give an activation energy of about -2.4 kJ mol^{-1}. This means that there was little or no ionic concentration difference across the membrane and hence change in cell volume depends only on temperature. There are two major reasons for an influence of temperature on water influx. The first is an alteration of external hydrostatic pressure as predicted by the Van't Hoff relation. The hydrostatic pressure depends strongly on temperature and increases when the temperature is raised. The increase in external hydrostatic pressure will destroy the balance of the pressures between the two sides of the membrane. To re-balance the system, water moves down its chemical potential gradient and enters to the cell. The

cell swells. Secondly, increase in temperature will decrease the viscosity of external medium and consequently increase in the hydraulic conductivity, L_p, which is a parameter determined by the viscosity of the fluid (η) and membrane characteristics including the membrane pore of radius (r), pore number (n m^{-2}), membrane thickness (δ), which are related as follows (Sperelakis,1995):

$$L_p = \frac{n\pi r^4}{8\eta\delta} \qquad (2)$$

Cytoplasmic conductivity

The experimentally measured HRBC conductivity value at 25 °C (σ_{25} = 0.5566 ± 0.0146 S m^{-1}, ± SE, n = 4) shown in Fig. 2 agrees very well with the value of $\sigma_{25} \approx 0.5$ to 0.6 S m^{-1} found experimentally in other studies on red blood cells using quite different methods(Seidlet al., 1999; Fuhr et al., 1986; Sudsiri, 2002; Krupa and Terlecki, 1976; Asami, 1992) and is similar to theoretical estimates by Glaser and Donath (1984). For comparison, the conductivities of the cytoplasm of bacteria, plant protoplasts and yeast cells using dielectric methods have been reported to vary from 0.1 to 1.2 S m^{-1} at 25°C and so the conductivity of red blood cells appears to be representative for the cytoplasm of most cells (Hölzel and Lamprecht, 1992, 1997; Suehiro et al., 2003) despite the HRBC having a large amount of haemoglobin inside the cell which might lead to the belief that its conductivity would be unrepresentative. Of more physiological relevance is the HRBC conductivity at 37°C; σ_{37} = 1.156 ± 0.0188 S m^{-1} (± SE, n = 4) in the present study which is very nearly twice the value found at the standard measuring temperature of 25 °C. Conductivity information on HRBC cells is useful information because the conductivities of most cells are not practically measureable whereas the conductivity of the HRBC is easily measured by very simple techniques and by more than one method.

Conclusions

Our study has shown that the cytoplasmic electrical conductivity of red blood cells can be estimated from very simple experimental observations *independently* of dielectric methods. This ability to estimate conductivity independently is important in validating dielectric experiments and for modelling the electrical behaviour of the HRBC. Cell volume of human erythrocytes is sensitively affected by both external ionic concentrations and to temperature. It was found experimentally that the conductivities increased by a factor of 1.866 ± 0.0377 for every increase in temperature of 10°C and hence the Q_{10} of cytoplasmic conductivity *vs.* temperature has a value of ≈ 2. The alteration of cell volume induces changes in the cytoplasmic conductivities which depend exponentially on temperature. The convention of quoting conductivities at 25 °C can be misleading physiologically because conductivity is exponentially related to temperature (Fig. 2): the conductivity at normal body temperature (37 °C) is 1.18 ± 0.02 S m^{-1}, ± SE, n = 4) based on the curve fit. The conductivity of HRBC in a patient with a severe fever (40 °C) would have a conductivity exceeding 1.4 S m^{-1}. The experimentally determined Q_{10} of ≈ 1.866 is a typical Q_{10} value found in many biological systems, including cation transport in red blood cells (Laidler and Meiser, 1995). A Q_{10} of 2 implies surprisingly large effects of small errors in temperature in biological systems: for example an error of 1°C in the experimental temperature will result in a greater than 7% error in a conductivity determination of a living cell but only a 2% error in that of a NaCl solution. However, this temperature effect would be easy to allow for in an experiment if the experimental temperature is carefully monitored. The results suggest that in future experiments on cellular mobility in strong electric fields (Gimsa et al., 1996; Sudsiri et al., 2002, 2007) special attention to the temperature will have to be made since a temperature increase will be induced by Joule heating, especially at high media conductivities as already reported by Sudsiri et al. (2007).

References

[1] H. Pauly, H.P. Schwan, Dielectric properties and ion mobility in erythrocyte, Biophys. J., 6: 621-639, 1966.

[2] R. Glaser, The shape of red blood cells as a function of membrane potential and temperature, J. Membrane Biol., 51: 217-228, 1979.

[3] K. Murata, K. Mitsuoka, T. Hirai, T. Walz, P. Agre, J.B. Heymann, A. Angel, Y. Fujiyoshi, Structural determinants of water permeation through aquaporin-1, Nature, 407: 599-605, 2000.

[4] I. Bernhardt, A.C. Hall, J.C. Ellory, Effects of low ionic strength media on passive human red cell monovalent cation transport, J. Physiol.-London, 434: 489-506, 1991.

[5] J.C. Parker, In defence of cell volume, Am. J. Physiol.-Cell Ph., 265: C1191-C1200, 1993.

[6] C.W. O'Neill, Physiological significance of volume-regulatory transporters, Am. J. Physiol.-Cell Ph., 276: C955-C1011, 1999.

[7] R. Glaser, J. Donath, Stationary ionic states in human red blood cells, Bioelectroch. Bioener.,13: 71-83, 1984.

[10] L.K. Laidler, J.H. Meiser, Physical Chemistry, Houghton Mifflin, Boston, 1995.

[11] M.M. Gedde, W.H. Huestis, Membrane potential and human erythrocytes shape, Biophys. J., 72: 1200-1233, 1997.

[12] A.L. Harris, C.C. Guthe, F. Van't Veer, D.F. Bohr, Temperature dependence and bi-directional cation fluxes in red blood cells from spontaneously hypertensive rats. Hypertension, 6: 42-48, 1984.

[13] J. Chuaibamrung (Sudrisi), Influence of cell shape and cell volume on cytoplasmic conductivity of human red blood cells, Journal of Microscopy Society of Thailand, 23: 1-6, 2009.

[14] R. Glaser, Biophysics, Springer, Berlin, Germany, 2000.

[15] P.S. Nobel, Physicochemical and Environmental Plant Physiology, fourth ed., Academic Press, Amsterdam & Boston, 2009.

[16] N. Sperelakis, Cell physiology, Academic Press, San Diego, USA, 1995.

[17] J. Seidl, R. Knuechel, L.A. Kunz-Schughart, Evaluation of membrane physiology following fluorescence activated or magnetic cell separation, Cytometry, 36:102-111, 1999.

[18] G. Fuhr, R. Glaser, R. Hagedorn, Rotation of dielectrics in a rotating electric high-frequency-field: Model experiments and theoretical explanation of the rotation effect of living cells, Biophys. J., 49: 395, 1986.

[19] J. Sudsiri, D. Wachner, J. Donath, J. Gimsa, Can molecular properties of human red blood cells be accessed by electrorotation? Songklanakarin J. Sci. Technol., 24: 785-789, 2002.

[20] J. Krupa, J. Terlecki, A Nondestructive Method for Measuring Electrical Conductivity of intracellular Matter of Tissue *in situ*, Rad. and Environm. Biophys., 13: 79-88, 1976.

[21] K. Asami, T. Yamaguchi, Dielectric spectroscopy of plant protoplasts, Biophys. J., 63:1493-1499, 1992.

[22] R. Hölzel, I. Lamprecht, Dielectric properties of yeast cells as determined by electrorotation, Biochim. Biophys.,Acta 1104:195-200, 1992.

[23] R. Hölzel, Electrorotation of Single Yeast Cells at Frequencies Between 100 Hz and 1.6 GHz, Biophys J., 73: 1103-1109, 1997.

[24] J. Suehiro, R. Hamada, D. Noutomi, M. Shutou, M. Hara, Selective detection of viable bacteria using dielectrophoretic impedance measurement method, J. Electrostat., 57:157-168, 2003

[25] J. Gimsa, T. Mueller, T. Schnelle, G. Fuhr, Dielectric spectroscopic of single human erythrocytes at physiological ionic strength: dispersion of cytoplasm, Biophys. J., 71: 495-506, 1996.

[26] J. Sudsiri, D. Wachner, J. Gimsa, On the temperature dependence of the dielectric membrane properties of human red blood cells, Bioelectrochemistry,70: 134-140, 2007.

Acknowledgements

J.Ch.S. is grateful for a stipend and financial support for this project from Prince of Songkla University, Thailand. The authors would like to give special thanks to Suratthani Hospital for providing some blood for doing this study.

Development of the infrared images processing algorithm for the automatic detection of the early stage of periodontal disease

L.O. Akulenko[1], A.V. Kolpakov[1]

[1]Biotechnical Medical Systems (BME-1) dept, Bauman Moscow State Technical University, 2 nd Baumanskaja St. n°5, bld 1, Moscow, 105005, Russian Federation

Contact: kolpakovalexx@yandex.ru

Introduction

According to the WHO, inflammatory periodontal diseases occur in 90-95% of the adult population and lead to pathological changes in the dentoalveolar system [1].

Diagnosis is more based on visual examination of the oral cavity and index evaluation of the soft tissue periodontal conditions and is subjective. In most cases, patients already diagnosed with signs of inflammatory diseases are diagnosed, diagnosis at an early stage of inflammation causes signifiсВнесиant difficulties, since there are no clinical manifestations of the inflammatory process [2-5].

As a result of previous studies, the possibility of visualization of the foci of inflammation of soft periodontal tissue (hereinafter – SPT) at an early stage has been established [1-8].

The purpose of this study is the development and testing of an algorithm for the automatic detection of foci of inflammation in the IR images of SPT. In the course of the research, the following tasks were set and solved:
– the effectiveness of segmentation algorithms is investigated when inflammation foci are detected at various stages of the inflammatory process;
– an assessment of the quality of the algorithm for automatic detection of inflammatory foci on the IR images of SPT was carried out.

Materials and Methods

The study was carried out using a verified database of 150 IR images of SPT at various stages of the inflammatory process, formed as a result of previous studies [7]. The Database contains of 20 IR images of Intact SPT, 70 IR images of the stage of the SPT early inflammation and 60 IR images of the stage of the SPT severe inflammation.
The choice of informative parameters of inflammatory foci is expedient to be carried out taking into account the laws of visual perception. High contrast of the object with the background is easier to perceive with the eye, which allows to identify the primary symptoms of the inflammatory process on the IR images of the SPT. The contrast in its turn is due to the intensity differences in the image. Thus, to determine the distinctive features of the inflammatory foci, the parameters characterizing the spatial distribution of the energy of inflammatory foci in the IR images of the SPT are analyzed, see tab. 1.

Table 1: Contents of the IR image of SPT database

№	The parameter (p_i)	Formula for calculation	Notation
1	Average intensity	$I_m = \frac{1}{N}\sum_{i=1}^{N} I_i$	I_i – intensity of the i-th element of the image
2	Selective SD	$S_I = \frac{1}{N}\sum_{i=1}^{N}(I_i - I_{cp})^2$	
3	Coefficient of contrast at the border of the focus of inflammation of SPT	$C_a = \frac{I_{\max} - I_{\min}}{I_{\max} + I_{\min}}$	I_{max}, I_{min} – the maximum and minimum modes of intensity histogram
4	Modulus of gradient on the border of the inflammatory focus of SPT	$G = \sqrt{G_x^2 + G_y^2}$	G_x=dI/dx, G_y=dI/dy are the intensity gradients in the horizontal and vertical directions, respectively
5	The ratio of average intensities	$r = \frac{I_m}{I_o}$	I_o is the average intensity of the image

In the course of the studies it was established that the IR images of the SPT at the stage of early and severe inflammation differ from intact tissues by the mean intensity I_m, the selective mean square deviation S_I, the contrast coefficient at the border of the inflammatory focus of the SPT Ca, the gradient modulus at the border of the inflammatory focus of the SPT G and the ratio average intensities r, see tab. 2.

Table 2: Values of informative parameters of inflammatory foci on IR images of SPT

№	Parameters			
		Intact tissues	early inflammation	severe inflammation
1	I_m	0,39± 0,04	0,36± 0,01	0,71± 0,02
2	S_I	0,03± 0,01	$(70\pm 1)10^{-3}$	$(60\pm 1)10^{-3}$

3	*Ca*	0,33± 0,02	0,54± 0,02	0,55± 0,15
4	*G*	(18± 3)10^{-4}	(50± 1)10^{-4}	(48± 1)10^{-4}
5	*r*	1,18± 0,18	1,82± 0,18	3,68± 0,78

There were threshold segmenation with the parameters C_a, G, and a watershed method applied for automatic segmentation of the centers of an inflammation on IR images of SPT.
The calculation of I_m, S_I and r were carried out within the investigated area of the potential focus of inflammation, and for G and Ca – outside. If the obtained values of informative parameters belong to the confidence intervals of the foci of inflammation, then the region was classified as a foci of inflammation, if not, then intact tissues.
The evaluation of the segmentaion quality was carried out by calculating the relative error of the detection of foci for each of the algorithms:

$$k = 100 - \frac{S_a}{S_m} \cdot 100 \qquad (1)$$

where k is the relative error, S_a – the area of the focus of inflammation, obtained in the mode of automatic allocation using the considered segmentation algorithms, S_m - the area of the focus of inflammation, allocated manually. The S_a and S_m were determined by counting overall pixels quantity of the segmented areas. The smaller the relative error of the two areas, the more accurately the area of the focus of inflammation of the SPT is segmented.

Results

The results of the segmentaion quality estimation are presented in tab. 3.

Table 3: The value of the relative error

Algorithm	Stages of inflammation	
	Stage of early inflammation	Stage of severe inflammation
Threshold segmentaion using C_a	6,2%	3,15%
Threshold segmentaion using G	16,1%	32,3%
Watershed method	–	15,3%

Discussion

The segmentation algorithm modulating the gradient on the boundary of the focus of inflammation with the use of a sliding mask showed the highest relative segmentation error, because at the time of registration, artifacts, such as salivation, with a high modulus of the gradient appear on the IR images of the SPT, which in turn leads to the detection of regions that do not correspond to the centers of inflammation of the SPT .
The algorithm for segmentation of inflammatory foci on the basis of the watershed method showed good results when a stage of severe inflammation was detected on the IR images of SPT. Foci of early inflammation of SPT by the watershed method are not segmented, which makes it impossible to apply this algorithm as a universal method for segmentation of inflammatory foci for various stages of the inflammatory process of SPT.
The segmentation algorithm based on the contrast ratio at the boundary of the SPT inflammation focus with the use of a sliding mask is the best and provides the lowest relative segmentation error.

Conclusions

As a result of the study, it was established that the least relative error of segmentation of inflammatory foci on IR images of SPT provides an algorithm for automatically detecting inflammatory foci by the contrast ratio at the border of the SPT inflammation focus using a sliding mask.

References

[1] Gazhva S.I., Guluev R.S. Prevalence and intensity of inflammatory periodontal diseases (literature review) // Obozrenie. 2012. №1(75). P. 13-14
[2] Zorina O.A., Aimadinova H.C., Rebrikov D.V. Early diagnosis of periodontitis on the basis of the analysis of the relationship between clinical signs and molecular markers. News of science Proceedings of materials the international scientific conference. 2015. P. 374-376.
[3] Zorina O.A., Berkutova I.S., Sych M.Y. Monitoring the state of the microbiocenosis of the periodontal pocket in patients with chronic generalized and aggressive periodontitis. Actual directions of scientific research of the XXI century: theory and practice. 2013. № 1. P. 26-33.
[4] Grudyanov A.I., Dmitrieva N.A., Kurchaninova M.G., Krishtop V.V. Changes in the composition of the microflora of the dentogingival sulcus in the process of orthodontic treatment. In the collection: From the Faculty of Advanced Medical Education - to the Institute of Postgraduate Education: History and Achievements Materials of the Jubilee Scientific and Practical Conference on the 30th Anniversary of the Institute of Postgraduate Education IvGMA. Executive Editor A.E. Baklushin. 2015. P. 101-102
[5] Grudyanov A.I., Fomenko E.V. Methods of conservative treatment of inflammatory periodontal diseases. Moscow, 2013.
[6] Kolpakov A.V., Makarov A.L., Spiridonov I.N. The use of the method of infrared diaphanoscopy for assessing the state of soft tissues of the oral cavity in stomatology // Science and education: electronic scientific and technical publication. 2013.№12.P.297-306.
[7] Kolpakov A.V., Makarov A.L., Spiridonov I.N.. Investigation of the absorption of optical radiation by soft periodontal tissues // Science and education: electronic scientific and technical edition. 2014.№11.P.444-457
[8] Kolpakov A.V., Ydin I.N., Zorina O.A., Spiridonov I.N. Early detection of foci of inflammation in soft periodontal tissues with the help of infrared diaphanoscopy / / Medical technology. 2016. №2.P.10 – 13
[9] Bobkova A.O., Porshnev S.V., Zuzin V.V., Bobkov V.V., Investigation of methods for removing speckle noise on ultrasound images. 23rd International Conference "Computer Graphics and Sight - GraphCon 2015" - Vladivostok, Russia, Reports.

Algorithm for one-axis receiver of magnetic positioning system

E.A. Gerken[1], V.V. Grechikhin [2]
[1] Postgraduate, Platov South-Russian State Polytechnic University (NPI),
346428 Novocherkassk, Russia
[2] Dr.-Ing., associate professor, Platov South-Russian State Polytechnic University (NPI),
346428 Novocherkassk, Russia

Contact: elenagerken@yandex.ru

Introduction

Magnetic positioning method has found a lot of application in medicine. This is because the method does not require line of sight between a generator of magnetic field and a movable receiver, which makes it possible to use the receiver inside of patient's body.

The method also has a high accuracy, speed performance, reliability and ease of implementation, which allows to accurate determine the location and orientation of the surgical instrument in three-dimensional space in real time. Currently it is an essential prerequisite for many modern medical procedures.

Through the use of this method, complex inner surgical operations for the patient can become less dangerous because of reduction of possible number of errors by to constant high-precision tracing of invasive instruments.

The navigation and control of a medical instrument is achieved by determine location and orientation of miniature active receivers that are moved inside of patient's body together with an invasive instrument.

Magnetic positioning method is used in numerous applications within the area of biomedical engineering, such us ENT Surgery, laparoscopic surgery, thoracic surgery, simulation and surgeon performance. For example, Iustin et al. [1] developed EMT for real-time organ-positioning during radiotherapy of cancer tumors, Plotkin et al. [2] designed EMT for tracking of the human eye and used it to diagnose vestibular disorders, Seeberger R, Kane G, Hoffmann J, et al. [3] used EM device for navigation maxilla-facial surgery, H. Zhang et al. [4] developed EMT for abdominal interventions.

Method

The method of magnetic positioning is based on the generation of a magnetic field and measurement of the orthogonal components of this field by the movable sensor in the research area. The location and orientation of the movable sensor are determined by solving the system of equations.

For determining the field density at an arbitrary point in space, a magnetic field method of the circular current is used, which describes approximately the behavior of a small conducting body in a magnetic field. Since the distance to the observation point is many times greater than the dimensions of the sensor, the following expressions for the vector of the magnetic field strength in a spherical coordinate system is applied [5]

The main power characteristic of magnetic field is field density. The magnetic field at each point of space sets the dipole moment vector in a certain direction. This direction is taken as field density of the magnetic field at the same point.

For determing the field density at an arbitrary point of space, apply the method of circular current, which approximately describes the behavior of a small conducting body in a magnetic field. In connection with the fact that the distance to an observation point in many times larger than the dimensions of a receiver, then the field density in the three-dimensional coordinate system can be described by the following expression:

$$\overline{B} = rot(\overline{A}) = rot\left(\frac{\overline{m},\overline{r}}{r^3}\right) = \left[\overline{\nabla}, \frac{[\overline{m},\overline{r}]}{r^3}\right] = \left[\overline{\nabla}, \left[\overline{m}, \frac{\overline{r}}{r^3}\right]\right] \quad (1)$$

Where $\overline{A}$ is a magnetic vector potential, $\overline{m}$ is magnetic moment vector, $\overline{r}$ is distance vector between receiver and transmitter.

The right-hand side of the equation (1) can be represented in the next form:

$$B = \overline{m}\left(\overline{\nabla}, \frac{\overline{r}}{r^3}\right) - \frac{\overline{r}}{r^3}(\overline{\nabla}, \overline{m}) \quad (2)$$

In equation (2) the first term is zero, because

$$\left(\overline{\nabla}, \frac{\overline{r}}{r^3}\right) = div\left(\frac{\overline{r}}{r^3}\right) = div(\overline{H}_1) \quad (3)$$

Where $\overline{E}_1$ is magnetic field strength of a single point charge at the origin, in point $\overline{r}_1 = 0$. By the Gauss theorem in differential form $div(\overline{H}_1) = 4\pi\rho$, and for a single point charge at the origin we have $\rho = 0$ at all points except the point $\overline{r}_1 = 0$, therefore $div(\overline{H}_1) = 0$ at all points except the point $\overline{r}_1 = 0$, then:

$\left(\overline{\nabla}, \frac{\overline{r}}{r^3}\right) = 0$, at all points except the point $\overline{r}_1 = 0$.

Then the dipole field density:

$$B = \frac{1}{r^3}(\overline{\nabla}, \overline{m})\overline{r} - \overline{r}(\overline{\nabla}, \overline{m})\frac{1}{r^3} = \frac{1}{r^3}(\overline{\nabla}, \overline{m})\overline{r} - \\ -\overline{r}(\overline{\nabla}, \overline{m}, \frac{1}{r^3}) \quad (4)$$

In (4) the first term on the right is:

$$(\bar{\nabla},\bar{m})\bar{r} = \left(m_x \frac{\partial}{\partial x} + m_y \frac{\partial}{\partial y} + m_z \frac{\partial}{\partial z} \right) \times$$

$$\times \left(x\bar{i} + y\bar{j} + z\bar{k} \right) = m_x \frac{\partial}{\partial x} x\bar{i} + m_y \frac{\partial}{\partial y} y\bar{j} + \quad (5)$$

$$+ m_z \frac{\partial}{\partial z} z\bar{k} = m_x \bar{i} + m_y \bar{j} + m\bar{k}_z = \bar{m}.$$

Then use (5) in (2) and receive:

$$\bar{B} = -\frac{\bar{m}}{r^3} - \bar{r}(\bar{\nabla},\bar{m},\frac{1}{r^3}) \quad (6)$$

Then the second term in (6) can be transformed:

$$\bar{\nabla}\left(\frac{1}{r^3}\right) = \bar{\nabla}\left(\left(\frac{1}{r}\right)^3\right) = 3\left(\frac{1}{r}\right)^2 \bar{\nabla}\frac{1}{r} \quad (7)$$

Here $\bar{\nabla}\frac{1}{r} = -\frac{\bar{r}}{r^3}$ (8)

Then:

$$\bar{\nabla}\left(\frac{1}{r^3}\right) = 3\left(\frac{1}{r}\right)^2 \left(-\frac{\bar{r}}{r^3}\right) = -3\frac{\bar{r}}{r^5} \quad (9)$$

Substitute (9) in the expression for the magnetic field of a point magnetic dipole (1) and obtain:

$$\bar{B} = -\frac{\bar{m}}{r^3} - \bar{r}\left(\bar{m},-3\frac{\bar{r}}{r^3}\right) = 3\frac{(\bar{m},\bar{r})\bar{r}}{r^5} - \frac{\bar{m}}{r^3} \quad (10)$$

$\bar{B}_i = 3\frac{(\bar{m}_i,\bar{r})\bar{r}}{r^5} - \frac{\bar{m}_i}{r^3}$ - field density generated by the i-th transmitter.

$$B_i(x,y,z) = \left[B_{xi} B_{yi} B_{zi}\right] = \begin{bmatrix} B_{xi} \\ B_{yi} \\ B_{zi} \end{bmatrix} \frac{\mu_0}{4\pi}\left(\frac{3m_i r}{r^5} - \frac{m_i}{r^3}\right)$$

B_i - field density generated by the i-th transmitter along the axes X, Y, Z.

Where, $B_{xi}B_{yi}B_{zi}$ are the value of the axial components of the measured field density at the point where the receiver is, μ_0 is permeability of vacuum. $r = \left[x_i - x_0 \quad y_i - y_0 \quad z_i - z_0\right]$ is the difference between the previous and the current location of the receiver, where $x_0\ y_0\ z_0$ are previous coordinates of the receiver location relative to the axes *X*, *Y*, *Z*, and $x_i\ y_i\ z_i$ are current coordinates of the receiver location.

$$m_i = N_{tr} S_{tr} I_{tr} \begin{pmatrix} \sin\theta_i & \cos\theta_i \\ \sin\theta_i & \sin\varphi_i \\ \cos\theta_i & \end{pmatrix} \quad (11)$$

Where m_i is magnetic moment of the *i*-th transmitter, N_{tr} is number of turns in the transmitter winding, $S_{tr} = \pi R_{tr}^2$ is cross-sectional area of the transmitter, R_{tr} is radius of the transmitter coil, I_{tr} is current in the transmitter winding, θ_i is roll angle, φ_i is pitch angle.

The voltages pulses, induced in the receiver will be estimated basing on the known distribution of the electromagnetic field from the transmitters [6]:

$$U_{out} = -\omega_0 S_{sen}(\bar{B}_i \bar{n}_{sen}) \quad (12)$$

Where $n_{sen} = \left[n_x, n_y, n_z\right]$ is unit vector along the axes *X*, *Y*, *Z*; $S_{sen} = \pi R_{sen}^2$ is cross-sectional area of the receiver; R_{sen} is radius of the receiver coil; $\omega_0 = 2\pi f_0$ is angular frequency of the alternating current supplied to the transmitter.

Experimental setup

The magnetic positioning system is modeled using the Finite-Element-Method in ANSYS Maxwell for determining the sensor location in the three-dimensional space. This model includes the group of independent sources of magnetic field and the developed ferromodulation converter with pulse compensation. This converter can be used as a receiver.

Together with the results of the FEM simulation an experimental unit is designed. Fig. 1 presents the block structure of this unit.

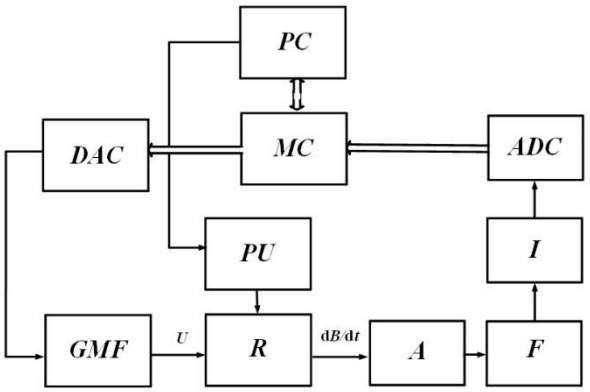

Figure 1: Block structure of experimental setup

Where *PC* is a personal computer, *MC* is a microcontroller, *DAC* is a digital-to-analog converter, *GMF* is a magnetic field generator, *PU* is a positioning unit, *A* is an amplifier, *I* is an integrator, *F* is filter, *ADC* is analog-to-digital converter.

PC controls operations of the entire positioning system and solves mathematical problems of determining the coordinates of the movable receiver. Estimation algorithm for determine the location and orientation of the movable receiver is implemented in the *MATLAB* environment.

MK sequentially connects independent sources of magnetic field to the power supply, controls the receiver's movement by supplying the control code to the positioning unit, obtains, records and transmits the values of the induced voltage pulses *U* in the receiver to the *PC*.

DAC converts digital codes from the *PC* into analog signals to control independent sources of magnetic field that are switches on circular for a short period of time (about 50-100 ms) and generate a magnetic field of known shape.

GMF consist of eight independent sources of magnetic field having the same orientations along axes of a fixed rectangular coordinate system and generating a magnetic field of known form with magnetic field strength in range of 100-150 A/m. Independent sources of the magnetic field are united in one structural element and are fixed in the given coordinate system *XYZ*.

PU is used like a reference system for motion estimation of receiver.

R get a signal from each independent source and induces voltage pulses directly proportional to the change in time of field density depending on the distance and angle between *i*-th source and receiver.

A intensify an output signal from the receiver.

F filters output signal from the receiver.

I integrates the output signal from the receiver.

ADC converts the output analog signal into a digital code.

System configuration

At present, various configurations of magnetic positioning systems are known, which use one, two or three receivers as the sensitive element of the system.

The most promising for medicine is the option with a single receiver, which overall dimensions must be minimal.

In that case, for determining the location and orientation of the single receiver in space, it is necessary to produce at least $N = 5$ independent measurements.

$$N(x, y, z, \theta, \phi) \tag{13}$$

Where, N is unit vector, x, y, z are coordinates of the receiver location relative to the *i*-th transmitter.

Determination of the receiver orientation in spherical coordinates is possible because of two variables θ and φ, yaw and pitch angles.

The configuration of the electromagnetic positioning system is selected from the conditions for solving the mathematical problem. For finding of five unknown coordinates of the movable receiver (13), it is necessary to have a minimum of five independent measurements. The following condition must be satisfied [7]:

$$L \cdot M \geq 5 \tag{14}$$

Where L is number of receivers, M is number of independent transmitters.

For finding of five unknown coordinates at one point in the three-dimensional coordinate system of research area, need to use the following solution:

$L = 1$, $M = 5$ (one receiver and five independent transmitters)

O'Donoghue et al [8] discusses the "blind zones" of the space under study and suggests using the following formula for calculating the optimum number of transmitters:

$$N(N+1)/2 \tag{15}$$

At the same time, Plotkin et al [9] showed using numerical simulation that the minimum number of transmitters providing continuous tracking of the receiver is eight, in addition, this design provides the best tracking accuracy for the transmitter in the research area. A schematic illustration of the developed magnetic positioning system containing one-axis receiver is shown on fig. 2.

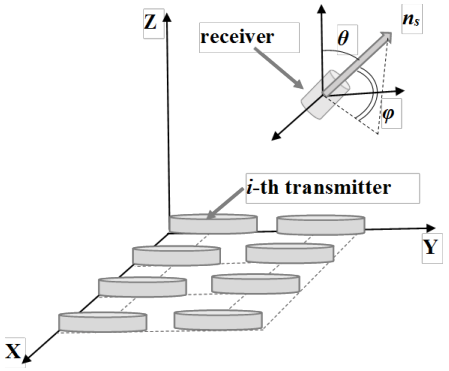

Figure 2: Model of magnetic positioning with five degrees of freedom

Receiver construction

The receiver sensing element is ferromodulation converter with pulse compensation which contain *C* made of low-coercitivity material with rectangular hysteresis loop *RHL*. *C* and *Wm* create a zero-organ whose principle of work based on using of limiting hysteresis loop nonlinearity of *C* material. *C* and *Wm* create a zero-organ whose principle work based on using of the nonlinearity of the limiting hysteresis loop of the core material. *Wc* works like an excitation and compensation winding at the same time, which consists of two identical windings Wc_1 and Wc_2 are wound opposite *W*m. Moreover, only Wc_1 is applied on *C*, Wc_2 on *S*. This condition allows to eliminate the parasitic connection between *Wc* and *Wm*. Construction of the receiver represent on fig. 3.

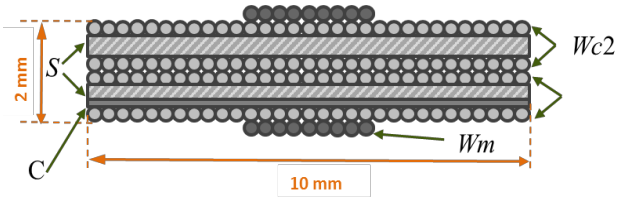

Figure 3: Construction of the receiver

Where, *Wc*2, *Wc*1 are compensating windings, *Wm* is measuring winding, *S* is non-magnetic substrate, *C* is a core.

However, the movable receiver in medical magnetic positioning systems must have minimal dimensions for placement in the patient's body. A design of a reduced size receiver is proposed, in which only one compensating winding is used. To eliminate parasitic connection, software correction is used.

In the software environment of ANSYS Maxwell, the magnetic state of the sensitive element of the primary magnetic field converter was simulated (fig. 4), the magnitude of the current creating the compensating field was calculated, and the minimum allowable diameter of the compensating winding wire.

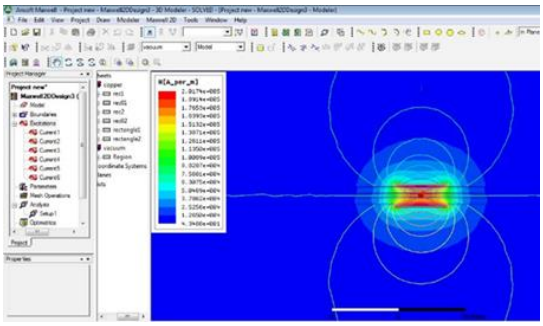

Figure 4: Simulation of converter magnetic state in Maxwell

Experimental research

The sensor receives a signal from each source and when the sensor's position or orientation change, the magnetic flux density *B* changes, too. In this case the voltage pulses *U* are induced inside the sensor. In terms of the magnitude and nature of the induced voltage pulses, the position and orientation of the sensor within the research area are calculated by means of the measuring block of the developed system.

During the experiment, the sensor and one of the source centers are on the same plane. The sensor is moved along this plane with a step width of 1 mm. The research area is 400 × 300 mm². At each point of this area, the voltage values induced in the sensor are measured, depending on the distance between the sensor and the source and the magnetic field strength (fig. 5).

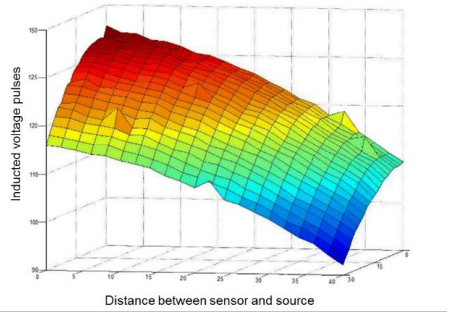

Figure 5: Static model of the inducted voltage pulses in receiver

After the identification of the static model in which each point is assigned to a certain voltage value, which is induced in the sensor, it is possible to move the sensor to a given point of the defined space.

In this case the sensor works as a zero-organ (an element of the automatic controller that generates a signal proportional to the difference of the compared values), comparing the induced values in the sensor with those assigned to certain coordinates.

Conclusions

The results of this research show a high accuracy. The interval of the induced voltage in the sensor after the measurement cycle at the same point in space do not exceed an error of 0.4%. It has been confirmed experimentally that the measurement error increases significantly with an increasing distance between the transmitter and the sensor. To increase the accuracy of positioning, it is proposed to use two sources where the sensor is located on the connecting axis between this two sources. In this case, the maximum value of the measurement error will be reduced significantly.

As a result of the research, algorithm of determine the position and orientation one-axis receiver in three-dimensional space in real time was realized by solving systems of equations. In response to the proposed approach, it was possible to minimize overall dimensions of receiver without loss of accuracy.

References

[1] R. Iustin, J. Linder, E. Isberg, T. Gustafsson, and B. Lenner-nas. A Model Based Positioning System. Patent. WO 2008/079071 A1, World Intellectual Property Organization, 2008.

[2] A Plotkin, O Shafrir, E Paperno, and D.M. Kaplan. Magnetic eye tracking: A new approach employing a planar transmit-ter. IEEE transactions on biomedical engineering, 57(5):1209–1215, March 2010.

[3] Seeberger R, Kane G, Hoffmann J, et al. “Accuracy assessment for navigated maxilla-facial surgery using an electro-magnetic tracking device.” Jurnal of Cranio-Maxillo-Facial Surgery, 2012, 40: 156-161

[4] H. Zhang et al., “Electromagnetic tracking for abdominal interventions in computer aided surgery”, Com-put. Aided Surgery, vol. 11, no. 3, pp. 127-136, May 2006

[5] Volkovitsky A.K., Karshakov E.V., Pavlov B.V. “Measure-ment of relative position of bodies in a magnetic field” Pro-ceedings of UTEOSS-2012 conference. - St. Petersburg. 2012, pp. 642-645 [4] C. J. De Luca. The use of surface electromyography in biomechanics. J Appl Biomech, 13(2):135–163, 1997.

[6] Bien, T., Rose, G., ‘‘Algorithm for calibration of the elec-tromagnetic tracking system,’’ Biomedical and Health In-formatics (BHI), pp. 85-88, 2012

[7] Zhelamsky M.V. “Electromagnetic positioning of moving objects”. - M.: FIZMATLIT, 2013 - 320.

[8] A. Plotkin and E. Paperno. 3-D magnetic tracking of a single subminiature coil with a large 2-D array of uniaxial transmitters. *IEEE Transactions on Magnetics*, 39(5):3295–3297, September 2003

[9] O'Donoghue K, Cantillon-Murphy P (2015) Planar magnetic shielding for use with electromagnetic tracking systems. IEEE Trans Magn 51(2):1–12

[10] Grechikhin V.V. Devices of the active control of magnetic characteristics for industrial process control of products made of ferromagnetic materials: the thesis of dissertation 05.13.05 - Novocherkassk, 2000.

Computational modelling of electroaerosol flows during external therapy

V.A. Karpukhin[1], K.S. Mustafina[1], G.S. Klimiashvili[1]

[1]Bauman Moscow State Technical University, 2-ya Baumanskaya str. 5, Moscow, Russia

Contact: christina.mustafina@gmail.com

Introduction

Burn injuries are one of the most important modern social and medical issue due to its prevalence, high death rate and considerable rate of temporary inability of working and primary disability [1]. Extensive burns cause huge losses of blood and weakness of the body therefore making sick man vulnerable to the infections which lead to inflammation [2].

Electroaerosol therapy is one of the methods of burns treatment. Exposing the burn wound to negatively charged medical aerosol particles. Under the impact of negative charge, the improvement of absorbability and pharmacologic properties of medical aerosols is occurred. It is known that thanks to negatively charged medical aerosols the perfusion is increased that helps with regeneration [3]. Moreover, electroaerosols have distinct bactericidal effect, they are able to inhibit the growth of various bacteria and fungi [4].

Unlike pharmacologic methods, electroaerosol therapy is less toxic and dangerous to body, and it is considered to be effective in burns treatment and allows considerably lower the dose of medicamental burden.

The aim of this study is the research of flow rates of electroaerosols in the workspace of the device of electroaerosol therapy.

Materials and Methods

Solving stated task, the geometrical model of device's workspace chamber, shown on fig. 1, was suggested. This model consists of air space (surfaces 5 and 6) between biological object (surface 7) and workspace chamber (surfaces 1 and 2), and ionizing electrode (surfaces 3 and 4).

To compute this model, we did assume that the flow of electroaerosols is laminar, it is modelled as Newtonian incompressible fluid, there are no particle coagulation and recombination of charges. We consider that the velocity of particles and air flow are equal, and electroaerosols are water spheres.

Flow rates of electroaerosols in workspace were computed using the following equations:

– Fick's convection and diffusion [5]:

$$\nabla \cdot (-D_i \nabla c_i - z_i \cdot mob \cdot F \cdot \nabla V) + + \vec{U} \cdot \nabla c_i = R_i, \quad (1)$$

$$N_i = -D_i \nabla c_i - z_i \cdot mob \cdot F \cdot \nabla V + \vec{U} c_i; \quad (2)$$

where c – consentration (mol/m^3), D – diffusion coefficient (m^2/s), z – ion's charge, mob – ion's mobility in an electric field (s·mol/kg), F – Faradey constant, R– reaction rate constant (mol/(m^3·s));

– Navier-Stokes' laminar flow [6]:

$$\frac{\partial \vec{U}}{\partial t} = \left(-\vec{U} \cdot \nabla\right)\vec{U} + \nu \Delta \vec{U} - \frac{1}{\rho}\nabla P + \vec{f} + \vec{g}, \quad (3)$$

$$\nabla \vec{U} = 0, \quad (4)$$

where $\vec{U}$ – velocity (m/s), υ – kinematic viscosity (m^2/s), ρ – density (kg/m^3), P – pressure (Pa), $\vec{f}$ – vector field of mass forces, $\vec{g}$ – gravitational acceleration;

– Electrostatics [7]:

$$\vec{E} = \nabla V, \quad (5)$$

$$\nabla \cdot \vec{D} = \rho_V, \quad (6)$$

where $\vec{D}$ – electric displacement field (C/m^2), ρ_V – spatial charge density (C/m^3), $\vec{E}$ – electric field (V/m), V – electric potential (V).

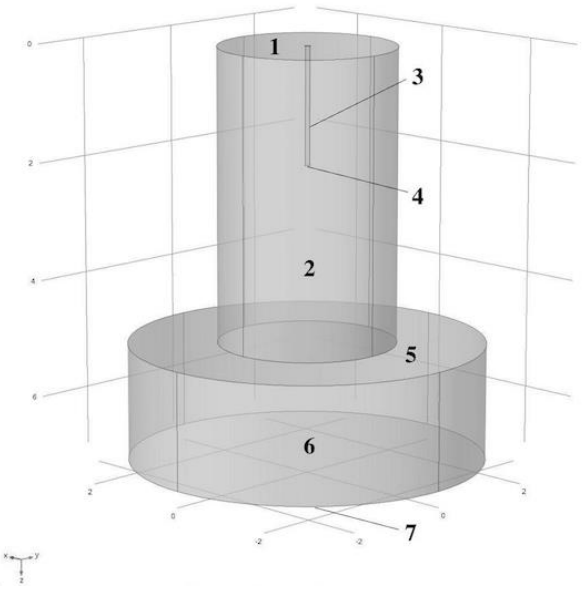

Figure 1: Geometrical model of device's workspace

To compute the ratio of electroaerosol particles on the bioobject's surface the following equations of forces affecting particles in the air flow were used [5, 6, 7]:

– Newton's law:

$$\frac{d(m_p v)}{dt} = F_t, \quad (7)$$

– Friction force:

$$F_D = \left(\frac{18\mu}{\rho_p d_p^2}\right) m_p(u - v), \quad (8)$$

– Brownian force

$$F = \zeta\sqrt{\frac{12\pi k_B \mu T r_p}{\Delta t}}, \quad (9)$$

– Electrostatic force

$$F = eZ(-\nabla V), \quad (10)$$

– Gravitational force

$$F_g = m_p g \frac{(\rho_p - \rho)}{\rho_p}, \quad (11)$$

where m_p – particle mass (kg), v – particle velocity (m/s), t – time (s), F_t – force affecting particle (N), u – airflow velocity (m/s), ρ_p – air density (kg/m^3), ρ_p – particle density (kg/m^3), d_p – particle diameter (m), μ – air dynamic viscosity (Pa·s), k_B – Boltzmann constant, T – absolute temperature (K), r_p– particle radius (m), ζ – proportionality coefficient.

All these equations were solved concurrently using finite-element methods.

To study the electroaerosol flow rates we did set the following boundary conditions: walls (surface 2) of workspace chamber and bioobject's surface (surface 7) are no slip; relative pressure at the inlet (surface 1) of workspace chamber *Pin*; relative pressure at the outlet (surfaces 5 and 6) of workspace chamber *Pout*=0; side walls (surface 2) of workspace chamber and bioobject's surface have zero potential (ground); potential on ionizing electrode (surfaces 3 and 4) is *U1*=-25 kV; zero charge on inlet and outlet (surfaces 1,5 and 6); initial particle concentration in an entire model is 0 mol/m^3; Inflow – surface 1 – concentration *Caer*=0 mol/m^3; concentration *Caer_m*=1,5·10^{-16} mol/m^3 on the edge (surface 4) of ionizing electrode; walls (surface 2) of workspace chamber and bioobject's surface (surface 7) are perfectly adsorbing walls – concentration *Caer*=0 mol/m^3; Outflow – surfaces 5 and 6.

Results

Trajectories of particles with diameters 10 um and 40 um while the workspace chamber is parallel to gravity force vector $\vec{g}$ were obtained, which are shown on figures 2 and 3. It is considerable that the bigger the diameter of particles is the greater quantity of them reaches the biobject's surface.

The effect of gravity force and particle diameter on electroaerosol flow particles ratio on bioobject's surface was studied in two workspace chamber's positions: vertical (chamber's axis was parallel to gravity force vector $\vec{g}$) or horizontal (chamber's axis was perpendicular to gravity force vector $\vec{g}$). We studied the dependence of diameter of electroaerosol particles and the part of electroaerosol particles reaching the bioobject's surface (particle ratio). The dependence is shown on figures 4 and 5.

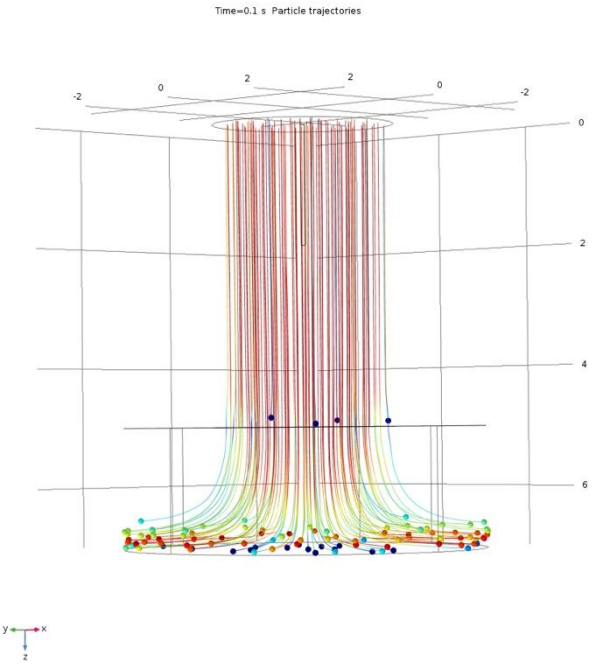

Figure 2: Trajectories of particles with diameter 10 um while the workspace chamber is parallel to gravity force vector $\vec{g}$

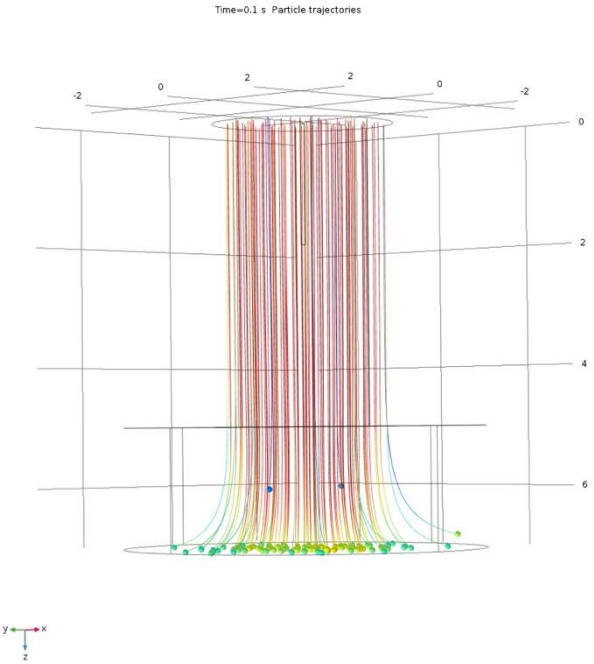

Figure 3: Trajectories of particles with diameter 40 um while the workspace chamber is parallel to gravity force vector $\vec{g}$

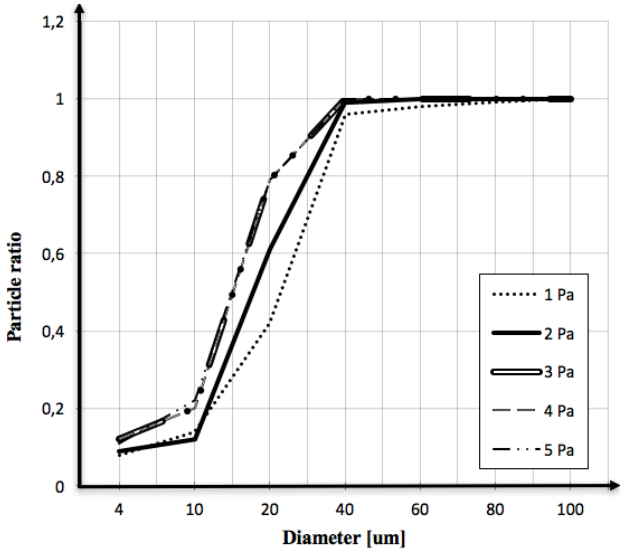

Figure 4: The dependence of particle ratio and diameter while the workspace chamber is parallel to gravity force vector $\vec{g}$

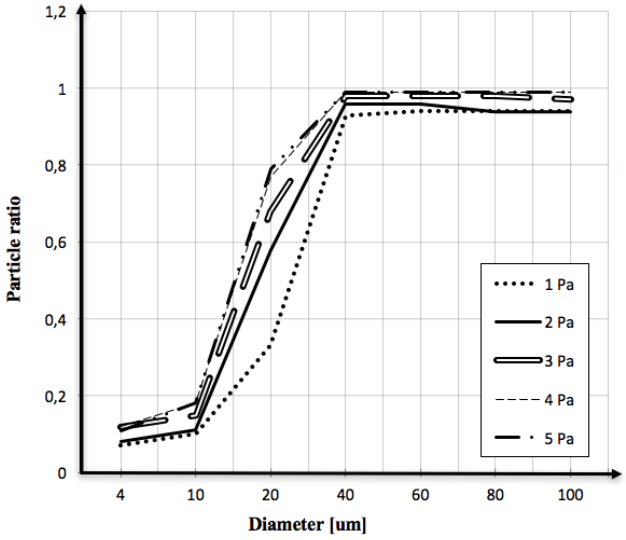

Figure 5: The dependence of particle ratio and diameter while the workspace chamber is perpendicular to gravity force vector $\vec{g}$

Conclusions

During the research, it was confirmed that electroaerosol particles with the diameter 40 um and more reach the burned bioobject's surface the most effectively independently of the workspace chamber position. Recommended input pressure is 3 and more Pa because it provides greatest quantity of electroaerosol particles on burned bioobject's surface.

References

[1] T. A. Spanholtz, P. Theodorou, P. Amini, G. Spilker. Severe burn injuries. Acute and long-term treatment. Deutsches Arzteblatt Int, 106(38): 607–613, 2009.

[2] M. G. Jeschke, D. L. Chinkes, C. C. Finnerty et al. The pathophysiologic response to severe burn injury. Ann Surg, 248(3): 387–401, 2008.

[3] A. N. Sheina. Aerosolterapiya. Kremlyovskaya medicina (klinicheskiy vestnik), 1: 154–160, 2014.

[4] Xiaoxia Xie, Lei Chen, Zhao-Qiang Zhang et al. Clinical study on the treatment of chronic wound with negatively-charged aerosol. Int J Clin Exp Med, 6(8): 649–654, 2013.

[5] E. M. Harding Jr., E. J. Berg, R. J. Robinson. Diffusion in replica healthy and emphysematous alveolar models using computational fluid dynamics. ISRN Biomedical Engineering, 2013.

[6] M.S. El-Genk, Yang In-Hwan. A numerical analysis of laminar flow in micro-tubes with a slip boundary. Energy Convers Manag, 50: 1481–1490, 2009.

[7] H. Labair, S. Touhami, A. Tilmatine et al. Study of charged particles trajectories in free-fall electrostatic separators. J. Electrostat. 2017.

[8] G.M. Hidy. Aerosols. Encyclopedia of Physical Science and Technology (Third Edition). 2003.

Experimental study of the mechanical properties of materials for physical modelling of biological tissues

I.V. Khaydukova, N.V. Belikov, A.M. Rezvanova, G.V. Savrasov

BMSTU/ Department « Biomedical Technical Systems », Baumanskaya 2-ya, 5/1, Moscow, Russia
Contact: irina.khaydukova@mail.ru

Introduction

Testing of the different modes of surgical devices includes tests on autopsy material. In this case, the major limitations are difficult biological samples acquisition, the heterogeneity of tissue properties and the dependence of mechanical properties on storage time and temperature.

An alternative to testing on autopsy materials is the modeling of surgical intervention. Modeling can be physical, analytical and computer-simulated.

Computer-simulated modeling (finite element analysis) has the advantage of unlimited ranges of parameter changes in the study. However, the parameters for the analysis are rarely fully described for biological tissues. Also, the computer modeling is a solution to a simplified task, which do not reflect all processes occurring in a real operation. Analytical modeling offers investigation of mathematical models of biological tissues, but the modeling of surgical exposure is also simplified.

Physical modeling offers a possibility to study the effect of surgical intervention on the physical model of tissue (phantom). The physical model simulates the target tissue. It is made from material that fits best the required criteria, for example the Young's modulus. Therefore, in tests on blood vessels, for example, it would be much easier to have a model that could mimic the physical vascular properties.

A paper review of the values of the Young's modulus for various vessels and their layers showed that according to [1], the static Young's modulus of the coronary artery is 2.3 MPa with a tensile pressure of 100 mm Hg. For the abdominal aorta the Young's modulus lies in the range from 0.1 MPa to 1.2 MPa at a tensile pressure from 1 mm Hg. to 90 mm Hg. [2]. According to [3], the Young's modulus of the coronary artery in men, depending on age, lies in the range from 0.9 MPa to 5 MPa. For women, the range is from 0.9 MPa to 4 MPa.

Physical models allow tests on large volumes of samples, in comparison with the autopsy material. Homogeneity of phantom properties increases the repeatability of results. The method of physical modeling allows to more accurately estimate the influence on tissue comparing to analytical and finite element modeling.

Materials used for physical modeling are often made by mixing two components: the main component (MC) and the supplementary one. When the ratio of MC in the mixture changes, the mechanical properties of the model also change. In this paper, the criterion for the similarity of material and biological tissue are mechanical characteristics. The main mechanical characteristic of the material is the Young's modulus, so the selection of the material is based on the correspondence of the Young's modulus to the real tissues.

For some materials, there is a wide range of values. It is due to the dependence of the mechanical properties on the ratio of mixing components in it. Ranges of possible values of the Young's modulus for some materials are presented in Fig. 1. [4]

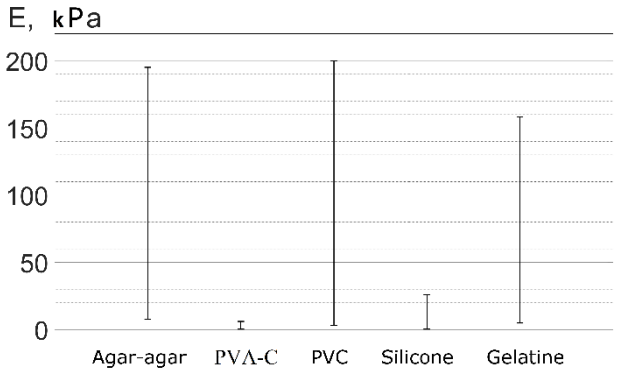

Figure 1: Mechanical properties of phantom materials

In [5] the Young's modulus for pure gelatin with concentrations of 25-30% was calculated. The range of values is 0.07-0.1 MPa. In [6] the values of the Young's modulus for gelatin mixtures are 0.4 kPa for gelatin-water mixture, 0.8 kPa for gelatin-water-sugar, 0.6 kPa for gelatin-water-sugar-citric acid.

In [7], there are dependences of the Young's modulus of gelatin and agar-agar on their concentrations $E_{gel} = 0,349 \cdot C^{1,87}$, $E_{agar} = 0,0034 \cdot C^{2,09}$, where C is the concentration in g/l of gelatin and agar-agar, respectively. Although, the chosen ranges of concentrations were not justified and these equations are applicable only within these ranges.

Taking into account the dependence of the mechanical properties on the ratio of mixing components, the most accurate simulation of the mechanical properties of biological tissue is possible by choosing the material of the most suitable concentration.

It is useful to cover the widest possible range of material properties to be able to mimic any type of biological tissue using chosen materials. According to the data shown in the Fig. 1, it is wise to choose gelatin and silicone for the current study. Gelatin is the most widely used material for physical models and therefore its mechanical properties at different concentrations are very useful to compare and refine the results of other studies. PVA-C could also be used

in this study but its drawback is a complex and long preparation procedure, especially for multi-layer structures. Unfortunately, biological tissues usually require multi-layer physical models.
However, as it was shown previously, in existing studies of the mechanical properties of materials for physical models, there is no clear dependence of the mechanical properties on the concentration under compression and stretch over the entire range of concentrations.
In this paper, we investigated the widest ranges of possible ratios of the components to be mixed when testing materials for compression and stretch. The dependence of the Young's modulus on concentration was investigated.

Materials and Methods

Materials

In the current work studies were conducted on gelatin and silicone. The dependence of the mechanical properties of these materials on the value of the mass fractions of their MC: gelatin and silicone gel, respectively, was investigated.
Mass fraction of MC can be expressed as:

$$\omega = \frac{m_{MC}}{m_{Mixture}} \times 100\% \qquad (1)$$

where m_{MC} is the mass of MC, $m_{Mixture}$ is the mass of the mixture.
The solution for the samples was made from gelatin ("Dr. Oetker" brand) by adding water at a temperature of 60-70°C. It was poured into cylindrical containers (for compression tests) or flat containers (for tension tests) and placed in the refrigerator (temperature + 4°C) for 6 hours until complete solidification. To facilitate the extraction of samples, the forms were pre-lubricated with petroleum jelly.
Gelatin was tested for compression with a mass fraction ranging from 2% to 50%. The tensile samples were tested with a mass fraction of MC ranging from 10% to 40%.
The types of silicones vary significantly from soft to hard ones, the latest can be used for example for tires production. To simulate biological tissue, that is rather fragile, we searched the softest silicone. To measure the hardness of low-modulus materials (plastics, elastomers, rubbers, etc.),

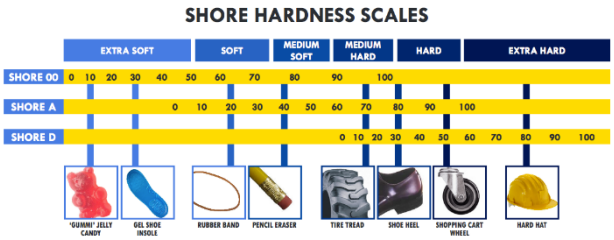

a Shore hardness scale is used (fig. 2) [8].

Figure 2: Shore hardness scale

From fig. 2 the softest silicone (Extra soft) is type 00. But silicones of this type are too expensive, therefore, type A was chosen for the tests. Among this type, a silicone compound Alcorsil 315 based on tin was chosen, its technical characteristics are given in the tab. 1. Compound consists of two parts - silicone gel (part A) and hardener (part B).

Table 1: Parameters of Silicone Alcorsil 315

Parameters	**Values**
Ratio by weight	100 A: 5 B
Viscosity of the mixture, cP	10,000 ± 2000
Life time	20-40 min
Curing time, at 23 ° C	4-6 hours
Shore A / D hardness	15 ± 2 A
Density, g / cm3	1.08
Tensile strength, MPa	≥2.75
Breaking strength, MPa	≥1.77
Elongation at break,%	≥363
Linear shrinkage,%	<1

From tab. 1, the recommended ratio of weight parts (A:B) is 20:1. the upper and lower limits of silicone hardening were investigated within ± 900%, which is from 1:1 to 200:1.
For ease of mixing, the mass ratio was converted into a volume ratio. Corresponding component densities: ρ_A = 1,125 g / cm^3, ρ_B = 0,96 g / cm^3.
The solidification threshold ratio was investigated in droplets of small volumes. The suitable lower limit of volume ratio was 2:1 and the upper limit was 40:1. At lower ratios, a homogeneous compound was impossible to achieve due to instant solidification. At larger ratios no solidification occurred even after 24 hours. The later studies showed that samples with ratios 2:1 and 3:1 did not solidify in the syringe, but only in air and therefore were also excluded from the experiment.
Thus, Alcorsil 315 was tested within the range of a mass fraction of 75 - 97.6% for tensile and 80 - 97.6% for compression.
All samples were divided into groups by material, type of test and mass fraction of MC. Each group contained 3-5 samples.

Methods

For compression, the samples were made in form of cylinders 10 mm long. The nature of the destruction of gelatin samples in compression tests depended on the concentration of MC. Low concentration samples typically split into 3-5 pieces, while high concentrations samples crushed. Dumbbell samples for tensile tests were cut with a die. During the stretching, the wide part of the sample slipped out of the clamps; therefore, to increase the friction pieces of insulating tape were glued for the gelatin samples and adhesive tape for the silicone samples (figure 3). The rupture of the silicone samples occurred layer by layer.

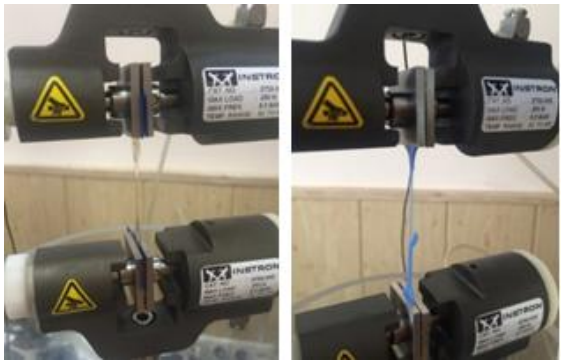

Figure 3: Stretching test of gelatin (left) and silicone (right) samples.

The thickness of the samples was measured with a micrometer. In the test on the Instron 3365 test machine, the dependence of the force on elongation was recorded. Then, from the experimental data, the dependence of the stress on the deformation was calculated as follows:

$$\sigma = \frac{F}{S};\ \varepsilon = \frac{\Delta l}{l} \qquad (2)$$

where F is the registered force, S - initial cross-sectional area of the sample, Δl - elongation, l -initial length.
The Young's modulus was calculated in the linear section of the stress-strain curve.

Results

The dependence of the average values of the Young's modulus on the mass fraction of MC for each group is shown in figures 4-7. There were 4 different groups for two types of materials and two types of tests: tension and compression.
The average value of the Young's modulus for each mass fraction is showed by an asterisk. The exact values are shown by red crosses. The error bars show the confidence interval of 95% for each mass fraction.
The average values for each group were approximated for best visualization. The lowest possible order of approximation was chosen. The order of approximation varies between different groups.

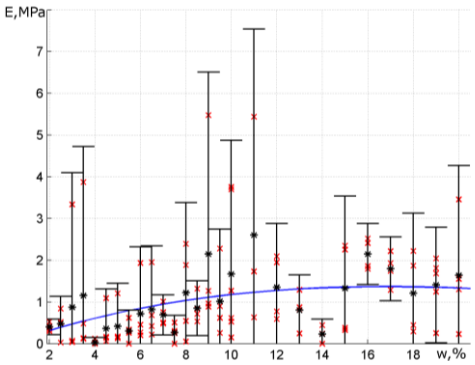

Figure 4: Dependence of the Young's modulus on gelatin concentration under compression

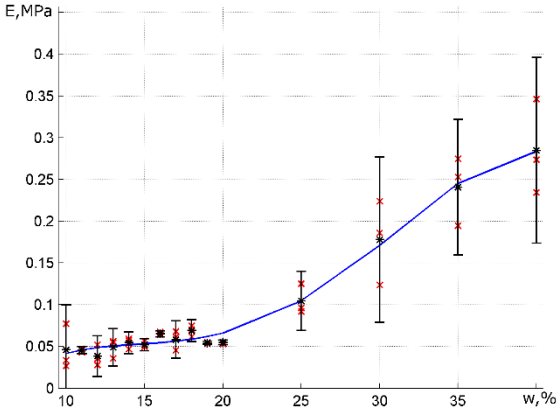

Figure 5: Dependence of the Young's modulus on gelatin concentration in tension

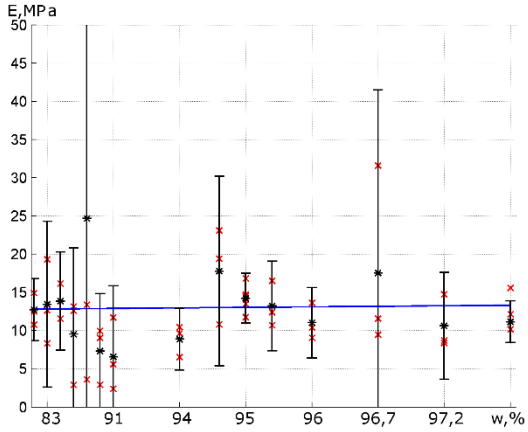

Figure 6: Dependence of the Young's modulus on silicone concentration under compression

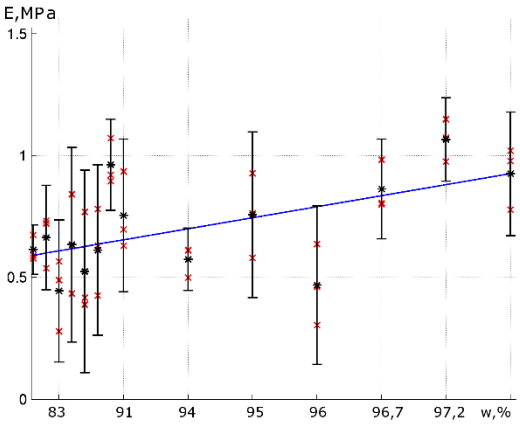

Figure 7: Dependence of the Young's modulus on silicone concentration in tension

Discussion

In this work materials for the physical modelling of biological tissues were tested under compression and stretch to find the strength properties, depending on the mass fraction of MC. The results for each group of samples were approximated.

This work allows to choose to the right concentration of material to get the physical model with exact physical properties of the target tissue.

As expected, the dependence of the Young's modulus on the mass fraction of silicone is more linear than for gelatin, which conforms well the literature review. Its Young's modulus is closer to vascular tissue so for vascular physical models it fits better. Also, silicone characteristics do not change with time and, most importantly, do not depend on temperature changes. This fact confirms the expediency of using silicone for modeling biological tissues.

According to the graphic results, we conclude that the dependence of the Young's modulus on the mass fraction for silicone is insignificant. Thus, it is necessary to choose a silicone with the Young's modulus that closely matches the parameters of the target tissue.

Gelatin required not only the exact conditions of storage and preparation, but it also quickly lost its properties due to drying or melting. Gelatin is good for model making because of its high variability of parameters. This makes it suitable for modeling a wide range of materials.

However, it should be noted that these materials are not suitable for vascular models. If we develop a blood vessel model we should use harder silicones or gelatin mixtures.

These mechanical properties were investigated only in the linear portion of the stress-strain curves. This does not fully describe the nonlinear behavior of the material. Materials for physical modeling behave nonlinearly, like biological tissues [9]. Thus, it is also planned to study nonlinear mechanical properties of materials for physical modeling for the fine selection of material concentration to model specific tissues.

References

[1] Gow, B. S., & Hadfield, C. D. The elasticity of canine and human coronary arteries with reference to postmortem changes. Circulation research, 45(5):588-594, 1979.

[2] Drangova, M., Holdsworth, D. W., Boyd, C. J., Dunmore, P. J., Roach, M. R., & Fenster, A. Elasticity and geometry measurements of vascular specimens using a high-resolution laboratory CT scanner. Physiological measurement, 14(3): 277, 1993

[3] Kasjanovs, V., Ozolanta, I., & Purina, B. Features of biomechanical properties of human coronary arteries. Mechanics of composite materials, 35(2):155-168, 1999

[4] Hungr, N., Long, J. A., Beix, V., & Troccaz, J. A realistic deformable prostate phantom for multimodal imaging and needle-insertion procedures. Medical physics, 39(4):2031-2041, 2012

[5] Cheremnykh, A. V., Gladkov, A. S., Afonkin, A. M., Pothekhina, I. A., Serebryakov, E. V., Kuzmin, I. V. Modeling of the stress-strain state in the vicinity of the fault node of the kimberlite pipe area "Mir" (the Yakut diamond-bearing province) (Моделиро-вание напряженно-деформированного состояния в окрестностях разломного узла района кимберлитовой трубки «Мир»). Izvestiya SO RANS. Geology, prospecting and exploration of ore deposits. 1, 2014.

[6] Tysyuspova, B. B., Artykova, D. M., Tazhibaeva, S. M., Musabekov, K. B., Esimova, O. A. Structurization in pectin-containing food systems (Структурообразование в пектинсодержащих пищевых системах). Kazakh National University named after al-Farabi, Almaty, Kazakhstan

[7] Hall, T. J., Bilgen, M., Insana, M. F., & Krouskop, T. A. (1997). Phantom materials for elastography. IEEE transactions on ultrasonics, ferroelectrics, and frequency control, 44(6), 1355-1365.

[8] Taylor R. A Guide to Shore Durometers. Albright Silicone [Internet]. 2015 Jan [cited 2018 March 28];[about 1 p.]. Available from: https://albrightsilicone.com/a-guide-to-shore-durometers

[9] Fung, Yuan-cheng. Biomechanics: mechanical properties of living tissues. Springer Science & Business Media, 2013.

An approach for patient-specific hemodynamics modeling taking into account biomechanical properties of the cerebral artery

S.V. Frolov[1], S.V. Sindeev[1], A.Yu. Potlov[1], D. Liepsch[2]

[1]Tambov State Technical University, Sovetskaya street 106, Tambov, Russia
[2]Munich University of Applied Sciences, Lothstrasse 64, Munich, Germany
Contact: Sergej.frolov@gmail.com

Introduction

Hemodynamic conditions in cerebral arteries, especially at bends and bifurcations, play an important role in initiation, growth and rupture of cerebral aneurysms [1]. During the recent years a computational fluid dynamics (CFD) has been used by many researchers as a primary tool for investigation of cerebral circulation, focusing mainly on finding a correlation between flow conditions and genesis of cerebral disorders [2]. However, the CFD studies are limited by a rigid vessel wall assumption, e.g. [3–5], primarily due to the lack of patient-specific information about mechanical properties of the vessel wall.

Several groups have reported approaches for evaluation of mechanical properties of cerebral arteries utilizing modern non-invasive clinical techniques, such as intravascular ultrasound (ultrasound elastography) [6] and magnetic resonance elastography [7]. Despite of the promising results, a low spatial resolution of the aforementioned methods has a significant influence on estimated mechanical properties.

On the other hand, intravascular optical coherence tomography (OCT) seems to be a promising technique for high precision imaging of internal vessel wall structures and could be used for evaluation of mechanical properties of the cerebral arteries [8]. Moreover, feasibility studies of the use of OCT to perform elastography have shown a strong correlation existed between the mechanical measurements and those performed with OCT elastography, with no significant difference existing between the two techniques [9, 10].

In this study, we present a novel approach for a patient-specific mathematical modeling of hemodynamics taking into account individual biomechanical properties of the cerebral artery obtained by optical coherence elastography.

Materials and Methods

Conducting a patient-specific simulation of the cerebral circulation requires an individualization of a general mathematical model of hemodynamics [5], based on three-dimensional governing equations, by clinically available patient's data.

Patient-specific mathematical modeling of hemodynamics

Geometrical model: The individual geometry of a cerebral artery has a significant influence on distribution of hemodynamic parameters, especially velocity and wall shear stress (WSS), and should be taken into account in CFD studies. To obtain the individual geometry of the artery various medical imaging techniques could be used, such as magnetic resonance imaging (MRI) and computed tomography (CT), e.g., see fig. 1. A surface, obtained by initial segmentation of available DICOM data, should be further post-processed to be used to generate a computational domain by smoothing, treating of irregular elements, etc.

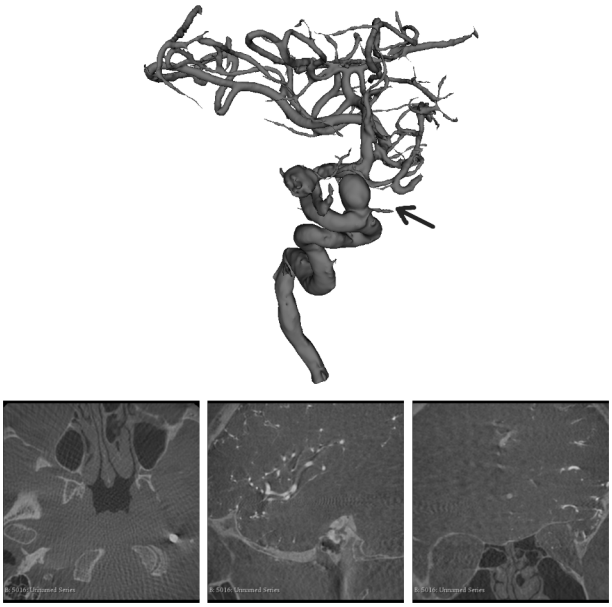

Figure 1: An example of segmented cerebral vasculature (top) with aneurysm (arrow) and clinical visualization data (bottom)

Boundary conditions: A patient-specific flow rate curve for the studied cerebral artery could be measured by Doppler ultrasound and imposed as an inlet boundary condition. An outlet pressure curve is often not available and therefore a free outflow condition could be used for outlets [11].

Blood rheology: The effect of blood rheology on distribution of hemodynamic parameters in cerebral arteries is comparably less then the effect of individual morphology; however, a presence of low shear rate zones and vortices in an aneurysm sac cause non-Newtonian fluid models to be used to represent blood [5, 12].

Vessel wall: In contrast to a healthy artery wall with a three-layered structure, an aneurysm wall is generally composed of only intima and adventitia; media is often damaged. Such specific internal wall structure, causing an aneurysm to be less distensible than arteries, as well as limitations of

in vivo measurement techniques, contribute to using a linear elastic model of a cerebral artery wall in the proposed approach.

Compression elastography for evaluation of biomechanical properties of the vessel wall

Contrary to a traditional approach assuming a rigid vessel wall, we consider artery as a deformable region taking into account individual biomechanical properties of the wall, which are evaluated by the compression elastography method based on OCT.

To evaluate biomechanical properties of the aneurysm wall a series of structural OCT images should be obtained for systolic and diastolic phases. After data filtering, a group of about one hundred control points are selected for comparison of B-scans. For each pair of control points (for systole and diastole) a displacement is calculated, i.e., local deformation of the vessel wall under a pulse wave. Thus, the Young's modulus E could be estimated as follows:

$$E = \frac{F_n}{S} \cdot \frac{l}{\Delta l}, \quad (1)$$

where F_n is a normal component of the deforming force F, which blood exerts on the vessel wall; S is an area under the force; l is longitudinal dimension of a deformed region; Δl is an averaged relative longitudinal deformation for local regions of the vessel wall. The following considerations could be taken into account to determine parameter values for Eq. 1. The force F could be evaluated by the difference between systolic and diastolic pressures. The length l could be assumed to be equal to the coherence probing depth, since it commensurates with an aneurysm wall thickness. For calculation of Δl only normal components of the deforming force F should be used.

Using similar considerations the Poisson's ratio μ could be found as follows:

$$\mu = \frac{\Delta d}{d} \cdot \frac{l}{\Delta l}, \quad (2)$$

where d is a transverse dimension of a deformed region (equals to the scan area size of the OCT system); Δd is an averaged relative transverse deformation of local regions of the vessel wall.

A phantom of cerebral artery with similar mechanical properties as for real intracranial artery was created to validate the proposed methods. The sculptural clay was used to make the mold. The phantom had a three-layered internal wall structure with different mechanical properties. To adjust the absorbing properties of the phantom structures a special dye "Evans Blue" (Biochem) was used. For adjusting of the scattering properties all layers contained microparticles of titanium dioxide in different concentrations.

Results

Figure 2 shows structural OCT images of the phantom of a cerebral artery before and after a deformation. Red and green areas mark displacements of dark and light regions

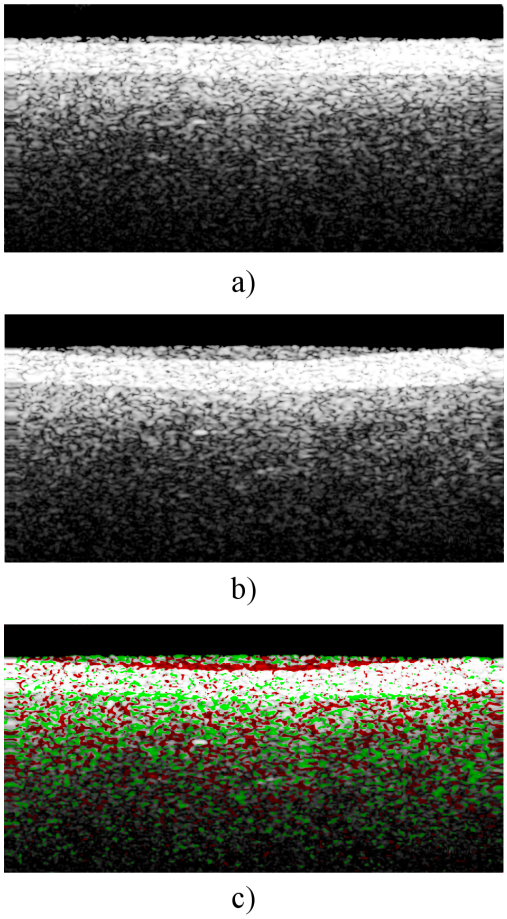

Figure 2: Structural OCT images of the cerebral vessel phantom before (a) and after (b) deformation; deformed regions are marked by red and green (c). Image size is 2.2 x 1.1 mm

of the OCT image respectively. The displacements were obtained by comparison of the structural OCT image at the systolic peak with the corresponding image at the diastolic end. The obtained average Young's modulus (1) and Poisson's ratio (2) were 1.03 MPa and 0.495 respectively, which are in agreement with available clinical data [13].

In the proposed workflow an individual geometry of the studied cerebral vessel along with individual biomechanical properties of the vessel wall are used for patient-specific evaluation of hemodynamic parameters in the cerebral artery (fig. 3). The main steps of the workflow could be represented as follows:

(1) Acquiring diagnostic images of patient's vasculature using clinical visualization techniques; extraction of individual geometrical 3D model of the cerebral artery with an aneurysm.

(2) Reconstruction of structural images of the cerebral artery wall using endoscopic OCT.

(3) Evaluation of biomechanical properties of the vessel wall using compression elastography.

(4) Setting up the mathematical models by adjusting mate-

rial's coefficients of the vessel wall and imposing patient-specific boundary conditions.
(5) Transient simulation of preoperative hemodynamics of the patient.
(6) Evaluation of three-dimensional distribution of velocity and pressure, computation of WSS and derived parameters (e.g., oscillatory shear index (OSI), time averaged wall shear stress (TAWSS), etc.).
(7) Analysis of obtained hemodynamic parameters in the cerebral artery.

Discussion

Information about mechanical properties of the cerebral artery wall provides physician a valuable support in assessment of various cerebral disorders and further treatment planning; however, in vivo evaluation of mechanical properties is challenging due to the limitations of available clinical visualization techniques.
Wittek et al. [14] proposed an approach for identification of artery material properties using time resolved 3D ultrasound. Despite of advances in identification of material properties of aortic walls, an application of the method for cerebral arteries is limited by low spatial resolution of an ultrasound device and visualization problems for structures within the skull.
Alternatively, in our study we propose using of minimally invasive endoscopic OCT method, providing a sufficient resolution for imaging of internal wall structures, for evaluation of cerebral artery material properties and further patient-specific numerical studies of cerebral circulation. It should be noted that, in vivo evaluation of the deforming force F is a complicated task and requires some workaround. The difference between systolic and diastolic pressures in the proposed approach could be estimated either by numerical simulation of blood flow in the artery with rigid walls or by direct measurement of blood pressure using an intravascular pressure sensor, e.g., dual-sensor guidewire ComboWire XT (Philips, Amsterdam, Netherlands). A detailed description of measurement procedure was reported by Schneiders et al. [15].
The proposed approach has some limitations. First, an aneurysm size should be at least two times larger than a diameter of forward-imaging OCT probe, which means that the approach is applicable only for cerebral aneurysms larger than 4 mm. Second, a construction of endoscopic OCT probe should be improved to allow an easy access to the studied segment of the cerebral circulation. Third, a cerebral artery wall is considered as a homogeneous material, assuming constant thickness, Young's modulus and Poisson's ratio along the vessel wall. Forth, a representation of a cerebral artery wall by a linear elastic model could lead to overestimation of vessel deformations during CFD simulations compared to non-linear models [16].
Presented methods and workflow are the results of ongoing study and further investigations should be done to address the listed limitations and prepare the proposed approach to be used as a part of standard clinical practice for individualized assessment of cerebral circulation disorders.

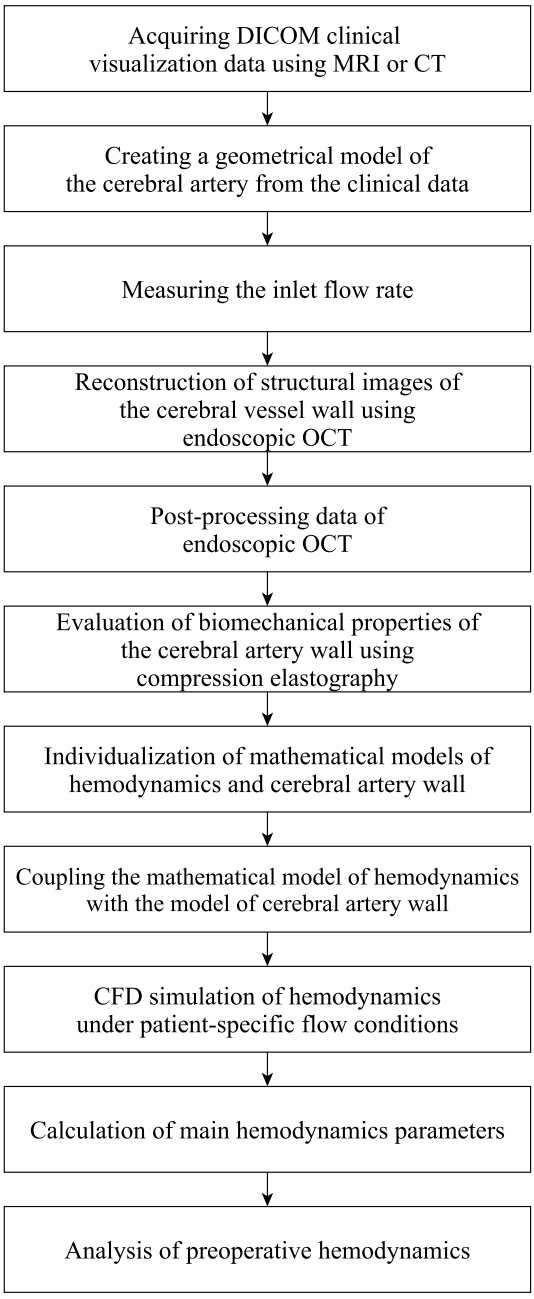

Figure 3: A workflow for patient-specific modeling of hemodynamics taking into account individual biomechanical properties of the cerebral artery

Conclusions

The proposed approach takes into account the individual biomechanical properties of the cerebral artery wall measured in vivo and has a potential to be used in clinical practice for improved patient-specific evaluation of hemodynamics in the cerebral artery with an aneurysm.

References

[1] C. Sadasivan, D. J. Fiorella, H. H. Woo, and B. B. Lieber. Physical factors effecting cerebral aneurysm pathophysiology. *Annals of Biomedical Engineering*, 41:1347–1365, 2013.

[2] D. M. Sforza, C. M. Putman, and J. R. Cebral. Computational fluid dynamics in brain aneurysms. *International Journal for Numerical Methods in Biomedical Engineering*, 28(6-7):801–808, 2011.

[3] K. Valen-Sendstad, M. Piccinelli, and D. A. Steinman. High-resolution computational fluid dynamics detects flow instabilities in the carotid siphon: Implications for aneurysm initiation and rupture? *Journal of Biomechanics*, 47(12):3210–3216, 2014.

[4] J. R. Cebral, F. Mut, J. Weir, and C. M. Putman. Association of hemodynamic characteristics and cerebral aneurysm rupture. *American Journal of Neuroradiology*, 32(2):264–270, 2010.

[5] S. V. Frolov, S. V. Sindeev, D. Liepsch, and A. Balasso. Experimental and CFD flow studies in an intracranial aneurysm model with Newtonian and non-Newtonian fluids. *Technology and Health Care*, 24:317–333, 2016.

[6] R. Fan, D. Tang, C. Yang, J. Zheng, R. Bach, L. Wang, D. Muccigrosso, K. Billiar, J. Zhu, G. Ma, A. Maehara, and G. S Mintz. Human coronary plaque wall thickness correlated positively with flow shear stress and negatively with plaque wall stress: an IVUS-based fluid-structure interaction multi-patient study. *BioMedical Engineering OnLine*, 13(1):32, 2014.

[7] Y. K. Mariappan, K. J. Glaser, and R. L. Ehman. Magnetic resonance elastography: A review. *Clinical Anatomy*, 23(5):497–511, 2010.

[8] T. Hoffmann, S. Glaßer, A. Boese, K. Brandstädter, T. Kalinski, O. Beuing, and M. Skalej. Experimental investigation of intravascular OCT for imaging of intracranial aneurysms. *International Journal of Computer Assisted Radiology and Surgery*, 11(2):231–241, 2015.

[9] K. V. Larin and D. D. Sampson. Optical coherence elastography – OCT at work in tissue biomechanics [invited]. *Biomedical Optics Express*, 8(2):1172, 2017.

[10] J. Rogowska, N. Patel, S. Plummer, and M. E. Brezinski. Quantitative optical coherence tomographic elastography: method for assessing arterial mechanical properties. *The British Journal of Radiology*, 79(945):707–711, 2006.

[11] Q. Sun, A. Groth, and T. Aach. Comprehensive validation of computational fluid dynamics simulations of in-vivo blood flow in patient-specific cerebral aneurysms. *Medical Physics*, 39(2):742–754, 2012.

[12] C. Fisher and J. S. Rossmann. Effect of non-Newtonian behavior on hemodynamics of cerebral aneurysms. *Journal of Biomechanical Engineering*, 131(9):091004, 2009.

[13] J.D. Humphrey and P.B. Canham. Structure, mechanical properties, and mechanics of intracranial saccular aneurysms. *Journal of Elasticity*, 61(1/3):49–81, 2000.

[14] A. Wittek, W. Derwich, K. Karatolios, C. P. Fritzen, S. Vogt, T. Schmitz-Rixen, and C. Blase. A finite element updating approach for identification of the anisotropic hyperelastic properties of normal and diseased aortic walls from 4D ultrasound strain imaging. *Journal of the Mechanical Behavior of Biomedical Materials*, 58:122–138, 2016.

[15] J. J. Schneiders, E. VanBavel, C. B. Majoie, S. P. Ferns, and R. van den Berg. A flow-diverting stent is not a pressure-diverting stent. *American Journal of Neuroradiology*, 34(1):E1–E4, 2011.

[16] M. Oshima and R. Torii. Numerical evaluation of elastic models in blood flow–arterial wall interaction. *International Journal of Computational Fluid Dynamics*, 20(3-4):223–228, 2006.

Acknowledgments

This work was supported by Russian Science Foundation (Project 16-15-10327).

Neural network approach to cell segmentation in immunocytochemical study

D.A.Parpulov[1], A.V.Samorodov[1], V.I.Iglovikov[2]
[1] Bauman Moscow State Technical University, Moscow, Russian Federation
[2] Lyft Inc., San Francisco, CA 94107, USA

Introduction

Immunocytochemical (ICH) study has a great importance in the evaluation of some predictive and prognostic factors in breast cancer (BC). The degree of C-erbB-2 oncoprotein expression is important for BC treatment strategy choice, because C-erbB-2 is a receptor for HER2/neu epidermal growth factor [6]. Overexpression of this oncoprotein is a risk factor of BC recurrence. The degree of membrane staining (qualitatively from 0 till 3+) represents tumor HER2 status in ICH study.

Now tumor HER2 status is evaluated manually by oncologist, doctor should check about 100-200 images of the specimen before giving the final assessment. Thus, the automation of determining tumor HER2 status is an urgent task, because it will allow to free an oncologist from routine work.

Automatization of tumor HER2 status assessment is divided into 2 subtasks: cells segmentation and automatic determining the degree of membrane staining. This work is devoted to the problem of cell segmentation.

For classical methods of computer vision the problem of cell segmentation is difficult due to the frequent presence of erythrocytic background and non-cellular elements at specimen image. In addition, the process of feature engineering for these algorithms is a time consuming and non-trivial. We propose segmentation algorithm, based on deep convolutional neural networks (CNN), which are very popular in image processing [1,5]. Using this approach, we got better results, than using classical computer vision algorithms.

Materials and Methods

Data

As input data for training algorithm we used biomedical images, obtained by hardware-software complex "Granat". Each color image has 1600 pixels at vertical and 1200 pixels at horizontal dimension. We prefer images with high and medium quality for manual segmentation. Images with bad quality were filtered from training dataset.

Selected images from different patients were manually segmented by an expert. Thus, for each image in training dataset we obtain binary image mask with correct result of cells segmentation. Training set contains about 300 manually segmented images. We use random crops and random angle rotations for training set augmentation.

Baseline segmentation algorithm

As a rule for algorithms comparison we need a simple algorithm, that succesfully solves our segmentation task. After that we evaluate this algorithm and use these results as a baseline to construct algorithm with better quality. Baseline segmentation algorithm has the following steps:

- image normalization;
- adaptive histogram equalization;
- Otsu binarization;
- morphological operations (remove small holes, remove small objects, image opening);
- connected components detection.

Neural network approach for cells segmentation

We train deep CNN with U-net like architecture for task of cells segmentation, because this architecture proved itself very useful for segmentation problems with limited amounts of data [4]. In general, the U-Net architecture consists of an encoder to capture context and a decoder that enables precise localization (Fig.1).
The contracting path follows the typical architecture of a CNN with convolution and pooling operations and progressively downsampled feature maps. Every step in the expansive path consists of an upsampling of the feature map followed by a convolution [4]. Hence, the expansive branch increases the resolution of the output. In order to localize, upsampled features in the expansive path are combined with the high-resolution features from the contracting path via skip-connections.

We also employ batch normalization technique to improve convergence during training. As encoder we use VGG-11 CNN [5] pretrained at Imagenet dataset [2].

We deploy CNN with this architecture on its own at python language in Pytorch framework.

This U-net-like CNN was trained during 100 epochs using stochastic gradient optimization method called “Adam” [3]. We check training progress at labeled validation dataset.

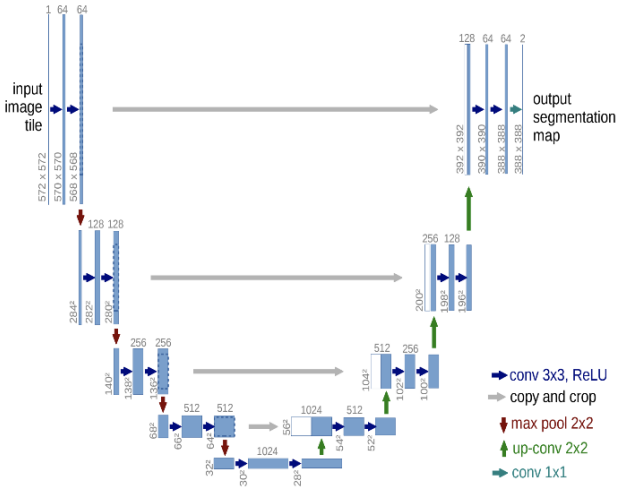

Figure 1: U-net architecture

Metric

We use Sørensen-Dice coefficient as metric. This metric shows similarity measure between true and predicted segmentation masks, like Jaccard coefficient.

$$Dice = \frac{2 * |True \cap Pred|}{|True| + |Pred|} \qquad (1)$$

It's worth noting that typically total cells' area at image is far fewer that total background area. The task of CNN is high accuracy cells' segmentation, not background segmentation. So, it's important to note that when we compute intersection and union in Dice coefficient formula (1), we take in consideration only masks for cells only (not total masks for image).

Additionally, we check relative frequencies of true negative and false positive cells detection. This information gives us more intuition about algorithm's weak points and helps for further improving of segmentation quality.

Results

The quality of the resulting model was evaluated on validation data set consisting of 60 images (by 15 images of each membrane coloring degree).

During results exploration we found that trained CNN frequently segment small objects as false positive cells. This problem can be solved by two ways: training set extension or removing small connected components. Training set extension requires additional time for manual labeling of images by expert. So, we decide to remove connected components that have area less than some empirically determined threshold. This trick enables to increase Dice coefficient a little bit (from 0.81 to 0.83 in average for validation set), because area of false positive cells is relatively small. But at the same time relative frequency of false positives decreased from 16.8% to 10.8%.

Final average value of Sorensen–Dice coefficient for neural network segmentation model at validation set is 0.83 ± 0.09. An example of image segmentation by CNN model is shown in Fig. 2.

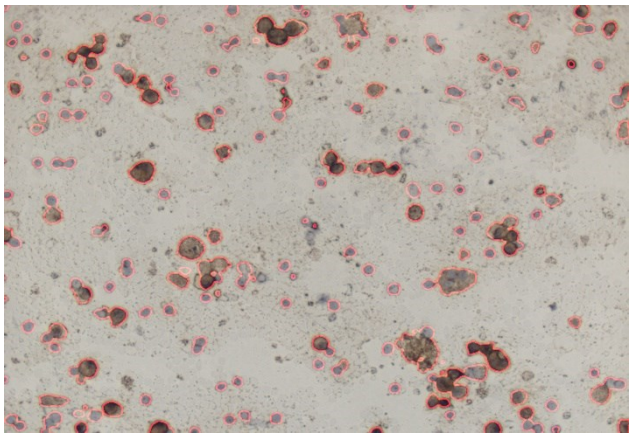

Figure 2: Image segmentation result

Simple baseline segmentation algorithm has 0.68 ± 0.16 average Dice coefficient on the validation data set.

Below you can see table with false positive and false negative rates for baseline and neural segmentation methods (Table 1).

Table 1: False Positive And False Negative Rates

Object	**False positive rate**	**False negative rate**
Baseline	23.8 ± 8.3%	2.7 ± 0.8%
Neural	10.8 ± 4.7%	2.5 ± 0.7%

Here we can see that CNN can significantly reduce false positive cells detection rate. The main reason is that CNN implicitly learns geometric and color features, which are specific just for cells.

Cell with complex background near it is another difficult case for baseline segmentation method. As a rule, it segments all «thrash» area with cells inside it (Fig.3). In contrast, neural segmentation method can distinguish cell from difficult background around it (Fig.4).

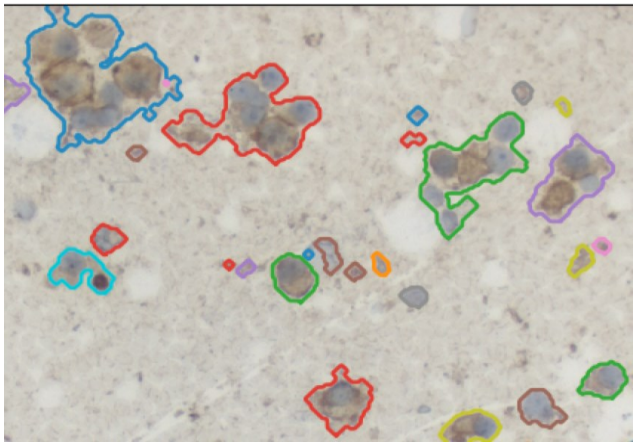

Figure 3: Segmentation result, obtained by baseline algorithm

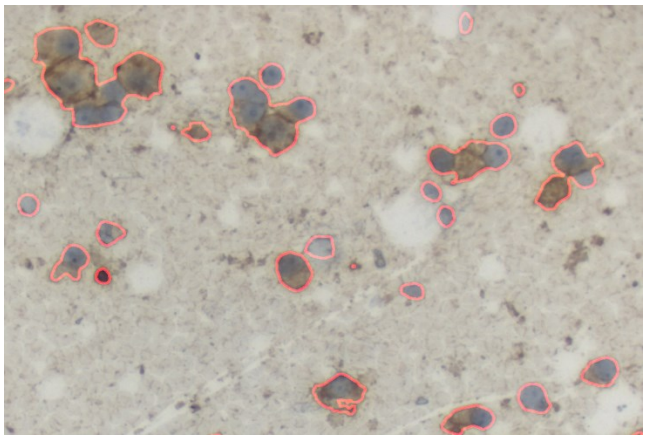

Figure 4: Segmentation result, obtained by neural network algorithm

Conclusions

In this paper, we propose a neural network approach for cells segmentation that solves the problem of tumor HER2 status assessment. Our model is based at U-net CNN with pretrained VGG-11 encoder.

It has been shown that CNN-based model works significantly better than classical computer vision segmentation algorithms, especially on difficult cases of images with complex background. In case of high quality images without non-cellular elementrs both kinds of algorithms work well with similar precision.

The main advantages of CNN-based model are:

- lower false positive cell detection rate;
- more precise cell segmentation at images with complex background;
- robustness to noise and image artifacts.

The main reason that CNN-based model works better than classical segmentation algorithm is that neural net implicitly learns geometric and color features specific just for cells. At the same time baseline model operates only with information at color and intensity levels, and this is not enough for high-quality segmentation in complex cases.

Thus, implementation of neural network segmentation algorithm can reduce false positive cell detection rate from 23.8 % to 10.8 % and improve Dice coefficient from 0.68 to 0.83. Deploying this model into production can simplify the routine work of oncologist for determining HER2 status of breast cancer tumors.

References

[1] Ching, T., Himmelstein, D.S., Beaulieu-Jones, B.K., Kalinin, A.A., Do, B.T., Way, G.P., Ferrero, E., Agapow, P.M., Xie, W., Rosen, G.L., et al.: Opportunities and obstacles for deep learning in biology and medicine. bioRxiv p. 142760 (2017)

[2] J. Deng, W. Dong, R. Socher, L.-J. Li, K. Li and L. Fei-Fei, ImageNet: A Large-Scale Hierarchical Image Database. IEEE Computer Vision and Pattern Recognition (CVPR), 2009

[3] Kingma, D., Ba, J.: Adam: A method for stochastic optimization. arXiv preprint arXiv:1412.6980 (2014) [4] C. J. De Luca. The use of surface electromyography in biomechanics. J Appl Biomech, 13(2):135–163, 1997.

[4] Ronneberger, O., Fischer, P., Brox, T.: U-net: Convolutional networks for biomedical image segmentation. In: International Conference on Medical Image Computing and Computer-Assisted Intervention. pp. 234–241. Springer (2015)

[5] Simonyan, K., Zisserman, A.: Very deep convolutional networks for large-scale image recognition. arXiv preprint arXiv:1409.1556 (2014)

[6] Volchenko N.N., Slavnova E.N., Gladunova Z.D. and others. Current cytological diagnostics of breast diseases. Moscow: Publishing house of Bauman Moscow State Technical University, 2014

Display Interfaces for the Control Unit of an Implantable Cardiac Pump

Ilya N. Rodionov[1], Igor V. Nesterenko, Dmitriy V. Telyshev, Ivan .A. Sapozhkov

Department of biomedical system
National Research University of Electronic Technology, Zelenograd Moscow, Russian Federations

Contact: rodionov@bms.zone

Introduction

A cardiac pump consists of the implanted module providing monitoring of a heart rate and the external block providing processing and visualization of the logged data. One of basic elements of the external block is the graphic display. Coming from the sizes of device and quantity of displayed information, LCD and OLED displays are used as an output information device.

Presently the digital interfaces of image transferring are used for the small-size displays. The bit depth of information transmission depends on the depth of color of the image that we want to give. In black and white displays each pixel has from one to eight digits. In color displays it has from eight (RGB332) to 24 (RGB888) bits [1]. Figure 1 shows the type structure of graphic display control.

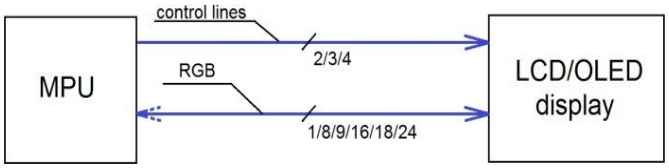

Figure 1: Typical connection of graphic displays

In the process of development restrictions and requirements, such as energy consumption, size, reliability, volume of the output information, cost etc., are imposed on a device. According to problem a developer make an optimal decision about the choice of hardware components. An interface, which will be used for data transmission, is chosen during work with graphic displays.

INTERFACES DESCRIPTION

A. Parallel interfaces

1. RGB interface:
Digital RGB interface has three timing signals - DOTCLK (PIXELCLK), HSYNC and VSYNC with frequencies of one pixel, line and frame transmission. Figure 2 shows the RGB transmission timing [2].

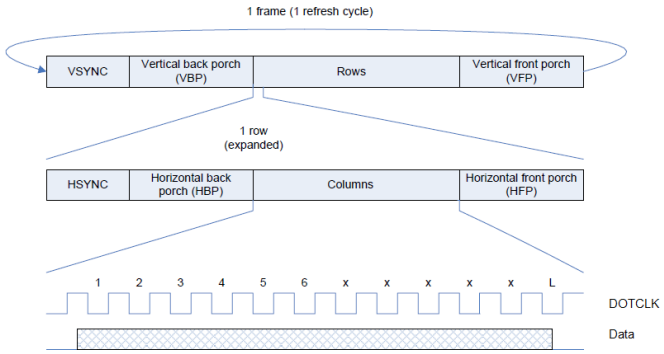

Figure 2: Frame and line timing parameters

To transmit a pixel color the parallel digital data bus is used. Width of bus is determined by colorize that we want to pass, or by restrictions of terminals. At the using of RGB interface, a width of data bus is 24 bits (RGB888). The feature of RGB interface work is transmission of full image frame. This method of image display is useful when it is necessary to change a picture on the screen constantly, for example, in the video transmission to screen.

2. System parallel interfaces.
For data transmission to a GPU it isn't always required to pass a full image. It is mostly necessary to change a small area of image on the screen. For this purpose Motorola and Intel companies created their own interfaces of graphic images transfer, which use registers of data transmission control in the RAM of GPU. The features of such interfaces are work with registers and delivery of control signal lines. The main difference between interfaces of Motorola and Intel companies is in the control signals. For the transmission of different color depth the different data bus width is used. We shall consider in detail every interface [3].

Intel 8080: Fig. 3 shows 8080-series bus interface [4]

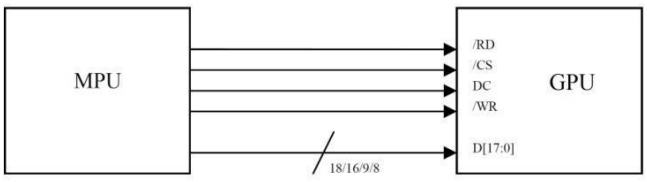

Figure 3: 8080-series Bus Interface

978-1-5386-4340-2/18/$31.00©2018 IEEE

The /WR and /RD signals are for indication writing to register and reading from register. The DC signal is used for designation of transmitted word type: command word (log.0) or data (log.1). The /CS signal is used for selecting chip of required device. There are timing performances of 8080 interface in the Table 1 [4]. Figure 4 shows the timing diagram of command/data writing [4].

Table 1: Parallel 8080, 6800 Timing Characteristics

Parameter	Min	Max	Unit
Clock Cycle Time (write cycle)	75	–	ns
Clock Cycle Time (read cycle)	450	–	ns
Pulse Width $\overline{CS}$ low (write cycle)	40	–	ns
Pulse Width $\overline{CS}$ high (write cycle)	25	–	ns
Data Access Time (READ)	250	–	ns
Output Hold time (READ)	100	–	ns
Pulse Width $\overline{CS}$ low (read cycle)	500	–	ns
Pulse Width $\overline{CS}$ high (read cycle)	500	–	ns
Rise time	–	4	ns
Fall time	–	4	ns

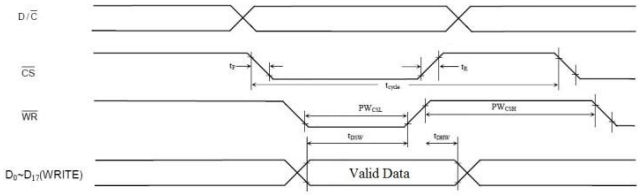

Figure 4: Parallel 8080-series Interface Timing Characteristics (write)

Motorola 6800: Fig. 5 shows 6800-series bus interface [1].

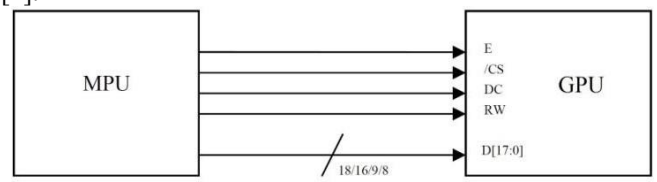

Figure 5: 6800-series Bus Interface

Unlike the Intel 8080 this interface is synchronous. For synchronization the E line, which latch data at the falling edge, is used. The RW control line is used for designation of read (log.1) or write (log.0) cycles. The DC signal is used for designation of transmitted word type: command word (log.0) or data (log.1). The /CS signal is used for selecting chip of required device. There are timing performances of Motorola 6800 interface in the Table 1 [4]. Figure 6 shows the timing diagram of command/data writing [4].

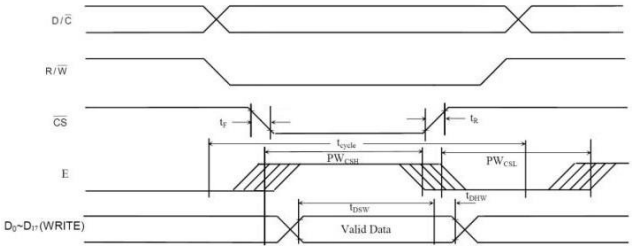

Figure 6: Parallel 6800-series Interface Timing Characteristics (write)

B. Serial system interface SPI

All considered interfaces had a parallel data bus. During resource lack the serial SPI interface is used for graphic data transmission. More often all this interface is used for black and white displays, which have a 1bpp capacity. There are 4-wire and 3-wire ways of data transmission by SPI.

4-wire SPI: Four flow lines are used for an information transfer. The SCLK signal is for data transmission clocking. The CS signal is used for selecting chip of required device. The SDI signal is used for data transmission. The SDC signal is used for designation of transmitted word type: command word (log.0) or data (log.1). In the process of one command word or data transmission 8 bits are used. There are timing performances of 4-wire SPI interface in the Table 2 [4]. Figure 7 shows the timing diagram of command/data writing [4].

Table 2: Serial Timing Characteristics

Parameter	Min	Max	Unit
Clock Cycle Time	75	–	ns
Chip Select Setup Time	2	–	ns
Chip Select Hold Time	10	–	ns
Clock Low Time	38	–	ns
Clock High Time	38	–	ns
Rise time	–	4	ns
Fall time	–	4	ns

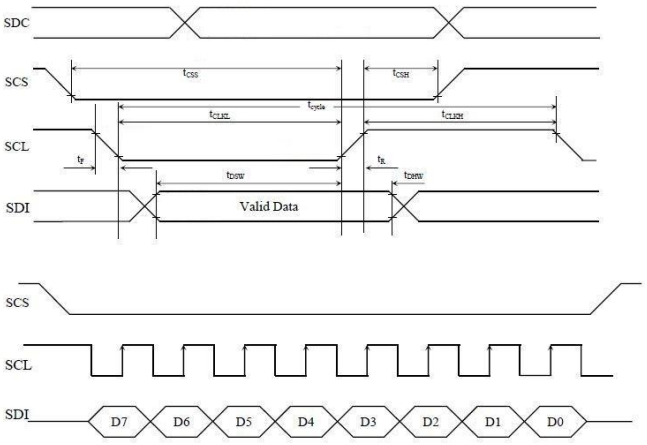

Figure 7: 4-wire Serial Timing Characteristics

978-1-5386-4340-2/18/$31.00©2018 IEEE

3-wire SPI: Three flow lines are used for an information transfer. The SCLK signal is for data transmission clocking. The CS signal is used for selecting chip of required device. The SDI signal is used for data transmission. In the process of one command word or data transmission, 9 bits are used, and also the first bit points to a transmitted word type (command word or data). Figure 8 shows the timing diagram of command/data writing [4].

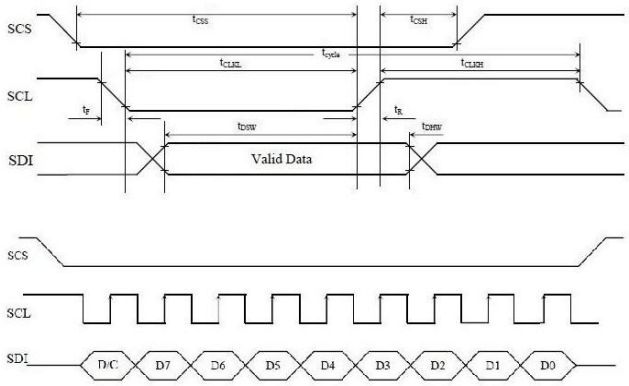

Figure 8: 3-wire Serial Timing Characteristics

Comparison of interfaces

Developing a device, it is necessary to understand, what interface will be optimal for this task. The basically criteria of interfaces comparison are memory, CPU time, number of wires and frame rate. There is comparing of interfaces in the Table 3.

Table 3: Comparison of interfaces

Interface / Criteria	RGB	Parallel 8/9 bpp	Parallel 16/18 bpp	SPI 4-wire
Memory	Bad	Good	Good	Good
CPU time	Good	Bad	Bad	Very bad
Number of wires	Bad	Middle	Bad	Good
Frame rate	Good	Good	Good	Bad

In considering each interface it is possible to select a few groups of the under development devices where its application will be optimal. The small-size devices with small output information scope are in the first group. Using of the internal MPU SPI unit is typical for such systems. The large-size devices with big output information scope are in the second group. Using of the parallel interface with the 16/18-bit data bus is the best variant for such systems. The small-size devices with big output information scope are in the third group. Using of the parallel interface with 8/9-bit data bus is typical for such systems. It should be taken that video controllers support transmission of bigger quantity of colors per pixel (16/18 bpp) in case of the 8/9- bit data bus. For this purpose we do two data sending instead of one, but we give up MPU time.

The classification given earlier is applicable to displays with internal video controller. In the absence of the internal GPU the RGB interface is used.

Conclusions

Comparing interfaces, we can note that everyone has advantages and disadvantages. When using parallel interfaces critical parameter is the MPU time. In the presence internal the MPU DMA unit we can transfer information to the display practically without using CPU time. The storage area which the DMA unit will transfer to a video controller is necessary for using this unit.

On the basis of the conducted research it has been decided to use for visualization of data of the Cardiac Pump the 8-bit Parallel Intel 8080 interface and color LCD with a 320x240 pixels screen resolution. Experiments were carried out and the MPU time was measured with and without using DMA. For display one-color rectangle at full screen size without using the DMA unit 15ms of MPU time and 1 byte of a memory were required. When using DMA ≈3us of MPU time and 75 Kbytes of a memory were required.

References

[1] LCD Module Protocol Interfaces at http://www.lxdinc.com/
[2] Introduction to graphics and LCD technologies at http://www.nxp.com/
[3] TFT LCD interfacing with the high-density STM32F10xxx FSMC at http://www.st.com//
[4] Solomon Systech Limited (2009) SSD2119 Advance Information. 320 RGB x 240 TFT LCD Driver. Integrated Power Circuit, Source and Gate Driver and RAM.

Acknowledgment

This work was provided by the Ministry of Education and Science of the Russian Federation (Agreement 14.575.21.0145, RFMEFI57517X0145 from September 26, 2017).

978-1-5386-4340-2/18/$31.00©2018 IEEE

A Closed-loop system for blood glucose level control

E.L. Litinskaia[1], K.V. Pozhar[1], N.A. Bazaev[1], P.A. Rudenko[1], V.M.Grinvald[1], A.I. Chekasin[1]

[1]National Research University of Electronic Technology (MIET),
Bld. 1, Shokin Square, Zelenograd, Moscow, Russian Federation

Contact: zheka101993@yandex.ru

Introduction

Diabetes mellitus type 1 is a metabolic disease characterized by chronic increase of blood glucose concentration (BG) that occurs when pancreas is no longer available to produce enough amount of insulin. Patients with diabetes mellitus need continuous control of BG.

One of the most widespread methods for type 1 diabetes compensation is pump insulin therapy based on the exogenous insulin infusion combined with special physical activity treatments.

Closed-loop system for BG control may improve efficiency of insulin therapy and, furthermore provides an opportunity to compensate diabetes mellitus automatically.

Almost all up-to-date commercial BG meters and monitoring systems are invasive. A portable noninvasive glucometer development is an important task for modern science.

In the paper, we present a closed-loop system for blood glucose level control on the basis of a noninvasive glucometer, an insulin pump and model predictive control.

Elements and applications

Closed-loop operation is in maintaining BG in physiological range and preventing hypo- and hyperglycemia. A continuous glucose monitor measures BG noninvasively. An analyzing system is based on model-predictive control.

An insulin pump (IP) provides precision subcutaneous insulin infusion and control of an actual infused dose. The IP experimental embodiment comprises of a control unit, a mechanical drive based on a micro motor with a reduction gear system 1:1024, and an infusion system with a 3 ml reservoir. Tab.1 presents main parameters of the developed pump.

The experimental embodiment of portable non-invasive glucometer (PNG) comprises of a control unit and an earlap clip, connected to each other by an opto-electrical cable. Noninvasive BG measurement is based on absorption spectroscopy method. Infrared radiation from a laser diode is transmitted through an earlap and is registered by a photodiode. Transmitted radiation is analyzed and BG is calculated. The algorithm for calculating the concentration is based on the iterative methods.

The clip consists of a housing, a transmitter, a receiver (InGaAs photodiode) and optical elements (lenses, mirrors, windows). Infrared radiation goes from the control unit to the earlap via the optical fiber. Tab.2 presents main parameters of the developed glucometer.

Table 1: Insulin Pump
Experimental Embodiment Parameters

Parameter	Value
Reservoir volume	3 ml (300 u)
Basal insulin discretization	0.025 u
Bolus insulin discretization	0.2 u (2 ml)
Amount of daily basal profiles	48
Infusion accuracy	±2,6%
Energy supply	1 AAA battery
Run time (continuous work time)	3 days
Connection	Bluetooth
Control	autonomous/ by smartphone
Indication	3.5″TFT resistive touch screen

Table 2: Glucometer Experimental
Embodiment Parameters

Parameter	Value
Measurement object	earlap
Laser power	30 mW
Time of a single measurement	5 min
Amount of measurements during monitoring	12 mes/h
Energy supply	2xICR18650
Run time (continuous work time)	> 6 h
Connection	Bluetooth
Control	by smartphone
Indication	LED

IP and PNG can be controlled by a smartphone connected to them via Bluetooth interface. Smartphone application allows user to:

– input data about food intake and calibration data;

– input of personal and physiological data affecting on BG dynamics;

– create of basal and bolus insulin patterns creation and launching;

– visualize current BG and its dynamics track;

– save and show statistics data of the patient by certain day, week or month;
– signalize on appearance of system messages, warnings or errors.

In order to organize an effective feedback between IP and PNG we propose a short-term prediction algorithm [1]. Tasks of the algorithm are the following:
– patient BG prediction;
– calculation of the required bolus insulin dose;
– infusion subsystem or glucometer faults alarms;
– detecting user incorrect information input;
– alarms for hypo- and hyperglycemia;
– correcting the mathematical model parameters;
– detecting wrong BG measure results;
– detecting the need of glucometer to be recalibrated.

The algorithm is based on mathematical model of BG dynamics [2, 3]. The model assumes that glucose dynamics is regulated by insulin, amylin, epinephrine and glucagon secretion. Ascents of BG are mainly caused by food intake as well as glycogenolysis and gluconeogenesis activated by glucagon and epinephrine. Descents of BG are caused by glycolisys and glycogenesis activated by insulin and amylin. Thus, the general equation of BG dynamics can be represented as follows:

$$G = G_0 + G_f(m_{carb}, \zeta) + G_{gls}(\nu_{gn}, \nu_{epn}) + \\ + G_{gng}(\nu_{gn}, \nu_{epn}) - G_{glg}(\nu_{ins}, \nu_{am}) - G_{gs}(\nu_{ins}, \nu_{am}) \quad (1)$$

where G is current BG, G_0 is initial BG, m_{carb} is meal carbohydrates mass, ζ is food glycemic index, ν_{gn}, ν_{epn}, ν_{ins}, ν_{am} are concentrations of glucagon, epinephrine, insulin and amylin.

The closed-loop system comprises of two data sets – the measured BG from PNG and the predicted BG. The difference between them determines its further operation.

When a patient enters meal/insulin data or bolus insulin data is received from the pump, the model and the prediction are recalculated. After the prediction is made, several intervals are calculated for the current prediction. These ranges are used to classify the measured value into one of the following categories: reliable, reasonable reliable and unreliable. They are taken into consideration for error determination if appeared.

Results

Experimental trials of the closed-loop system were performed using the special test bench [4]; the scheme of the one is presented in the Fig.1.The test bench allows adjusting necessary glucose concentration in a model solution circulating in a flowthrough cuvette. Glucose level increasing simulates food intake while decreasing simulates insulin infusion. Blood-model solution contained glucose, water and such blood plasma components as albumin, urea, creatinine etc. A controlled hydraulic system provides smooth and accurate setting of target concentration in the cuvette.

Current glucose concentration in the cuvette was measured by the developed noninvasive glucometer and HemoCue Glucose 201+ as a reference. For relative error estimation 20 experiments were performed (36 measurements/experiment with BG in range 75–400 mg/dl, step 5–10 mg/dl). An average error in hyperglycemia is 13,41 %, in normoglycemia is 17,85 %, in hypoglycemia is 24,89 %. Adequacy of glucose meters is acceptable to be estimated using Clarke Error Grid Analysis (EGA). EGA of developed noninvasive glucometer is represented on the Fig.2. On the X axis are reference measurements; on the Y axis are developed glucometer measurements.

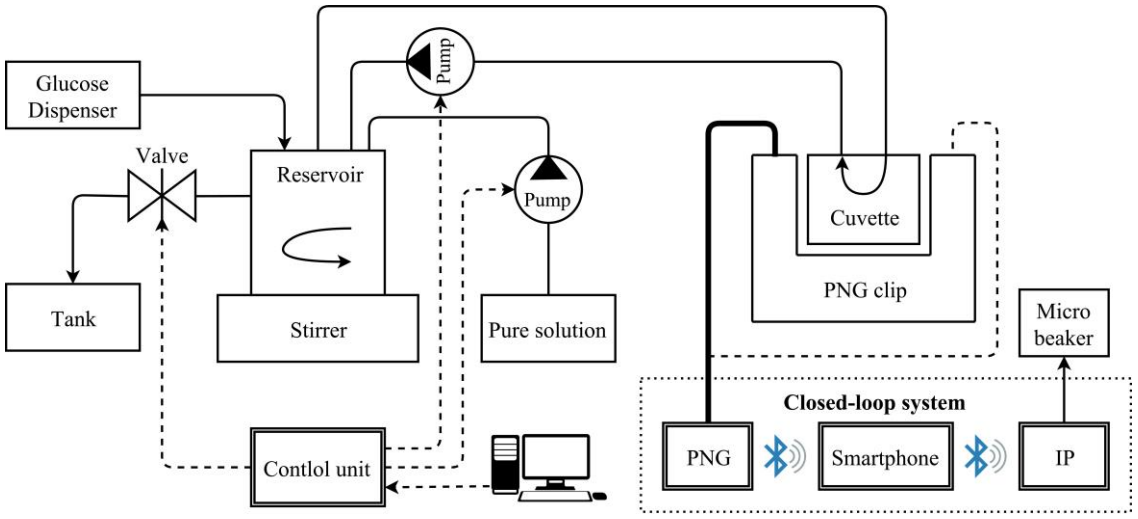

Figure 1: The scheme of the test bench for the closed-loop system experimental trails

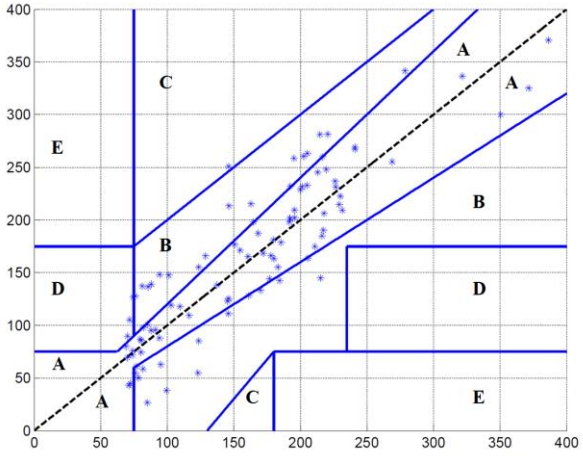

Figure 2: EGA of developed glucometer.
95.8% of measurements are in the A- and B-zone,
in C-zone is 1%, in D-zone – 3.1%, in E-zone – 0%

Series of experiments were performed in order to estimate the accuracy of the developed insulin pump. The amount of infusing insulin was changed from 0.1 ml to 2 ml, by 0.1 ml once an hour. Actually infused value was estimated by a micro beaker. As a result, the insulin infusion error averaged for one hour is 2.6%, while the maximum error is in the test range of 3.1%.

The short-term prediction algorithm was designed and tested *in silico* using Matlab. The input data sets for the algorithm were formed using the processed [5] DirecNet clinical protocols [6]. Two studies were performed: the accuracy study and the functional one. The functional study was aimed to test PNG and IP faults, incorrect data, hypo- and hyperglycemia alarms adequacy. During the study data from 30 patients was used. It included tracks for two consecutive days. For each patient, the day 1 track was used for mathematical model training and the day 2 track - for prediction system tests.

As measured BG in accuracy tests, we use actual patient track values with 5–25 % normal noise added. The algorithm was tested on every patient with different noise levels. Tests show that the difference between predicted values and patient BG values was less than 10%. During functional tests in every BG track, we deleted some data about food intake or insulin injections. As a result, the predicted track differed from real and measured ones. The algorithm analyzed the nature of the discrepancy of tracks and indicated relevant message. In every test the algorithm detected incorrect/absent data or displayed the necessary timely warnings.

The example of the prediction algorithm operation is presented in the Fig. 3.

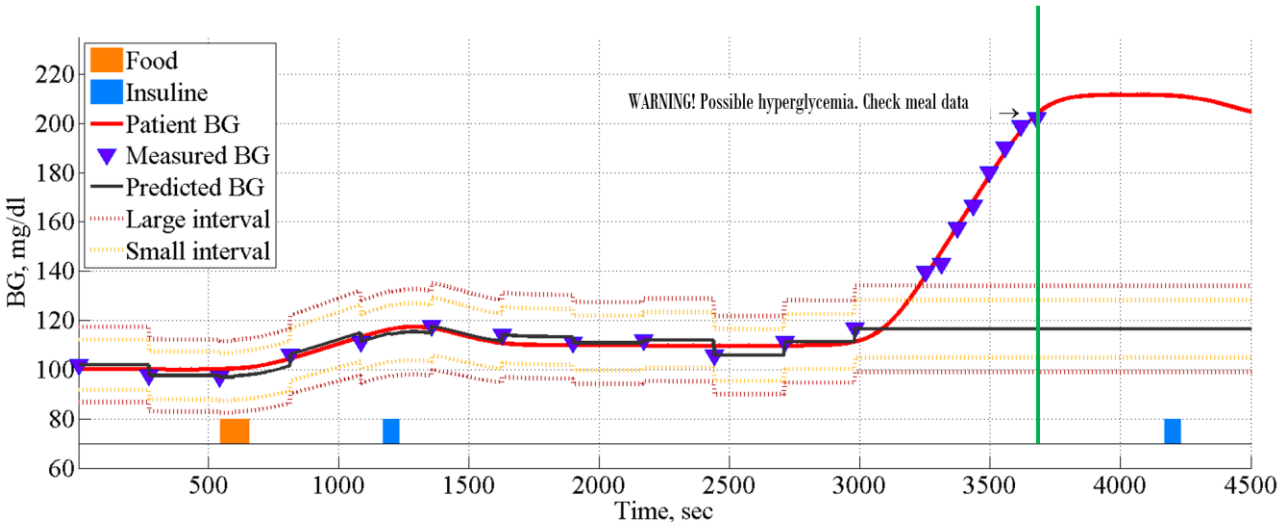

Figure 3: Prediction testing example. Patient BG is unknown for algorithm.
Predicted track is shifted to measured point if the latter is inside the reliable interval (small interval), measurement frequency 1 in 300s. If measured values are aside the reliable zone measurement frequency increased (1 in 60s).
If a divergent trend is detected, the algorithm cautions user.

Conclusions

The closed-loop system for BG level control is aimed to automate BG maintaining in physiological range with patient minimal involvement. The key feature of the system is a model predictive control and noninvasive BG measurements. The developed closed-loop elements (the optical noninvasive glucometer, the insulin pump and the model-based prediction algorithm) tests show high efficiency of proposed methods. The prediction algorithm detects incorrect data, faults of the glucometer and the pump. The implemented model predictive control allows reduction of measurement errors.

References

[1] Bazaev N.A., Pozhar K.V. Blood Glucose Prediction for "Artificial Pancreas" System. Gluconeogenesis. Rijeka, Croatia: InTech, 55–73, 2017.

[2] N. Bazaev, K. Pozhar, E. Litinskaya, P. Rudenko. Mathematic Model of Blood Glucose Dynamics. The International Journal of Artificial Organs, 40(8), 437, 2017.
[3] N.A. Bazaev, K.V. Pozhar, P.A. Rudenko. Mathematical Modeling of Blood Glucose Concentration Dynamics. Biomedical Engineering, 48(6), 292–296, 2015.
[4] N.A. Bazaev, V.M. Grinvald, A.N. Zhigailo, E.L. Litinskaya, K.V. Pozhar, P.A. Rudenko. A Test bench for performance validation of an artificial pancreas system. Biomedical Engineering, Vol. 51, No. 6, March, 2018, pp. 422–426.
[5] P.A. Rudenko, N.A. Bazaev, K.V. Pozhar, E.L. Litinskaia, V.M. Grinvald, A.I. Chekasin. Getting day blood glucose tracks using clinical protocols of the DirecNet database. Biomedical Engineering, Vol. 51, No. 5, January, 2018, pp. 346–349.
[6] Ruedy K.J., Beck R.W., Xing D. and Kollman C. For the Diabetes Research in Children Network (DirecNet) Study Group Diabetes Research in Children Network: Availability of Protocol Data Sets // J Diabetes Sci Technol. – 2007. – Vol. 1(5). – pp. 738-745.

Acknowledgements

The work was financed by the Ministry of Education and Science of Russian Federation: agreement № 14.578.21.0186, project ID: RFMEFI57816X0186.

Effect of thrombus formation on heat emission in Sputnik RBP

A.O. Porfiryev[1], D.V. Telyshev[1], A.A. Pugovkin[1], S.V. Selishchev[1]

[1]National Research University of Electronic Technology, Shokin Square 1, Zelenograd, Moscow, Russian Federation

Contact: porfiryev@bms.zone

Introduction

End-stage heart failure (HF) is a major cause of mortality, morbidity and disability worldwide. Nowadays, a surgical and medical treatment of HF has a positive trend. But heart transplantation remains an optimal treatment of end-stage HF. A shortage of donor organs has made this therapy available only for limited number of patients (1). This problem required a development of ventricular assist devices (VADs) for critically ilium patients. The first devices had large dimension, but by the aid of engineering and technology developers have the opportunity to reduce the dimensions of VADs (2, 3). This feature allows the use of VADs for treatment of patients with small body surface area. However, the miniaturization of pump components may lead to a high hemolysis level (4, 5). Thrombus formation remains a serious problem of axial and centrifugal ventricular assist devices (6-8).

A typical construction of axial VAD consists of a flow straightener, an inlet bearing, an impeller, an outlet bearing and a diffuser in series, and a stator (9, 10). Mechanical friction between the pump components in such devices is accompanied by heat generation, which depends on the pump design (11).

Conversion of electrical energy to thermal energy is inherent for any motor under normal operation mode (12). Heat dissipation occurs due to thermal emissions from pump housing and heat transmission of blood moving through a device. Herewith excessive heat generation can adversely affect the blood hemolysis level and the protein denaturation increasing the probability of thrombus formation (13). As a result the pump failure probability increases. This problem can be solved only by emergency surgery with full replacement of implanted VAD (14, 15). Currently, the influence of thrombosis on a rotary blood pump heat generation is not fully investigated. Therefore, in vitro tests were conducted in hydraulic closed loop using the rotary blood pump of the Sputnik VAD to determine the nature of heat generation for different conditions which are typical for implantable systems. Since 2012 the Sputnik VAD successfully used to replace of left ventricular function for patients with HF. This VAD is the axial and continuous flow pump.

Materials and Methods

The Sputnik VAD construction is comprised of movable element (impeller) and stationary elements (flow straightener, diffuser, inlet and outlet bearings). An electrical motor allows you to rotate the pump at a speed from 5000 to 10000 rpm, providing a flow of up to 10 L/min (16). Sputnik VAD produces necessary head pressure-flow rate (H-Q) curves (17). This blood pump has a length of 82 mm, outside full diameter of 34 mm and weight of 246 g.

Experiments to compare the influence of thrombus formation on the VAD heat generation was carried out under following conditions: non-thrombosis, inlet (flow straightener) thrombosis, outlet (diffuser) thrombosis. The platinum-based silicone Ecoflex 00-10 (Smooth-On, USA) was used as a material for simulation of thrombus formation. For thrombus formation manufacture silicone components A and B was mixing in equal amounts. Degasing of resulting compound was conducted in vacuum chamber during 10 minutes. Further the silicone was applied on inner surface of flow straightener and diffuser. By hot air gun at 200 °C silicone instantly fixed. After complete polymerization the Ecoflex silicone is a very soft, durable and stretchable material without tacky surface. Thrombus with a volume of 0.5 cc was used in tests. Figure 1 shows an artificial clot in the diffuser (A, B) and flow straightener (C, D) before and after the tests. In total 27 hours of tests were performed for each thrombus formation.

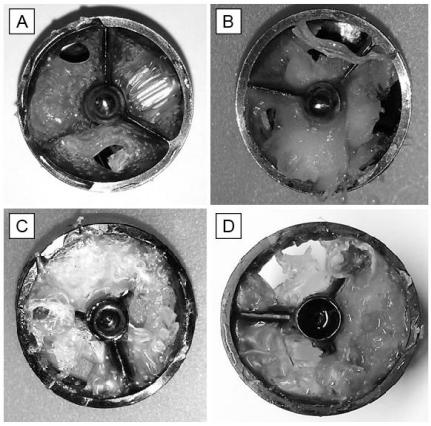

Figure 1: Image of the diffuser (A, B) and flow straightener (C, D) thrombosis at the beginning (A, C) and at the end of all tests (B, D).

The experiments were conducted on a special test bench, which consists of a hydraulic loop, temperature measuring and recording devices (infrared camera and thermocouple unit) and control units including pump controller, power source and personal computer. The pump body during the tests was placed inside a viscoelastic silicone cover with a volume of 1400 cc, which properties are similar to the soft tissues properties (18). Pump location inside the cover limits the heat dissipation into environment during the tests.

Temperature change of the Sputnik VAD body surface was measured by thermocouple-thermometer TPI 343 (TPI, USA). The data was recorded every 2 minutes. Temperature sensors were fixed tightly for more accurate recording of the pump surface temperature: one sensor – on the pump body at the stator location, and another sensor – at the pump outlet. This location of sensors allowed recording the heat emission level during stator operation and the temperature change at the pump outlet.

As an additional device for temperature change measurement a thermal imaging camera THT-47 (HT Italia, Italy) was used. This infrared camera is designed for rapid detection of heat map emitted by the test unit. THT Link software was used to analyze the obtained data.

Different test fluids were used to analyze viscosity influence on the pump heating. On the initial test stage distilled water with dynamic viscosity of 0.00085 Pa·s at 23 °C was taken. Aqueous glycerol solution (dynamic viscosity of 0.003 Pa·s at 23 °C) was used as fluid with blood viscosity. The test fluid volume in hydraulic loop was 6150 cc. On the second test stage test fluid was heated up to 37 °C during 90 minutes in a special bath by a heat regulator. Constant bath temperature was maintained for the duration of the experiment. Aqueous glycerol solution with dynamic viscosity of 0.006 Pa·s at 23 °C was used. It is noted that viscosity of fluid being heated decreases. Thus, aqueous glycerol solution with dynamic viscosity of 0.006 Pa·s at 23 °C after heating to 37 °C has viscosity equal to blood viscosity (19).

The experiments by test bench were carried out for each system configuration separately. Differences consist in four parameters: the pump speed (5000, 7000 and 9000 rpm), the viscosity of test fluid (distilled water or aqueous glycerol solution), the presence or absence thrombosis and its location and the test fluid temperature (room temperature – 23 °C or body temperature – 37°C). When using the aqueous glycerol solution with dynamic viscosity of 0.003 Pa·s at 23 °C, diffuser thrombosis and test fluid heating to body temperature the system configuration is «blood viscosity, outlet thrombosis, 37 °C».

Results

Experiments without heating the test fluid

The thermal map of the Sputnik VAD surface was obtained by infrared camera with aqueous glycerol solution with dynamic viscosity of 0.003 Pa·s as test fluid, pump reference speed of 5000 rpm and non-thrombosis (Fig. 2A). Figure shows areas with high temperature corresponding to the stator area. Also the output bearing was slightly heated in compare to the input bearing. There was no zone of excessive heat generation at the flow straightener area. Heat map of the pump surface is shown in Figure 2B for the pump inlet thrombosis case. The maximum temperature of the pump surface was located in the area between the inlet bearing and stator and amounted to 25.8 °C. In this case the heat emission level at the pump inlet is higher compared to the pump outlet. This pattern is caused by thrombus location on the flow straightener. It should be noted the difference of the pump surface heat map in absence and presence of thrombus formation: hot spots in Figure 2A are shifted to the left (the pump inlet), whereas hot spots in Figure 2B are located at the pump center. Heat map obtained in the experiments with diffuser thrombosis is shown in Figure 2C. The minimum temperature of the pump surface was 24.1 °C, maximum temperature was achieved at the diffuser area and equal to 29.1 °C. In addition, there is a driveline cable connection in this pump body area, which emits a small amount of heat during pump operation.

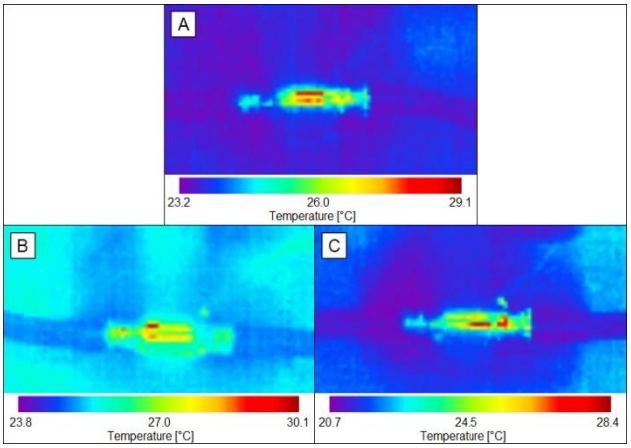

Figure 2: Thermal map of the Sputnik VAD surface at speed of 5000 rpm, using test fluid with blood viscosity and different thrombus clamping; where A – non-thrombosis, B – inlet thrombosis, C – outlet thrombosis.

For the same system configuration a temperature increase at the stator area surface and at the pump outlet measured using thermocouple sensors was equal to 0.7 °C for non-thrombosis, 1.2 °C for the inlet thrombosis and 1 °C for the outlet thrombosis. Consequently, for 5000 rpm the influence of the stator thermal energy to the total pump heat generation is minimized. Temperature change curves increase gradually, without spikes during 50 minutes, and then curves change to linearity range with a constant temperature value.

The temperature distribution obtained along the pump axis for reference speed of 9000 rpm is shown in Figure 3. For clarity the location of main pump components relative to coordinate origin is shown by vertical lines and numbers. Nature of the distribution is similar to the same data at the pump speed of 5000 and 7000 rpm. The differences are in maximum and average temperature values. For non-thrombosis case measured maximum temperature value of 26.7 °C is in the stator area. Conversion of stator electrical energy to thermal energy had a major influence on the total heat map of the pump. For inlet thrombosis case maximum temperature value was located in the area between the inlet bearing and stator, moreover characteristic temperature rise is observed before the thrombus, which is accompanied by a further sharp drop of meas-

ured temperature value. For outlet thrombosis case maximum temperature value of 27.9 °C was located in the thrombosis area. The temperature average at 9000 rpm for non-thrombosis system configuration was 24.4 °C, for inlet thrombosis – 24.6 °C and for outlet thrombosis – 24.5 °C.

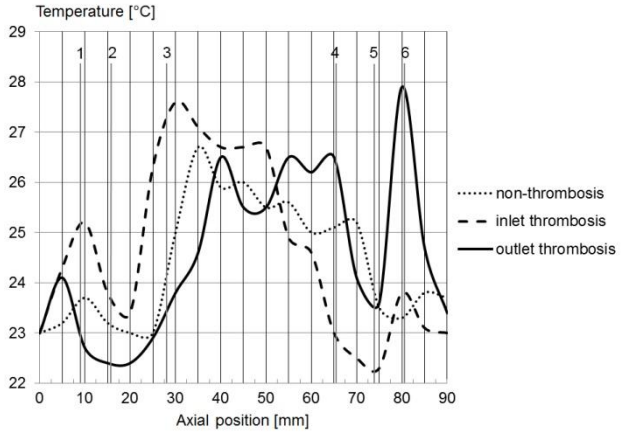

Figure 3: Temperature distribution along the pump axis for 9000 rpm, using test fluid with blood viscosity and different thrombus clamping; where 1-2 – flow straightener zone, 2-5 – impeller zone, 3-4 – motor zone, 5-6 – diffuser zone.

Curves obtained by thermocouple at 9000 rpm have different shape: temperature change curves of the stator area at the test start are compact and linearly increases with time, but the outlet temperature curves have a sharp discontinuity of temperature at the test start. At the reference pump speed of 9000 rpm maximum outlet temperature was higher than the stator temperature. Therefore, test fluid temperature was higher than the stator area surface temperature. As a result, electric stator energy is converted to thermal energy and contributes to heating of the test fluid.

Experiments with heating the test fluid

To determine the pump heat generation nature at human body temperature the test fluid was heated to 37 °C. After changing a single parameter of system configuration each subsequent experiment was started only after test fluid and pump body cooling to room temperature followed by heating to 37 °C. The pump outlet temperature change obtained by thermocouple is shown in Figure 4. The minimal temperature increase was 1.6 °C for «distilled water, outlet thrombosis, room temperature» configuration, maximum temperature increase was 5.1 °C for «blood viscosity, non-thrombosis, room temperature» configuration. Temperature increase is typical for all curves in the first 40-50 minutes of testing, further growth was slowing down and curves moved to flat area with a constant temperature spans.

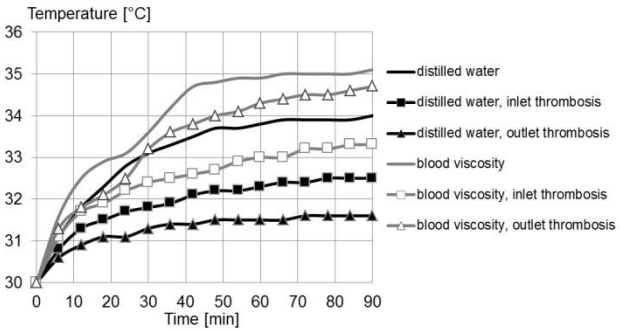

Figure 4: Temperature change curves at the pump outlet for different system configuration at the pump speed of 7000 rpm.

Temperature distribution curves for various reference speeds and thrombus presence at the inlet part of the pump are shown in Figure 5. The curves have a similar structure: temperature decreases first and then increases, reaching a maximum value in zone 1-2; in the stator area there is a decline up to diffuser reaching a minimum value; in zones 5-6 curves sharply increase and converge on the same parallel at 80 mm point; outlet temperature falls again. By reference to previously results it can be inferred that zone with maximum temperature includes a thrombus formation.

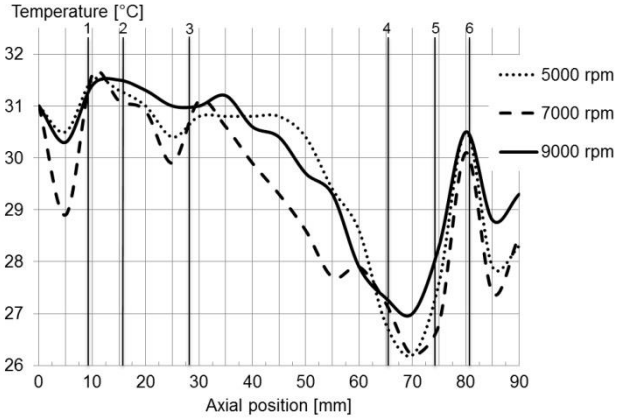

Figure 5: Temperature distribution along the pump axis for inlet thrombosis, using test fluid with blood viscosity and at different pump speeds; where 1-2 – flow straightener zone, 2-5 – impeller zone, 3-4 – motor zone, 5-6 – diffuser zone.

Conclusion and discussion

To determine relationship between the Sputnik VAD thrombosis and the pump heat generation numerous and continuous tests were conducted at in vitro bench. Temperature of the pump surface was increased in all trials regardless of reference pump speed, test fluid viscosity or thrombosis presence. At 5000 rpm conversion of stator electric energy to thermal energy provides the main contribution to the total pump heat emission. Whereas at

7000 and 9000 rpm pump surface temperature value depends more on pump rotational speed and test fluid viscosity. Results obtained at room temperature with great probability allow determining the presence and location of thrombosis. Pump surface areas with high temperature corresponded to thrombus presence in this pump part.

When the test fluid is heated up to human body temperature, identification of thrombus formation by visual analysis of heat map is complicated. This problem is associated with excessive test fluid heating and, therefore, elastic tubes surface heating. Temperature distribution curves along the pump axis were constructed to solve this task. Sites of pump, in which maximum temperature was measured, corresponds to thrombosis areas.

Data obtained on the laboratory bench gives an insight into the nature of released pump heat. However, a living organism is a very complex structure with many nuances. Therefore, understanding of human body heat transfer will allow developing a precise experimental model that will make possible obtaining accurate data of interaction with VAD. Most likely the overall blood temperature of the human organism does not increase during the VAD operation. But short-term or localized heat emission inside the pump with blood moving through it may cause thrombosis. In this case temperature value is the most important parameter. There is an increase of hemolysis rate consequently resulting to thrombus formation and potential death of patient already at the temperature of 40 °C (20). In spite of numerous studies on pump thrombosis detection (21), main causes and possible solutions (21), this problem remains important in the development of ventricular assist devices. Furthermore, study of the thrombosis problem is extremely important in implantation of tissue engineering structures based on carbon nanotubes in the area of defects in heart tissues and blood vessels.

Understanding of the pump heat generation will allow improving the design of axial and centrifugal VADs and reducing the probability of thrombosis.

References

[1] Y. Ohashi, A. Andrade and Y. Nose. Hemolysis in an electromechanical driven pulsatile total artificial heart. Artif Organs,27(12):1089-1093, 2003.

[2] A. Cheung, K. Chorpenning and et al. Design concepts and preclinical results of a miniaturized HeartWare platform: The MVAD System. Innovations (Phila), 10(3):151-6, 2015.

[3] I. Adachi, S. Burki, F. Zafar and D.L. Morales. Pediatric ventricular assist devices. J Thorac Dis, 7(12): 2194–2202, 2015.

[4] J. Garbade, H.B. Bittner, S. Lehmann, F.W. Mohr and M.J. Barten. Miniaturization of left ventricular assist devices: the ongoing trend. Expert Rev Med Devices, 9(1):49-58, 2012.

[5] T. Takano, S. Schulte-Eistrup and et al. Impeller inner diameter in a miniaturized centrifugal blood pump. Artif Organs, 26(1):67-71, 2002.

[6] V. Tchantchaleishvili, F. Sagebin, R.E. Ross, W. Hallinan, K.Q. Schwarz and H.T. Massey. Evaluation and treatment of pump thrombosis and hemolysis. Ann Cardiothorac Surg, 3(5):490-495, 2014.

[7] D.J. Goldstein, R. John and et al. Algorithm for the diagnosis and management of suspected pump thrombus. J Heart Lung Transplant, 32(7):667-70, 2013.

[8] J.K. Kirklin, D.C. Naftel and et al. Pump thrombosis in the Thoratec HeartMate II device: an update analysis of the INTERMACS Registry. J Heart Lung Transplant, 34:1515-26, 2015.

[9] F.H. Sheikh and S.D. Russell. HeartMate II continuous-flow left ventricular assist system. Expert Rev Med Devices, 8(1):11-21, 2011.

[10] M.P. Macris, S.M. Parnis, O.H. Frazier, J.M. Fuqua Jr and R.K. Jarvik. Development of an implantable ventricular assist system. Ann Thorac Surg, 63(2):367-70, 1997.

[11] T. Kink and H. Reul. Concept for a new hydrodynamic blood bearing for miniature blood pumps. Artif Organs, 28(10):916-20, 2004.

[12] L. Chen, Y. Pei, F. Chai and S. Cheng. Investigation of a novel mechanical to thermal energy converter based on the inverse problem of electric machines. Energies, 9(7):1-19, 2016.

[13] K. Araki, Y. Taenaka and et al. Hemolysis and heat generation in six different types of centrifugal blood pumps. Artif Organs, 19(9):928-32, 1995.

[14] J.K. Kirklin, D.C. Naftel and R.L. Kormos. The fourth INTERMACS annual report: 4,000 implants and counting. J Heart Lung Transplant, 31:117–126, 2012.

[15] M.S. Slaughter, J.G. Rogers and et al. HeartMate II Investigators: Advanced heart failure treated with continuous-flow left ventricular assist device. N Engl J Med, 361:2241-2251, 2009.

[16] S.V. Selishchev and D.V. Telyshev. Ventricular Assist Device Sputnik: Description, technical features and characteristics. Trends Biomater Artif Organs, 29(3):207-210, 2015.

[17] S.V. Selishchev and D.V. Telyshev. Optimisation of the Sputnik-VAD design. Int J Artif Organs, 39(8):407-414, 2016.

[18] T.K. Yasar, T.J. Royston and R.L. Magin. Wideband MR elastography for viscoelasticity model identification. Magn Reson Med, 70(2): 479-489, 2013.

[19] J.B. Segur and H.E. Oberstar. Viscosity of glycerol and its aqueous solutions. Ind Eng Chem, 43(9):2117-2120, 1951.

[20] N.L. Gershfeld and M. Murayama. Thermal instability of red blood cell membrane bilayers: temperature dependence of hemolysis. J Membr Biol, 101:67–72, 1988.

[21] F. Kaufmann and T. Krabatsch. Using medical imaging for the detection of adverse events ("incidents") during the utilization of left ventricular assist devices in adult patients with advanced heart failure. Expert Rev Med Devices, 13(5):463-74, 2016.

[22] A. Blitz. Pump thrombosis - a riddle wrapped in a mystery inside an enigma. Ann Cardiothorac Surg, 3(5):450-471, 2014.

Acknowledgements

This work is sponsored by the Ministry of Education and Science of the Russian Federation (Agreement 14.578.21.0234 RFMEFI57817X0234).

Surgery in the year 2030: Surgery 4.0?

H. Feussner, D. Wilhelm

Department of Surgery, Klinikum rechts der Isar, Technical University Munich, Germany

Contact: hubertus.feussner@tum.de

Introduction

Future developments in surgery are not only interesting for surgeons but also an issue for biomedical engineers and computer scientists in order to focus their own work and energy to areas which most probably become relevant. Surgery of the next decade may be described best by the keyword "surgery 4.0".

The term and its meaning are as yet even unfamiliar to most surgeons and most probably even less known by engineers. We coined it in 2016 [Feußner 2016] to describe a vital development in surgery, which could conceivably become as disruptive in interventional medicine as the current trend toward economic and industrial digitalization. To make the parallels and contrasts more evident, a reflection on the Fourth Industrial Revolution is helpful.

The global economy is assumed to move forward to the Fourth Industrial Revolution. Commonly, the mechanization of production using water and steam power is considered to have driven the First Industrial Revolution. The next "revolutionary" impact on industrial productivity came from mass production facilitated by the availability of electrical energy and improved workflow organization (assembly line, etc.). This was followed by the Third Industrial Revolution, which is characterized by the use of information technology (IT) and robots to automate production.

Today, a systematic transformation of industrial production is under way, which can be grossly defined as the comprehensive computerization of manufacturing.

The vision is some type of self-organizing or autonomous production: the factory with its production lines "understands" what has to be produced and autonomously carries out all necessary steps and adjustments. This strategy, originally propagated by the German Government as the Industry 4.0 initiative, is evidenced in the customization of products under the condition of highly flexibilized production. This highly automated technology is enabled by the introduction of methods of self-optimization, self-configuration, self-diagnosis, cognition and intelligent support of the few human beings who are still required to master this complex process. The main pillars are as follows:

1. Interoperability: The ability of machines, devices, sensors, and people to connect and communicate with each other via the Internet of Things (IoT) or the Internet of People (IoP).
2. Information transparency: The ability of information systems to create a virtual copy of a physical world by digital models with sensor data. The very dense net of information is available for all stakeholders. A huge amount of raw data have to be collected and interpreted in a higher context.
3. Technical assistance: Decision-making has to be facilitated by preparing all necessary information. Humans have to decide all necessary preconditions (information) that have already been provided.
4. Decentralized decisions: The ability of lower-level systems to make decisions on their own and to perform their tasks as autonomously as possible. Only in the case of exceptions and/or conflicting goals are tasks to be escalated to a higher level.

Autonomous decision-making by mechatronic support devices is the real disruptive element of Industry 4.0. Humans will need to be confident that machines are able to act and react reasonably, reliably, and as fast and as safely as a human worker.

There are, however, some necessary preconditions for this vision to become reality.

1. The IoT must support direct communication or dialogue with the technical equipment. If one device alters its functionality, the whole technical environment is informed.
2. Data/information must be provided wherever it is needed in real-time and by a high-quality, reliable service (5G telecommunication).

Surgery and the 4.0 development

What then has all this to do with surgery? Some context in the form of a brief review of modern surgical history may be helpful.

The beginning of scientific surgery dates back about 150 years. Retrospectively, this comparatively short period of time can be subdivided into three different eras. In the beginning, surgeons learned to master the specific challenges of the different anatomical regions – beginning with the abdomen and ending with the brain. In the next phase, surgery was not any longer confined to resection/amputation, but the focus was now laid on substituting deficits. Destroyed joints were replaced by artificial implants, and functional reservoirs were developed to accommodate for the roles of the stomach or rectum, for example, after their resection. The ultimate highlight of the era was the transplantation of whole organs (the heart, liver, kidneys, etc.).

The trend today is to further minimize the surgical trauma – collateral damage to other organs, functional impairment, and pain due to the operative intervention. This third era of

surgery started with the introduction of laparoscopic surgery. Laparoscopy was, however, only the beginning of a broad development in many medical disciplines toward minimally invasive therapy.

We are now arguably on the threshold of a new era. This does not mean that further advances in reconstruction (phase II) or trauma reduction (phase III) should no longer be pursued, but the innovative impact comes now from another discipline: information/digitalization.

Although surgery is often considered a manual or technical discipline, it will not remain unaffected by the general trend toward the information age development.

On the contrary, surgery in the information age is more or less a synonym of "surgery 4.0". Surgery will soon adapt new technologies and methodologies, such as the IoT, process modeling, cooperative learning machines, and new approaches to the generation of knowledge that will affect surgery – all with the aim to improve the quality, efficiency, and outcomes of surgical care. Surgery 4.0 might be the chance to master the difficult situation surgery is currently in.

Surgery is forced to maximize quality and value of surgical in a highly competitive environment. Surgery 4.0 or "information-based surgery" might be the best chance to respond to these needs. Some practical aspects of "surgery 4.0" are delineated.

The fully integrated, "cognitive" OR workplace

Today, the surgical OR is a workplace comprehending the OR table, the surgical lamps and a plethora or peripheral devices working completely independent of each other. The OR of the future will be a highly integrated environment of smart intraoperative assistance systems collaborating with each other via the IoT.

Model-based surgery

A fully integrated OR, however, is only conceivable if the surgical activities – the workflow – is known and can be "understood" by the system. The precondition is a modelling of the surgical workflow.

A "surgical model" is an evidence-based, detailed plan of a particular surgical intervention with a clear description of the workflow from skin incision to closure. It not only includes the normal course of an operation but considers potential modifications and deviations as well. To create "surgical models" either bottom-up or top-down approaches may be considered [Neumuth 2017]. Modern IT methodologies such as machine learning will become extremely helpful to establish "model-based surgery". However, even the most advanced computer technology cannot substitute for surgical expertise – an urgent challenge for the surgical community to engage and scientifically collaborate in the development of Surgery 4.0.

Knowledge extraction

Since the preoperative diagnostic workup and the whole treatment as well as the postoperative care will be meticously documented in each individual case, these easily accessible data will become very valuable for gaining new insights retro- or prospectively (data mining). For surgical decision making, hundreds or thousands of similar cases can easily be identified as a fundament of evidence-based treatment.

The key: Surgical Data Science

As shown above, the future transformation in surgical care will be driven by data/information. The key elements on the path toward evidence-based surgery are new tools to measure, model, and quantify surgical processes including intraoperative decision-making and knowledge extraction. An intelligent collaboration between care providers and devices/technologies will be enabled. A new scientific domain is, thus, gradually emerging: Surgical Data Science. It is defined as follows: "Surgical Data Science is an emerging scientific field with the objective of improving the quality of interventional healthcare and its value through capturing, organization, analysis, and modeling of data. It encompasses all clinical disciplines in which patient care requires intervention to manipulate anatomical structures with a diagnostic, prognostic, or therapeutic goal, such as surgery, interventional radiology, radiotherapy, and interventional gastroenterology. Data may pertain to any part of the patient care process (from initial presentation to long-term outcomes), may concern the patient, caregivers, and/or technology used to deliver care, and is analyzed in the context of generic domain-specific knowledge derived from existing evidence, clinical guidelines, current practice patterns, caregiver experience, and patient preferences. Data may be obtained through medical records, imaging, medical devices or sensors that may either be positioned on patients or caregivers or integrated into the instruments and technology used to deliver care. Improvement may result from understanding processes and strategies, predicting events and clinical outcome, assisting physicians in decision-making and planning execution, optimizing ergonomics of systems, controlling devices before, during and after treatment as well as from advances in prevention, training, simulation and assessment. Surgical Data Science builds on principles and methods from other data-intensive disciplines such as computer science, engineering, information theory, statistics, mathematics, and epidemiology, and complements other information-enabled technologies such as surgical robotics, smart operating rooms, and electronic patient records." [Maier-Hein 2017] It also includes a significant impact on surgical education and training. Surgical Data Science (SDS) not only enables objective computer-aided skill evaluation but also automated coaching.

Discussion

Surgery of the next decades will certainly gain a new profile due to the vast use of information. Self-evidently surgery 4.0 is not only confined to a more or less abstract utilization of information but will also have a massive impact

upon the use of a new hardware: Intelligent, cognitive surgical assistance systems ("robots") will reduce the surgical workload by (semi-) autonomous manipulations like camera navigation or suturing. Integrated, precisely navigated percutaneous or endoscopic puncture probes could replace conventional surgical cancer resection by local ablation. Based upon an "intelligent" OR environment even completely new surgical approaches like combined laparoscopic/endovascular interventions are becoming conceivable. From the surgical viewpoint, these options would be highly attractive, but this also means that technology will play an increasing role in modern surgery. Simply accepting this fact is not enough what surgeons can do. They are even summoned up to contribute actively to technical progress by identifying currently existing deficits, by careful evaluation and improvement of prototypes and generally by providing their domain knowledge. Hopefully, this will lead to a new "culture of cooperation" between basic scientists, computer scientists, engineers and clinically active surgeons.

Conclusions

Surgery 4.0 does not mean that robots will perform surgery on their own in the future. This can neither be the vision of surgeons nor would it be accepted by the majority of patients in societies with a highly developed healthcare system, as one very recent study [Arnold 2017] has shown. However, artificial intelligence, robotics, model-based surgery, and many additional principles of Surgery 4.0 will certainly help to make surgery more evidence-based, safer, and easier, all with the goal of a better outcome and experience for the patient.

References

[1] Arnold D, Wilson T. What doctor? Why AI and robotics will define new health. 2017. Available at: https://www.pwc.de/de/gesundheitswesen-und-pharma/assets/30597_healthcare_aI_ipad_interactive_v10.pdf. Accessed 16 August 2017.

[2] Feußner H, Wilhelm D. Minimally invasive surgery and robotic surgery: surgery 4.0? Chirurg 2016;87:189–94.

[3] Maier-Hein L, Vedula S, Speidel S, Navab N, Kikinis R, Park A, Eisenmann M, Feussner H, Forestier G, Giannarou S, Hashizume M, Katic D, Kenngott H, Kranzfelder M, Malpani A, März K, Neumuth T, Padoy N, Pugh C, Schoch N, Stoyanov D, Taylor R, Wagner M, Hager GD, Jannin P. Surgical Data Science: Enabling next-generation surgery. arXiv:1701.06482, 2017

[4] Neumuth T. Surgical process modeling. Innov Surg Sci 2017;2:123–37.

Acknowledgements

Parts of this work were supported by the German Research Foundation (Deutsche Forschungsgemeinschaft DFG).

Intraoral Microfocus X-ray radiography in veterinary medicine

N.N. Potrakhov[1], Y.N. Potrakhov[1]

[1]Saint Petersburg Electrotechnical University "LETI", Russian Federation

Contact: yn@eltech-med.com

Introduction

The provision of veterinary dental care is becoming an increasingly urgent task, for example, in dog breeding. So, for a thoroughbred exhibition animal, the loss of even one tooth can lead to the termination of a career.

In medicine in the vast majority of cases, diagnosis of the maxillofacial department is carried out with the help of specialized X-ray devices: traditional dental units, orthopantomographs and cone-ray tomographs [1]. Traditional dental devices (radioviographs) are designed to produce images of individual teeth or jaw areas, orthopantomographs for two-dimensional, and cone-ray tomographs for three-dimensional images of the full dentition of both jaws, including adjacent anatomical structures.

For a number of reasons - differences in the anatomy and physiology of the maxillofacial department of man and dog, as well as the language barrier, these devices cannot be directly used in veterinary dentistry. The flexibility and mobility of the fingers, paws, neck, and back of the dog are fundamentally lower than that of the corresponding human organs. The dog cannot fix the detector of the X-ray image with a finger or sit motionlessly in the chair of the cone-ray tomograph for a long time. The dog also cannot understand and fulfill the specific requirements of the X-ray assistant during the X-ray shooting.

Obviously, to solve the problems of diagnosis of veterinary dentistry in full, it is necessary to develop the appropriate technology.

Materials and Methods

At the present time for diagnostics in veterinary stomatology is used:

- sighting (traditional) dental units for taking pictures of individual teeth or jaw areas on an X-ray detector measuring 30 × 40 mm, which is placed in the oral cavity of the animal (Fig. 1)

Figure 1. Examples of obtained images using standard sighting dental devices.

- stationary X-ray apparatus for obtaining images of the entire head of the animal on an X-ray detector of 240 × 300 mm or more (Fig. 2, 3).

Figure 2. Scheme of shooting using powerful stationary X-ray apparatus.

Figure 3. Example of obtained images using powerful stationary X-ray apparatus.

The main disadvantages in the first case.

The size of the image detector does not allow:

- get a complete picture of even one tooth of a large dog;
- placement the image detector in the oral cavity of a small dog.

The probability of damage to the image detector by a dog of any size is great.

The main disadvantages in the second case:

- on the picture of the dog's head, images of all the teeth, bones of the skull and soft tissues are superimposed on

each other. This greatly complicates the description of the picture and the diagnosis

- the additional dosage for the animal and personnel.

At the beginning of the 21st century in Russia was offered a technique of Microfocus X-ray radiography. Unlike the currently known methods, this method allows to obtain:

- sighting images of individual teeth or jaw areas;
- panoramic images of the full dentition of both jaws, including adjacent anatomical structures [2].

To implement the technique, an X-ray tube with a hollow outside anode and a massive target 0.01BD57-90 (Fig. 4) was developed [3]. The length of the anode pipe is 120 mm, diameter 12 mm, and material - aluminum. The tube generates a panoramic X-ray beam with a solution angle of 135 × 360 °. The direction of the radiation output is opposite to the direction of motion of the electrons in the accelerating gap of the cathode-anode (tube target). On its basis, the sighting-panoramic dental X-ray apparatus PARDUS-02 was also developed [4].

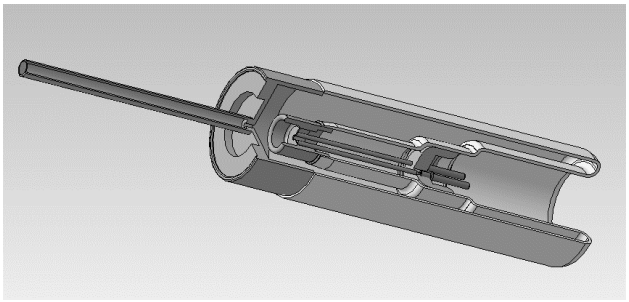

Figure 4. 3D drawing of the X-ray tube with a hollow outside anode and a massive target 0.01BD57-90.

Results

Studies conducted based on the city veterinary clinic №1 of St. Petersburg showed that the sighting device of the PARDUS family in portable design can be successfully used in veterinary dentistry for the direct dental studies. In the course of the tests, specialists highly appreciated the quality of the obtained X-ray images (Fig. 5), as well as the prospects for the development of a sight-panoramic technique for performing X-ray studies in veterinary medicine.

Figure 5. Dental pictures, obtained with portable X-ray device of the family "PARDUS".

A fundamental difference between the technique of panoramic X-ray radiography in veterinary medicine, in contrast to the standard methods, is the location of the anode of the X-ray tube directly inside the oral cavity of the animal. The X-ray generated by the tube passes through the teeth, jawbones, soft tissues and get to the X-ray detector, which is located outside the head of the dog opposite the diagnosed area (Fig. 6). In the course of further planned studies, the methods of installation will be tested, the shooting regimes will be improved, the dose of irradiation of the animal and the X-ray assistant will be estimated.

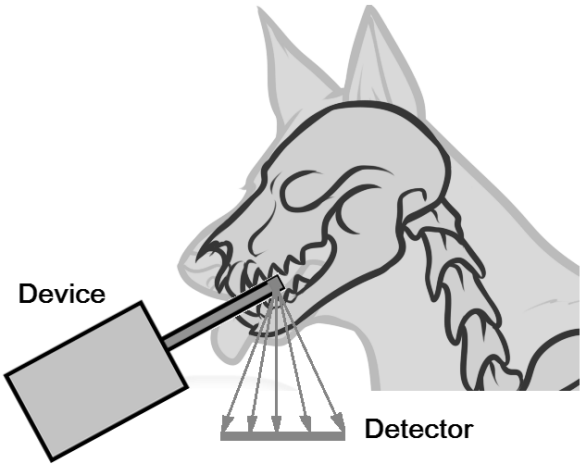

Figure 6. Scheme of the intraoral panoramic X-ray survey in veterinary medicine.

The main advantages of the method of the intraoral survey in veterinary medicine:

- small diameter and long length of the anode pipe allow placing the target of the X-ray tube anywhere in the oral cavity of an animal of any size;
- the reverse panoramic direction of X-ray radiation excludes the imposition of teeth belonging to different branches of the jaws;
- high informativeness of the images is provided by a small focal spot at an extremely low current tube (0.1 mA) and, accordingly, very low the exposure dose;
- the source of X-ray radiation is located inside the mouth, so the intensity of unused radiation is fundamentally lower due to absorption of the tissues of the head;
- ensured safe conditions for the X-ray assistant when shooting "from the hand" without the use of a traditional tripod;
- shooting "from the hand" greatly facilitates the laying of the animal and improves the efficiency of the diagnosis, primarily in non-specialized and non-stationary conditions.

Conclusions

As a result of a complex of design, technological and clinical research, a new technology for performing X-ray diagnostics in veterinary dentistry was proposed. The technology includes the method of the sight-panoramic survey

of the maxillofacial department of the animal and a set of digital technical means for its implementation. Conducted tests have shown expediency of carrying out of the further practical development in the field an X-ray survey of the maxillofacial department of the animals.

References

[1] Fundamentals of X-ray diagnostics / Ed. N.N. Blinov. Tutorial. - Moscow: Medicine, 2002.
[2] Potrakhov N.N. Microfocus X-ray radiography in dentistry and maxillofacial surgery. St. Petersburg: Technomedia Ltd., Page 184, 2007.
[3] Author's Certificate No. 1793491 of the USSR, MKI H01J35 / 08. X-ray tube / Potrakhov N.N. and others; Application 25.06.91; registered 08.10.92.
[4] Potrakhov N.N., Potrakhov E.N., Gryaznov A.Y. Portable X-ray diagnostic devices of the family "PARDUS" for sighting and panoramic research in stomatology and maxillofacial surgery // Medical technology, pages.45-46 - 2008. - №5.

Specialized x-ray machine for neonatology

V.V. Klonov[1], I.A. Larionov[1], N.N. Potrahov[1]

[1] Electrotechnical University "LETI", Professor Popov street h. 5, Saint-Petersburg, Russian Federation

Contact: klonovvladimir@yandex.ru

Introduction

The usage of X-ray radiation in modern neonatology makes a significant contribution to the quality of medical care for newborns with pathologies. High-quality image of the baby allows to quickly diagnose the problem or to prevent future possible complications.

The method of contact diagnostics (see fig.1) gives satisfactory results, however, to obtain informative images should take into account the following restrictions:

1. *A large distance between the radiation source and the object of study*. This condition is dictated by the need to distance the radiation source to reduce the blurring of the edges. It is necessary to use sufficiently powerful sources to work around the dynamic range of the receiver (which leads to the maximum contrast of the image). Increased tube current causes an increase of the focal spot. Its size directly affects the degree of outer edges blur on the image, which is unacceptable in the case of medical diagnosis. Compensation for this phenomenon is increasing the distance between source and receiver. This can lead to unwanted additional exposure of medical staff and others patients.

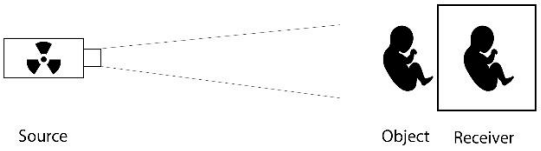

Figure 1: Contact X-ray diagnostics of newborns

2. *High resolution X-ray detector*. Upon contact of an object and a radiation receiver, the image quality depends on resolution of the receiver. However, increasing resolution naturally reduces sensitivity of pixels (by reducing their geometry sizes). This eventually leads to the necessity of increasing power of the radiation source.

3. *High power X-ray radiation*. Increased distance source-object and high resolution of the receiver lead to significant increase in power of X-ray diagnostic machine. Traditionally, the radiological diagnosis in neonatology and pediatrics using radiation sources with power up to 5 kW, which is directly related to their size and weight. From the point of view of stationary use it's not a big deal. However, for portable options, which work in conditions of constant transportation, this factor is essential.

Thus, of use of X-ray machines in non-specialized conditions, for example when you need to do diagnostic immediately after the procedure of childbirth is in the room of the maternity ward, the use of classical X-ray machines, described above, is not optimal. The basic idea, which is based on an alternative approach to the diagnosis of newborns is the use of smaller power sources with reduced size of the focal spot of the radiation source. The decrease in its value up to 0.3 mm or below will allow to diagnose newborns under appropriate conditions with scaling method (see fig. 2). Decrease focal spot is achieved with a small current of the tube and using additional focusing electrodes. The lack of dose is compensated by minor (20 – 30%) increasing of operating voltage and decreasing of shooting distance. As a result, while maintaining the quality of the image this approach provides the following benefits:

- Resolution of the receiver can be reduced. This leads to the best sensitivity.
- Source-object distance is reduced, which minimizes exposure of staff and others, and also reduces requirements on the output power.
- Relatively low power (360 – 500 W) of radiation source reduces weight and size of the device, which greatly simplifies its use in unsteady conditions [1].

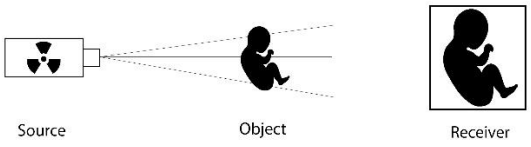

Figure 2: X-ray diagnostics of newborns with scaling

In this paper, the circuit and structural features of low-power portable apparatus for neonatology, its internal structure and organization of electronic modules are introduced.

Materials and Methods

Interconnection of electronic modules built on the centralized control principle (see fig.3). For the implementation of sensing functions and heat supplying, the subsidiary module is used. The high-voltage part comprises a generator and a voltage multiplier.

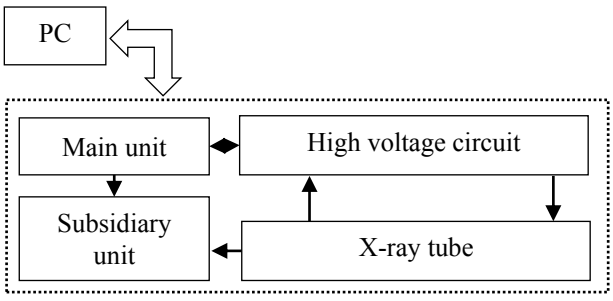

Figure 3: The generalized structure of electronic modules

Fig. 4 represents the organization of the main control module. Its basic functions are:

- control of X-ray tube supply power generator;
- management of data flow between PC and device;
- monitoring of the central module: the temperature of the inductive element, the average temperature of the power transistors, the average power consumption;
- X-ray dose control.

The Central MCU communicates with the Ethernet controller that have hardware support for the TCP/IP protocol. All data transmission is handling through specialized Ethernet PHY controller by SPI interface. The use of specialized chip simplifies the interaction of the microcontroller with a PC and partially offloads the core and the peripheral modules, however, the cost of such solution is considerably higher than MII/RMII chip. The power supply is controlled by 16-bit timer with push-pull signal with a pulse width modulation (PWM) [2]. The module is located on the outside of the case and is not in contact with an insulating filler (transformer oil). Inside casing the subsidiary module, all high voltage components (transformer, multiplier and divider, the X-ray tube) are located. From the Central unit to the internal elements a power line (the transmission of energy to the transformer) and two differential signal lines are routed. To ensure independent transmission in both directions of the communication channel a full duplex is implemented.

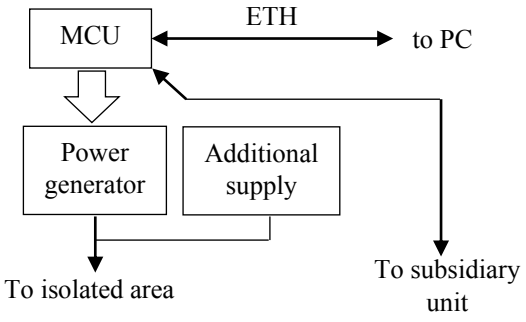

Figure 4: Structural diagram of control board

A subsidiary module (a structural diagram is represented in fig. 5) is placed inside the case in the vicinity of high-voltage circuits. The unit performs following functions:

- control of filament current;
- measurement of electrical parameters of the X-ray tube, such as voltage, tube current, filament current;
- calibration of measurement data and control of electrical parameters of the X-ray tube searching in a given workspace;
- control of ambient temperature (temperature of transformer oil);
- flexible converting input analog signals.

The main module node is the MCU, which controls the filament current and measures circuit parameters using the 4-channel 12-bit internal ADC. The temperature of the environment is controlled by sensor, which integrated into MCU package. Communication with the control board is realized via the RS-485 interface. This solution provides the most optimal ratio of communication speed to noise immunity.

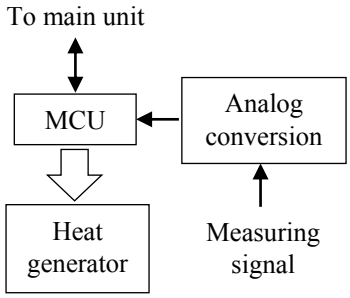

Figure 5: Structural diagram of the subsidiary module

When controlling the filament current is important to consider that the resistance of the filament is substantially depends of temperature. Standard approach uses the pulse-width modulation; full voltage amplitude is applied to the filament. In the case of low temperature (it happens at first turn on) initial current intensity may be significant (exceed the maximum to 1.5 times). This eventually may lead to its thermal destruction. A solution to this problem is the combination of pulse-width modulation and frequency control [3]. Fig. 6 represents a simplified circuit of the filament supply. The pins of the X-ray tube cathode form a parasitic inductance which at high frequency limits start current equal to:

$$I_{start} = \frac{U_s}{R_{heat} + Z_{leak}}, \qquad (1)$$

where U_s is the amplitude of the voltage of the filament supply, V; R_{heat} – the resistance of the filament in Ohms; Z_{leak} – impedance of the parasitic inductance of pins on the current frequency, Ohms.

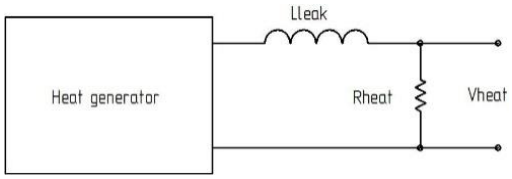

Figure 6: The equivalent circuit of circuit the heated filament

Thus, the combination of a gradual increase of duty cycle and frequency can be used to achieve amplitude modulation of the heat voltage that will provide a smooth increase of operating current and significantly extend the service life of the machine.

The machine construction design (see fig. 7) is based on several ribs formation of the carrier frame. This is done by perpendicularly arranged walls that provide a rigid positioning of the device in space relative to the outer aluminum case. This aspect is especially important because of the strict requirements for maintaining a minimum displacement of the apparatus. The change in the position in the process of exploitation can lead to the risk of voltage breakdown. Therefore, special attention was paid to make the structure as rigid as possible [4].

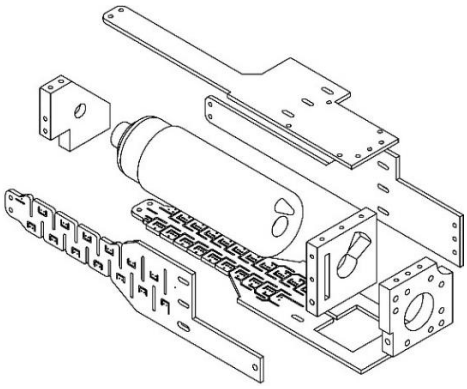

Figure 7: Sketch of the internal nodes construction of X-ray machine

Load-bearing walls are made of FR4. The products made of this material is technologically advanced and has a stable surface breakdown voltage of about 1.5 kV/mm (assuming storage material is isolated from dirt and moisture). The transverse plate is made of PTFE and in addition to quality insulation provide rigid fixation of all structural elements.

Results

Eventually, fully functioning layout portable, low power apparatus for neonatology with the ability to control from PC or control panel, were designed and constructed. Main characteristics are introduced below:

- operating voltage: 120 kV;
- operating voltage ripple: < 3%;
- maximum power: 360 W;
- efficiency: > 75%;
- output raise time: < 20 ms;
- weight: 5 kg;
- controlled by PC or portable console;
- size: 380 × 130 × 180 mm.

The present design provides a quick assembly, which increases the manufacturability of serial production. A modular approach to the design of electric circuits allows to make fast replacement of units and perform a local update of specific parts of the scheme. Testing the model sample of the device was carried out in laboratory conditions.

The closest analog is portable X-ray machine EcoRay 9020HF. Comparison (see tab. 1) demonstrates, that new design uses tube with lower focal spot, which allows to decrease power of machine and its weight. Lower power is compensated by higher voltage (120 kV against 90 kV) and decreased distance (0.35 m).

Table 1: Characteristics of apparatus in comparison with nearest analog on the market

Item	Introduced machine	Analog
Focal spot size, mm	0.4 × 0.4	1.2 × 1.2
Power, W	360	1200
Operating voltage, kV	120	90
Shooting distance, m	0.35	0.66
Weight, kg	5	7

Discussion and Conclusions

Modern medical X-ray machines allow to obtain high-quality images for accurate diagnosis of patients. However, medical staff are always at risk of extra exposure. This is especially true for portable applications, when medical worker holds the apparatus or stands near it. Introduced machine greatly reduces extra radiation in comparison with similar ones having large focal spot. Small focal spot allows to decrease power of the apparatus and distance between source and receiver. Dimensions and weight are also decreased, portability is improved. Moreover, X-ray diagnostic complex based on microfocus tube can perform images with higher quality than classic apparatus does. Implementing local net between machine, PC and receiver allows to expand possibilities of constructing specialized X-ray complexes. Several sources and receivers could be combined under single or distributed control.

References

[1] Potrakhov N N. Journal of new medical technologies, 2007, vol. 14, no. 3 167-9.

[2] V. V. Klonov., I. A. Larionov, V. B. Bessonov. Modification of circuit and investigation of operating modes of the high-frequency pulse resonance converter for the X-ray tube power supply. In IV all-russian scientific and practical conference for manufacturers of X-ray technology, pages 42–46, nov 2017.

[3] Philips semiconductors. Power semiconductor applications, chapter 2 – Switch mode power supplies. URL: http://educypedia.karadimov.info/library/APPCHP2.pdf.

[4] G. Pisarenko 1988. Handbook on strength of materials.

Acknowledgements

The work was supported by Federal target program «Research and development in the priority areas of development of the scientific and technological complex of Russia for 2014-2020», project № 14.578.21.0262 «Digital neonatal fine-focus X-ray diagnostic complex».

Computer program for setting up a medical X-ray apparatus

I.A. Larionov, V.V. Klonov, V.B. Bessonov.

Saint Petersburg Electrotechnical University "LETI", Professor Popov street h. 5, Saint-Petersburg, Russian Federation

Contact: silverusion@yandex.ru

Introduction

Distribution of digital equipment, including the production of medical X-ray apparatuses, allows to control various devices using a computer software. At present, this mechanism is a widespread practice.

The vast majority of power sources of medical X-ray apparatuses are built according to the scheme with amplitude or pulse-width modulation (PWM). At the same time, the resonance control scheme of the X-ray tube is also promising. In comparison with PWM control, the resonance circuit allows to obtain greater efficiency and to provide a more exact adjustment of operating parameters of the apparatus. The adjustable parameters are: resonance frequency, heating current and duty cycle. The most convenient way to establish the values of these quantities is their software setting. Thus, the aim of the work is to create graphic user interface (GUI) for setting up an X-ray apparatus.

Materials and Methods

A model sample of medical X-ray machine for neonatology was compiled on the basis of the EPU department of ETU «LETI» [1]. Due to the features of a scope of the apparatus it is necessary to provide high efficiency of his work that is achieved by applying a resonant control circuit.

Parameters of the X-ray apparatus

The parameters of the power supply (excluding the voltage multiplier), which define the mode of operation of the X-ray tube (current and voltage on the tube) include filament current, resonant frequency and duty cycle. A specific set of values for these parameters will yield the desired current and voltage of the tube.

In order to determine possible combinations of these parameters for establishment the required values of current and voltage on the X-ray tube, the characteristic curves for current and voltage were obtained experimentally. The received dependences are qualitatively reflected in figure 1, 2 and 3 (in Fig. 1, the ratio of currents is as follows $I_4 < I_3 < I_2 < I_1$; in Fig. 3, the ratio of the filament currents is as follows $I_{h4} > I_{h3} > I_{h2} > I_{h1}$).

Experiments have shown that at different currents of heat, the current of the X-ray tube is guaranteed to reach saturation at a voltage of 40 kV (V_{min}). This feature allows to receive calibration points as follows: to expose the minimum level of filling (about 5%); to shift the frequency before obtaining voltage on the tube of 40 kV; when this value is reached, record the calibration point parameters. Increasing the filling coefficient with a given step, it is possible to receive a set of calibration points. In order to set certain operating parameters, the machine takes the values of the obtained calibration points as a basis during operation and, if necessary, calculates the value at the interval between them.

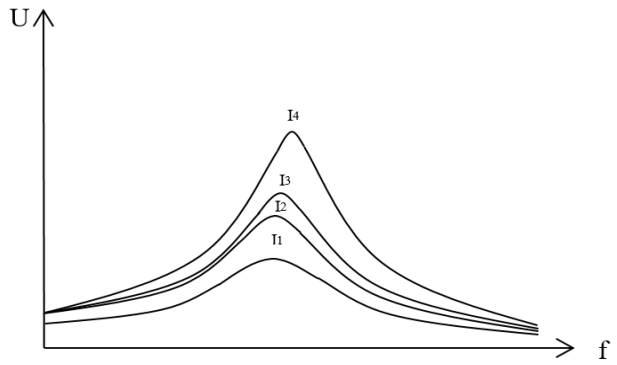

Figure 1: Dependence of the X-ray tube voltage on the generator frequency

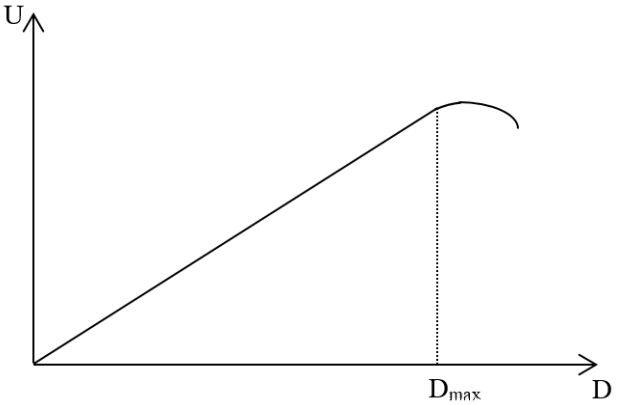

Figure 2: Dependence of the X-ray tube voltage on duty cycle

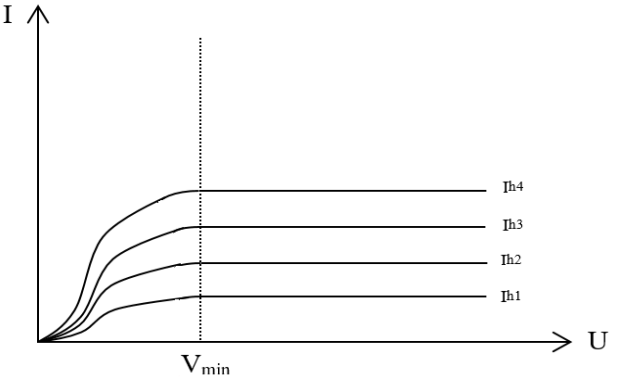

Figure 3: Volt-ampere characteristic of the X-ray tube

Features of the apparatus control and their software implementation

Due to the fact that the X-ray radiation belongs to ionizing, special attention should be given to matters of radiation safety when carrying out all types of work. If it is necessary to control the X-ray machine remotely using a computer program, first of all there is a question about the reliability of the communication line. In addition, the reliability of the received and sent data, which can affect the operation of the machine, is also an important point. At the same time all data can be sent and received only according to a certain protocol of interaction.

Reliability of the communication line: Taking into account the aforesaid, communication of the apparatus with a personal computer can be performed through the Ethernet line. There may be situations when the apparatus stops responding to commands due to the loss of physical connection between the cables. In that case, if the generation of X-ray has been started, then it will continue that is undesirable. To monitor the situation of loss of communication software implemented the constant data exchange between the personal computer and the x-ray apparatus. The need for constant monitoring of the operational parameters of the apparatus justifies the existence of such a constant connection. If necessary to send a command that differs from request parameters, corresponding to the command packet simply replaces the send queue of the request packet.

Accuracy of the data: The TCP / IP Protocol stack was selected as the top-level protocols. This ensures that the data packet is delivered to the recipient. For a possibility of management under the TCP/IP protocol a specialized chip of w5100 is used. In this chip, the use of standardized protocols is implemented by hardware, which eliminates the need to control the delivery and check the checksum (this factor is important in the X-ray t equipment as ensuring the reliability of the transmitted data will protect the machine from possible errors and emergency uncontrolled user modes).

Protocol of interaction: Any interaction between the control device and the operated device is performed according to certain rules, usually described in the so-called protocols. The first version of the protocol of interaction *XRTMP* (X-ray tube management protocol) between the x-ray apparatus and the external controller was developed to simplify the interaction of developers when writing software for the PC and for the microcontroller. In accordance with the protocol, all packets have a fixed length, which is 20 bytes. Figure 4 shows a block diagram of the interaction levels between the control device and the X-ray apparatus. The drafted protocol is responsible for the interpretation of transmitted data packets and the organization of interaction between internal nodes of the apparatus. In accordance with the communication protocol, besides control commands (these include turning the machine on and off with the set parameters), there are also special commands for apparatus settings (for example, setting generator parameters such as frequency and duty cycle, etc.).

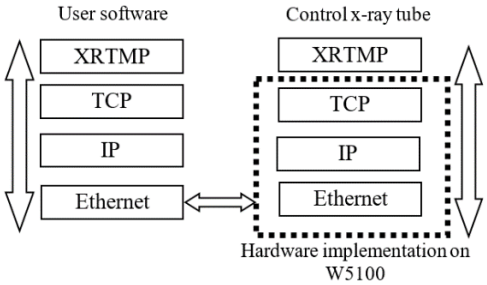

Figure 4: Organization of a protocol stack

Setup of the apparatus: Values of the operational parameters, though weakly, but vary from device to device in connection with dissimilarity of the electronic components used to build these devices. For this reason, at the first inclusion tuning of the apparatus has to be performed surely. Otherwise, the parameters stated in the documentation may not fully correspond to reality. Program and circuit control implementation provides a possibility of various calibrations types and settings:

- calibration of sensor;
- adjustment of emergency thresholds;
- setting operation modes of the tube;
- control of the working dose.

Calibration of sensors is intended for increase the accuracy and reliability of the data about current and voltage on X-ray tube, about heat current and also a radiation dose received from them. Depending on which components were used to assemble the apparatus, the emergency threshold values may vary. In order to take into account this feature, it is possible to update the threshold values. Setting of the operation modes allows to correct the current and voltage values for modes which are already written down in the machine. Special attention among the possible calibrations and settings deserves to control the working dose.
Structurally inside the apparatus there is a possibility of placement a special sensor, which is capable to register a relative dose of X-ray radiation. Under normal operating conditions, the dose level will coincide with the calibrated values (with allowance for minor fluctuations). In the case when the mode of operation of the apparatus is incorrect, the program will be able to track this by changing the working dose of radiation. All settings occur at the level of the microcontroller, which receives instructions for calibration from the host computer.

Results

To control the model of the X-ray apparatus, a program for a personal computer has been developed. As a development tool the framework Qt [2] was applied, and the program was under construction on the basis mentioned above data exchange protocol. With the help of this development environment, the interface of the control program was designed and implemented, the main window of

which is represented in the Fig. 5. The program is written on the C++ language.

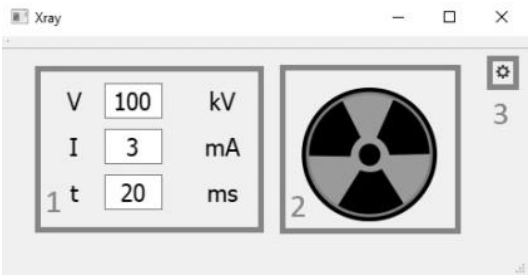

Figure 5: Main window of the program

The main window of the program can be conditionally divided into 3 parts: first block is the unit for setting exposure parameters (voltage, current and time); second block is the immediate start-up of apparatus (inclusion of X-ray radiation); third block is the configuration icon. Almost always the operator needs to use only the first two blocks. However, there are situations when it is necessary to change the machine settings (for example, to rebuild the resonant frequency). Circuitry and software implementation allow performing this action by simply changing the value in the corresponding field of the program by the operator. Despite such apparent simplicity of adjustment, all controls for calibration, advanced setting and connection of the machine are taken out into separate window, which is accessed after entering the correct password. Part of the advanced program settings window is shown in Fig. 6.

Figure 6: Part of advanced settings window

The presented part of the advanced settings allows changing the resonance frequency, duty cycle, starting and stopping the generator, and also checking the communication by the signal LED.

In general, advanced settings allow the attendants to perform the following actions:

- change IP-addresses and ports as needed to establish the connection between the personal computer and the apparatus;
- open and close the corresponding TCP connection;
- send a special request to the apparatus;
- receive and visualize response from the apparatus to corresponding request;
- start and stop pulse generator;
- change frequency and duty ratio of the generator;
- monitor the connection and operation of apparatus by means from signal LED;
- perform calibration for following parameters: voltage, tube current, filament current and temperature of tube;
- to monitor the above parameters in real time.

Indication of the current values of the main parameters of the apparatus is also contained in a separate part of the extended settings window of the apparatus. The parameter display field is shown in Fig. 7.

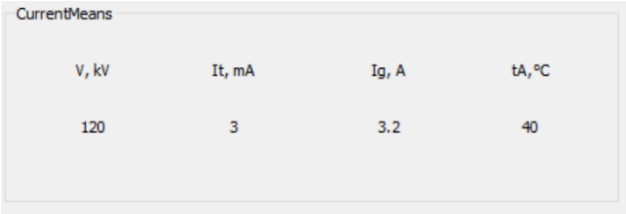

Figure 7: Indication of the current parameters of the apparatus

It should be noted that the program requires a computer with an installed operating system of the Windows family (Windows XP SP3 or higher), as well as the ability to use the computer TCP/IP connection. As for the rest, the program does not impose special requirements on the used computer.

Conclusions

The computer program created in the course of operation allows to adjust the X-ray apparatus for neonatology to improve its performance characteristics. In the future we plan to expand the ability program to control several satellites simultaneously, and also to find the optimal calibration algorithm for the apparatus and to implement it programmatically.

References

[1] V. V Klonov., I. A. Larionov, V. B. Bessonov. Modification of circuit and investigation of operating modes of the high-frequency pulse resonance converter for the X-ray tube power supply. In IV all-russian scientific and practical conference for manufacturers of X-ray technology, pages 42 – 46, nov 2017.

[2] M. Summerfield. Advanced Qt programming: creating great software with C++ and Qt 4. Courier in Westford, Massachusetts, 2010.

Acknowledgements

The work was supported by Federal target program «Research and development in the priority areas of development of the scientific and technological complex of Russia for 2014-2020», project № 14.578.21.0262 «Digital neonatal fine-focus X-ray diagnostic complex».

Digital X-ray image processing with using the adaptive histogram equalization and adaptive background correction

Staroverov N.E., Gryaznov A. Y., Kholopova E. D.

[1]СПбГЭТУ «ЛЭТИ», Professor Popov st. h. 5, Saint-Petersburg, Russian Federation

Contact: nik0205st@mail.ru

Introduction

Microfocus X-ray is a combination of methods for receiving X-ray images using radiation sources with focal spots size less than 100 μm. Using these sources gives the opportunity to obtain images with a direct geometric image magnification 5-20 times. Today microfocus X-ray is widely used in medicine, industrial non-destructive testing and quality assessment of agricultural crops. [1,2,3].

In the list of cases, microfocus X-ray images could not be authentically analyzed because of insufficient quality of images. More often main disadvantages of microfocus X-ray images are irregular background, distorted brightness characteristics, the presence of noises. Therefore, the development of algorithms for digital processing of microfocus X-ray images is a relevant task.

Materials and Methods

In the paper, two algorithms of digital X-ray images processing are considered: the algorithm for correcting the uneven image background based on the subtraction of the distorting function and the algorithm for locally-adaptive histogram equalization.

Algorithm for correcting the image background

During the X-ray examination according to the scheme with the direct geometric magnification uneven image background arises, complicating visual analysis and subsequent digital image processing. A distorting function is introduced to eliminate irregular background of the image. It is considered that the receiver registers an image that can be represented as the sum of the image and the distorting function, which creates the uneven background. The distorting function in microfocus X-ray is usually described by a function of the form:

$$g(x,y) = C[(x - \frac{x_{max}}{2})^2 + \left(y - \frac{y_{max}}{2}\right)^2], \quad (1)$$

where C – is a constant, whose value depends on the microfocus X-ray apparatus mode and the shooting conditions, x_{max} and y_{max} – is the vertical and horizontal size of the image respectively.

This form of distorting function follows from shooting peculiarities with image enlarging, as X-ray radiation intensity decreases proportionally to the square of the distance.

Figure 1: Image for the analysis

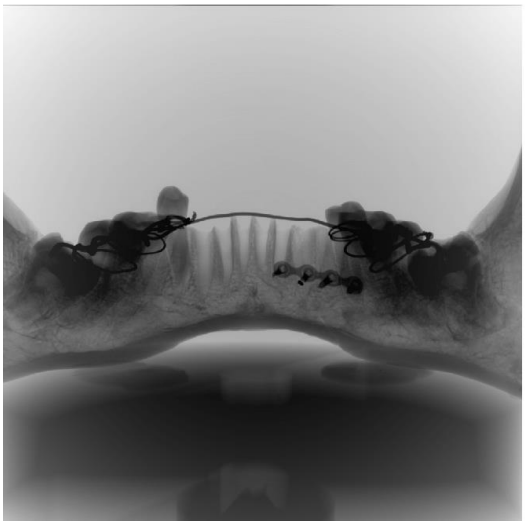

Figure 2: The result of image background correction

For every single profile, its minimum and maximum are determined and the difference between them is found. The constant C is determined by the expression (2) as the medium difference between minimum and maximum of the profiles.

$$C = \frac{\sum_k^N (a_{k\,max} - a_{k\,min})}{N}, \quad (2)$$

where N – the number of profiles, $a_{k\,max}$ and $a_{k\,min}$ – respectively maximum and minimum brightness values. In case of the big difference between profiles minimums and maximums the number of the analysed profiles should be increased to get the correct constant.

On figure 3 profile built along the upper edge of the image is presented.

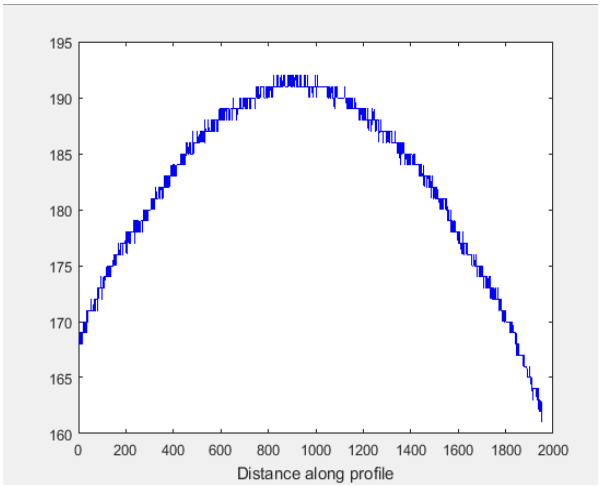

Figure3: Profile of the upper edge of the image

The resulting image *f(x,y)* is obtained by the way of subtraction *g(x,y)* from image registered by the receiver:

$$f(x,y) = h(x,y) - g(x,y) \qquad (3)$$

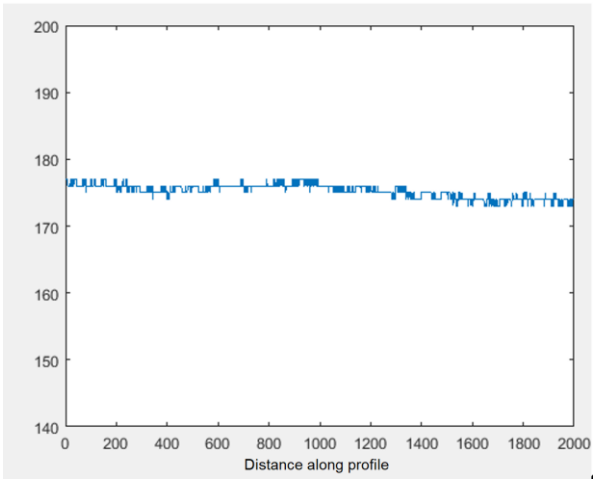

Figure4: Profile of the upper edge of the image after correction

On the figure 4 profile built along the upper edge of the image after the correction of the tone is presented. As it's shown in the figure 3 profile of the image is aligned, uneven background illumination is removed. After image background correction, it's much more convenient for automatic analysis. Visual analysis also becomes easier. So, for teeth image selection on the image primitive threshold transformation can be used, while in a case of uneven background it is ineffective.

The algorithm of local-adaptive equalization of the histogram

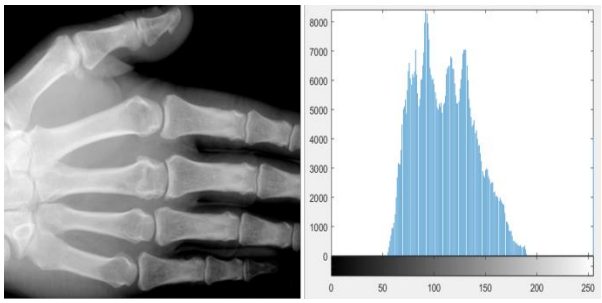

Figure5: The original image and its histogram

The method of the local-adaptive histogram equalization can be also used for the image's contrast improving.

Histogram of the image is a function defined as:

$$h(r_k) = n_k, \qquad (4)$$

where r_k – *k*- is a level of brightness on the image, n_k– number of pixels, belonging to this level of brightness. If the image has a low contrast, this means that the histogram values are concentrated in a certain region of the brightness range [5]. For improving contrast it's necessary for non-zero levels of the histogram to overlap the bigger part of the range of brightness. Equalization of the histogram is a transformation that can be described by the formula:

$$s_k = T(r_k) = \sum_{j=0}^{k} \frac{n_j}{n}, \qquad (5)$$

where s_k – k-level of the brightness of the processed image, n – the common number of pixels on the image, n_j– number of pixels that have brightness r_k.

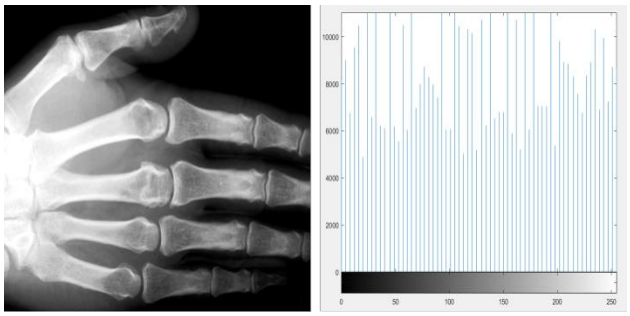

Figure6: The image and its histogram after using the method of histograms' equalization

This method allows you to significantly increase the contrast of X-ray microfocus images without the operator's participation. However, the method of the histogram equalizing does not lead to the desired result if the image has an uneven background or if the image has a wide histogram.

To overcome listed limitations method of local-adaptive histogram's equalization is applied: at first in the method of local-adaptive histogram's equalization the image is splitted into a number of non-crossing areas (usually from

16 to 128) and then every single area is subjected to the histogram's equalization. On the next step, all the areas are combined into a single image with the bilinear interpolation. For removing artificial borders, which appear in the combining areas, the interpolation is used. In this way, there is a local increase in the contrast of the main image details.

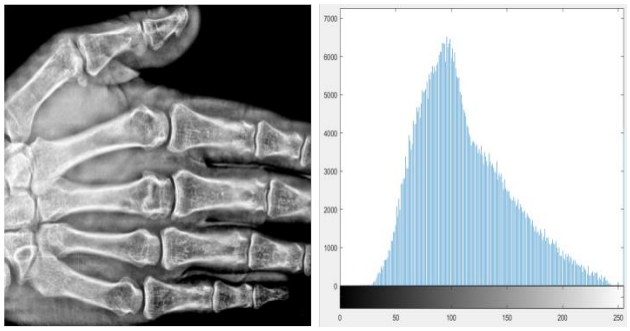

Figure7: Image and its histogram after using the method of the local-adaptive equalization of the histogram

Results and discussion

To check the quality of method of the background correction a sample of 100 medical microfocus X-ray images obtained using different radiation receivers was used.

As the result of the developed method backgrounds of the 73% of the images were fully leveled (pixel brightness values difference between the edges and the center has become less than 5 points), for 27% of the images pixel brightness values difference between the edges and the center has become less than 10 points.

Every single wrong case of the background correction was considered in details. In all the cases error was caused by the fact that objects in the image occupied more than 80% of the length of the profile, so there wasn't enough information to determine the background.

To check the quality of method of the background correction a sample of 50 medical microfocus X-ray images was used. As the result of the application of the method of histogram's adaptive equalization to all images from the sample for 80% of the images, a notable contrast increase was fixed. It also became possible to distinguish the details of tissues and bones. If the traditional method of histogram equalization is applied to the same images, significant improvement in contrast, without deterioration of contrast in other areas of the image, was achieved only in 40% of cases.

Conclusions

As the result the algorithm for image background correction and algorithm of the local-adaptive histogram equalization was developed.

On the samples of microfocus X-ray images, investigations of developed methods were done. Both of the methods gave satisfactory results.

Also, it was determined that while doing the local-adaptive equalization of the histogram, contrast image of both soft and osseous tissues can be reached on the same shot.

References

[1] Potrakhov N N. Journal of new medical technologies, 2007, vol. 14, no. 3 167-9.

[2] Potrakhov N N, Gryaznov A Yu Zhamova K K , Bessonov V B, Obodovski A V, Staroverov N E, Kholopova E D, 5 46-54 Biotechnosphere

[3] Gryaznov A Yu Methods and systems microfocus phase contrast X-ray medical. Doct. Diss., Saint Petersburg, 2010. 245 p.

[4] Sobel and G. Feldman, "A 3x3 Isotropic Gradient Operator for Image Processing," Pattern Classification and Scene Analysis, 1973, p. 271-272.

[5] Gonzalez R C, Woods R E. Digital Image Processing. Prentice Hall Publ., 2008, 976 p.

Acknowledgements

The work was supported by Federal target program «Research and development in the priority areas of development of the scientific and technological complex of Russia for 2014-2020», project № 14.578.21.0262 « Digital neonatal fine-focus X-ray diagnostic complex ».

The advantages of background correction of microfocus X-ray images are presented.